eXPRESS Polymer Letters Vol.7, No.11 (2013) 885
Available online at www.expresspolymlett.com
DOI: 10.3144/expresspolymlett.2013.85

Editorial corner – a personal view
Controlling properties by understanding polymer crystallization

M. Gahleitner[*]

Borealis Polyolefine GmbH, Innovation Headquarters, St. Peterstr. 25, 4021 Linz, Austria

More than half of the thermoplastic polymers used worldwide have a crystalline structure, making solidification a complex process in which polymer microstructure, additives and processing conditions together define the final optical and mechanical properties. While standard differential scanning calorimetry (DSC) or heat-stage microscopy with a limited heating and cooling rate range have dominated polymer studies for many years, conversion processes became faster and faster. Now methods have caught up, using nano-calorimetry for better heat transfer and enabling up to 10^6 K·s^{-1} in cooling and heating. This allows to study quenching effects and the development of metastable crystal modifications, as in case of isotactic polypropylene (iPP) or poly(ethylene terephthalate) (PET). Next steps are increasing the possible pressure and deformation rate ranges into 'realistic' regions – also here, instrumental challenges exist.

A better understanding of crystallization processes enabled by better data allows better conversion modelling. For injection moulding it is already widely applied for optimizing geometry and parameters, even if often with unrealistic assumptions. The situation is, however, worse for processes involving free surfaces like blown film or extrusion blow moulding, where empirical rules still dominate industrial practice. And, of course, the next step should be to relate crystalline morphology to mechanics with realistic structural models.

For years, iPP has been in the focus of polymer crystallization. For some reasons it is a good 'model material': Chain structure and molecular weight distribution can be varied widely, in practice for product design. iPP polymorphism has got more diverse recently, the three forms of α-, β- and γ-iPP being expanded by the trigonal δ-form. And the combination of moderately fast crystal growth at large undercoolings together with the absence of sporadic nucleation makes it an ideal material for crystallization control by nucleating agents.

Other areas still need 'elucidation'. For linear polyethylene (HDPE) with its trickily high crystallization rate, effects of high molecular weight fractions and flow are getting attention recently. Effects of confined crystallization in thin layers or small droplets, as well as from solid glassy- or mesophase, need to be studied. For polar polymers, there is an interaction between crystallization and hydrogen bonds – recently seen as a severe factor for iPP graft copolymers of. And urgent is the problem of crystallizing biopolymers like poly(lactic acid) (PLA), so far limiting the applicability range. It will clearly be necessary to improve the understanding of nucleation options and the effect of chain disturbances (in commercial PLA up to 3 mol% stereodefects) on growth rate.

Dr. Markus Gahleitner
Member of International Advisory Board

[*]Corresponding author, e-mail: markus.gahleitner@borealisgroup.com

eXPRESS Polymer Letters Vol.7, No.11 (2013) 886–894
Available online at www.expresspolymlett.com
DOI: 10.3144/expresspolymlett.2013.86

Optimizing the bulk copolymerization of D,L-lactide and glycolide by response surface methodology

*L. I. Cabezas, R. Mazarro, I. Gracia, A. de Lucas, J. F. Rodríguez**

Department of Chemical Engineering, Institute of Chemical and Environmental Technology University of Castilla-La Mancha, Av. Camilo José Cela 12, 13071 Ciudad Real, Spain

Received 9 May 2013; accepted in revised form 11 July 2013

Abstract. Poly(D,L-lactide-co-glycolide), PLGA, is a biodegradable polyester with high interest in medical industry, especially when zinc (II) 2-ethylhexanoate ($ZnOct_2$) is used as catalyst substitute in polymerization processes as a substitute of the toxic tin (II) 2-ethylhexanoate ($SnOct_2$) together an initiator such as methanol to improve the reaction rate. This article shows the optimization of the bulk copolymerization method by using a factorial design approach on three experimental parameters: temperature (*T*), molar ratio monomers/catalyst (*MC* ratio) and molar ratio initiator/catalyst (*IC* ratio). Their influence on mass conversion (*X*) and number-average molecular weight (M_n) was also discussed. Also it provides a useful tool to select in a fast way the proper experimental conditions for the obtaining of this polymer as a previous stage in the synthesis and impregnation of biodegradable scaffolds. This analysis revealed that the most relevant variable in the process is the temperature, being desirable to use the high value (160ºC) in order to obtain high values of conversion and molecular weight.

Keywords: *biodegradable polymers, poly(D,L-lactide-co-glycolide), bulk polymerization, optimization, response surface methodology*

1. Introduction

Polylactide (PLA), polyglycolide (PGA) and their copolymer (PLGA) have been widely used as biomedical materials in absorbable sutures, orthopaedic devices, tissue scaffolds or drug delivery [1–3].

These types of biopolymers can be synthesized by direct melt polymerization of the hydroxyacids lactic and glycolic acid, as well as by ring-opening of the cyclic dimers lactide and glycolide (Figure 1). Ring-opening polymerization (ROP) can take place by cationic, anionic, coordination-insertion or enzymatic mechanisms. The coordination-insertion method has drawn the most attention and has been widely employed due to advantages such as lower risk of side reactions, higher molecular weights obtained and easy control of the molecular weight [4, 5]. Tin alkoxides and carboxylates have been usually used as catalysts for this mechanism, but the deposition of toxic metallic residues, difficult to extract, into the resulted polyesters becomes a severe drawback. This fact explains the success of zinc octoate, $ZnOct_2$, as a substitute [5–7]. The mechanism consists in the conversion of $ZnOct_2$ into zinc alkoxide by reaction with an alcohol added as an initiator. The deliberate addition of a predetermined amount of alcohol to the polymerisation medium is an effective way to control the molecular weight by the monomer-to-alcohol molar ratio [8]. Initiation

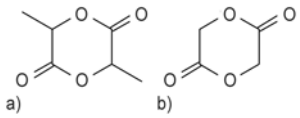

Figure 1. Chemical structure of cyclic dimers: (a) lactide; (b) glycolide.

*Corresponding author, e-mail: Juan.RRomero@uclm.es

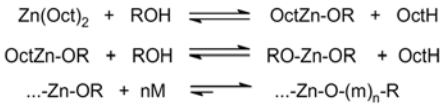

Figure 2. Initiation with zinc-alkoxide formed via carboxylate-alkoxide ligand exchange reactions. *R* denotes *H* or alkyl group, OctH is the 2-ethylhexanoic acid, *M* is the lactide or glycolide molecules and *m* is the polyester repeating unit [9]

Figure 3. Ring-opening polymerization of lactones: lactide and glycolide [8]

and ROP process is shown in Figure 2 and Figure 3 [8, 9].

In a previous study $ZnOct_2$ and methanol were determined as interesting catalyst and initiator respectively for the copolymerization of D,L-lactide and glycolide [10]. One of the aims of this work is to study the influence of different operational parameters such as temperature (*T*), molar ratio monomer to catalyst (*MC* ratio) and molar ratio initiator to catalyst (*IC* ratio) and their interactions in the copolymerization process and to carry out the optimization using Response Surface Methodology (RSM) to quantify the effect of main parameters and their interactions on polymer variables such as mass conversion (*X*) and number-average molecular weight (M_n) to produce suitable PLGA for subsequent use in drug release. Moreover, the mathematical model obtained provides a useful tool to select quickly and effortlessly the proper experimental conditions to achieve the desired properties of the polymer as a previous step in the synthesis and impregnation of biodegradable scaffolds [11, 12] without having to carry out complex mathematical calculations based on a rigorous theoretical model. Considering that this work represents only a practical approach in order to estimate the properties of the synthesized PLGA for a further step of impregnation, the rigorous study of the reactions that are taking place is not an end in itself (unlike other specific mechanistic or kinetic studies [10, 13–16]) so that this model of 'black box' is only a practical method to choose a set of conditions for the polymerization process.

2. Experimental

2.1. Materials

Glycolide (G) (1,4-dioxane-2,5-dione; Purac Biochem bv, The Netherlands) and D,L-lactide (L) (3,6-dimethyl-1,4-dioxane-2,5-dione; Purac Biochem bv, The Netherlands) both with a purity higher than 99.5%. Zinc octoate ($ZnOct_2$) (zinc (II) 2-ethylhexanoate; Nusa, Spain) with a metal content of 12%. Methanol anhydre (MeOH) (SDS s.a., Spain) with purity higher than 99.85%. Potassium bromide (KBr) (Sigma-Aldrich, Spain) with purity higher than 99%, for FTIR measures. Tetrahydrofuran (THF) (HPLC grade; SDS s.a., Spain). 1,1,1,3,3,3-hexafluor-2-propanol (Sigma-Aldrich, Spain) with purity higher than 99.8%. And n-hexane (analytical grade; Brenntag Químicas s.a., Spain). All products were used as received.

2.2. Bulk polymerizations

All experiments were carried out in a set-up consisting on a glass stirred-tank reactor with a volume of 500 mL and put into a constant inert atmosphere of nitrogen. The vessel was submerged into an oil bath and heated using a hot plate. Temperature was fixed by means of a temperature controller with a sensor inside the reaction melted mixture. Samples were collected along the reaction time through an opening in the reactor cover.

In a typical experiment, the procedure took place as described in [10] using a total monomer mass of 100 g, molar ratio D,L-lactide:glycolide (L:G) of 80:20 in order to get better control in the subsequent polymer degradation rate [17] and reaction time of 3 h. All the experiments were carried out in random order to avoid any kind of residual tendency and minimize the effect of possible uncontrolled variables.

2.3. Polymer characterizations

2.3.1. FTIR

A Fourier transform infrared spectrometer (FTIR 16 PC, Perkin Elmer, Spain) was used to measure the monomers ratio in polymer. All samples were dissolved in THF or 1,1,1,3,3,3-hexafluor-2-propanol (THF-insoluble samples) with a concentration of 35 $mg \cdot mL^{-1}$, and were applied on potassium bromide (KBr, standard infrared grade; Sigma-Aldrich

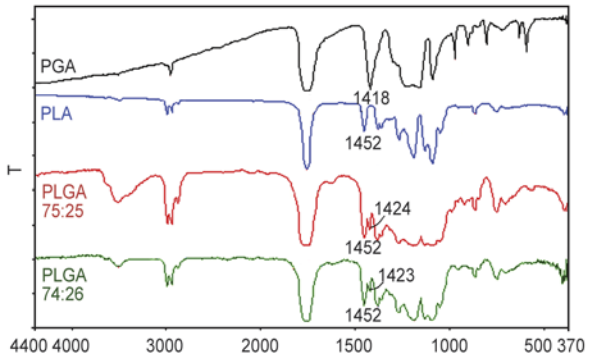

Figure 4. FTIR spectra for commercial homopolymers of glycolide, D,L-lactide, commercial PLGA 75:25 and synthesized PLGA 74:26

Química) pellets prepared by a manual hydraulic press (Perkin Elmer, Spain) and heated in oven at 70ºC oven 30 min to allow the solvent to evaporate, leaving a solid film. Poly(D,L-lactide) and copolymers of PLGA standards with different molar compositions of two comonomers (Sigma-Aldrich Química) were used as reference for the estimation of the comonomer ratio in the polymer taking into account the absorption bands of CH_2 group (1424 cm^{-1}) and CH (1452 cm^{-1}). Transmittance spectra were recorded from 370 to 4400 cm^{-1}. Figure 4 shows some examples of FTIR spectra with assigned peaks.

2.3.2. GPC

The molecular weight distribution was determined by gel permeation chromatography on a GPC chromatograph (Waters, Spain) equipped with two columns (Styragel HR2 and Styragel HR0.5) and a refractive index detector. Tetrahydrofuran (THF) was used as eluent at 35ºC (flow: 1 mL·min^{-1}; injection volume of 100 µL). Samples were dissolved in THF at a concentration of 1.5 mg·mL^{-1} and filtered before injection (pore size: 0.45 µm). Since no specific calibration was available, all measured molecular weights are values polystyrene-equivalent values and can be used only as relative quantities.

2.3.3. Gravimetric analysis

A simple gravimetric analysis consisting in dissolving all monomer-impurified polymer samples, previously quantified, in THF and precipitating only the polymer by the addition of n-hexane was carried out in order to calculate the mass conversion of each polymerization. The solid precipitate was filtrated under vacuum, drying in an oven at 70ºC for a minimum of 13 hours and until constant weight.

2.3.4. TGA

Thermogravimetric analysis was used in order to verify the mass conversion data obtained through gravimetric method. A TGA (TA Instruments, Q600) with a refrigerated cooling system was used. Sample weights were between 3–10 mg and the measures were run in aluminium pans until 210ºC (PLA) or 250ºC (PLGA) using a ramp of 40ºC·min^{-1}. The TGA cell was purged with nitrogen gas flow of 100 mL·min^{-1}. To estimate the polymer amount, TA Universal Analysis 2000 software was utilized.

2.4. Response surface methodology (RSM) and statistical analysis

RSM is commonly used in the study of empirical relationships between measured responses and independent variables (also called factors), minimizing experimentation and leading to correlations which can be used for optimization purposes [18].

The effect of the operating variables in the copolymerization process (temperature, *MC* ratio and *IC* ratio) and their possible interactions on the mass conversion (X) and number-average molecular weight (M_n) as response variables were carried out using a 23 full factorial design with two central points. The levels of each factor are indicated in Table 1 and were selected on the basis of preliminary studies of this polymerization system [10, 13–15]. In order to allow a direct comparison of each variable the independent variables were normalized in the range –1 to +1 according to Equation (1):

$$x_i = \frac{2(X_i - X_{min})}{(X_{max} - X_{min}) - 1} \quad (1)$$

where x_i is the normalized value of variable X at condition i, X_i the dimensional value, and X_{min} and X_{max} represent the dimensional inferior and superior limits, respectively.

A statistical analysis was performed for these results using the commercial software *Statgraphics*

Table 1. Levels of factors in the experimental design

Factor	Lower level (–1)	Higher level (+1)
Temperature [ºC]	120	160
Molar ratio monomer/catalyst	100	500
Molar ratio initiator/catalyst	0.5	2

5.1 Plus (Manugistics, Inc. Rockville, MD, USA). The analysis of variance (ANOVA) provided a study of the variation present in the results of experiments carried out and the test of statistical significance, *p*-value, was determined according to the total error criteria considering a confidence level of 95%. The influence of a factor will be significant if the value of critical level (p) is lower than 0.05; discarding the meaningless parameters for *p*-values over 0.05 [19]. As a result of the RSM, an empirical model encompassing all the operating variables and their binary interactions was calculated. Nevertheless, once the factors with statistical significance in mass conversion and number-average molecular weight were determined, the rest of the meaningless information was deleted from this model, obtaining new equations, for X and M_n, which fitted the experimental data representing much correctly their scientific meaning and avoiding fitting terms for discarded variables or their interactions.

3. Results and discussion

As commented before, the effect of the operating variables (T, MC ratio and IC ratio) and their possible interactions on the mass conversion (X) and number-average molecular weight (M_n) were studied using a 23 full factorial design. The standard experimentation matrix is shown in Table 2. Columns 2 to 4 give the variable levels coded in the dimensionless coordinate while as columns 5 to 7 give the dimensional variable levels. Table 2 also shows the experimental values obtained for the selected responses (columns 8, 9, 11 and 12) together with theoretical number-average molecular weight (column 10) supposing activity of both active centres of $Zn(Oct)_2$ and calculated according to the following Equation (2) [15]:

$$M_{\text{theoretical}} = \frac{1}{2}\cdot\frac{M_n}{C}\cdot\frac{X[\%]}{100}\cdot M_{\text{weighted}} \quad (2)$$

where M/C is the molar ratio monomer to catalyst, M_n is the experimental number-average molecular weight, X is the total monomer conversion and M_{weighted} is a weighted molecular weight for a pseudo-monomer formed by a mixture of both comonomers, assuming that monomer mixture composition does not change along the reaction (80:20 for D,L-lactide and glycolide, respectively). So, for a conversion of 100% $M_{\text{theoretical}}$ should be 6900 approximately.

3.1. Statistical analysis in RSM: ANOVA test and evaluation of the effect of curvature

The analysis of main effects and their interactions for the chosen responses are shown in Table 3. Statistically significant effects are underlined according to *p*-values calculated.

In order to obtain correlations to predict the responses values along the interval studied, it is necessary to evaluate the curvature and the effect of curvature. Curvature (C) can be calculated as the difference between the mean value of the response analyzed considering all the experimental points (y_m) and the mean value of the response analyzed considering only the central points (y_{mCP}). Effect of curvature (EC) is obtained through the Equation (3):

$$EC = t\cdot s\cdot\sqrt{\frac{1}{N}+\frac{1}{r}} \quad (3)$$

Table 2. Experimental matrix and results for the full 2^3 factorial design[a]

Run	T [ºC]	M/C	I/C	T [ºC]	M/C	I/C	X	M [g/mol]	$M_{theoretical}$[b] [g/mol]	PDI[c]	L:G [%]
1	–1	–1	–1	120	100	0.5	0.65	13 700	4 500	1.67	72:28
2	+1	–1	–1	160	100	0.5	0.87	22 600	6 000	1.61	80:20
3	–1	+1	–1	120	500	0.5	0.87	12 900	29 500	1.66	71:29
4	+1	+1	–1	160	500	0.5	0.97	18 600	33 400	1.66	77:23
5	0	0	0	140	250	1	0.80	15 500	13 600	1.64	71:29
6	–1	–1	+1	120	100	2	0.69	11 100	4 700	1.53	69:31
7	+1	–1	+1	160	100	2	0.98	18 000	6 700	1.67	74:26
8	–1	+1	+1	120	500	2	0.40	3 600	13 500	1.49	61:39
9	+1	+1	+1	160	500	2	0.99	23 600	33 900	1.87	73:27
10	0	0	0	140	250	1	0.78	14 900	13 400	1.85	73:27

[a]Conditions for all experiments: Total monomers mixture weight, 100 g; molar ratio L:G = 80:20; stirring rate, 100 N; t = 3 h.

[b]$M_{theoretical}$ is the theoretical number-average molecular weight of PLGA and it has been calculated using Equation (2).

[c]PDI is the polydispersity index $\left(PDI=\frac{M_w}{M_n}\right)$, necessary together M_w or M_n to fully describe the morphology of the polymer chains in the molecular weight distribution.

Table 3. Estimated effects, interactions and ANOVA analysis from 2^3 factorial design for the polymerization system

Factor of interaction	X		M_n	
	Effects (±s)	p-Value	Effects (±s)	p-Value
T	0.3 (±0.014)	0.0019	10375 (±424.264)	0.0042
M/C	0.011689 (±0.014)	0.4603	–1575.47 (±424.264)	0.1433
I/C	–0.011689 (±0.014)	0.0297	–2742.29 (±424.264)	0.0545
T·M/C	0.045 (±0.014)	0.0740	2475 (±424.264)	0.0670
T·M/C	0.14 (±0.014)	0.0085	3075 (±424.264)	0.0450
M/C·M/C	–0.150563 (±0.014)	0.0073	691.823 (±424.264)	0.4129
T·M/C·I/C	0.105 (±0.014)	0.1490	4075 (±424.264)	0.0664

Table 4. Curvature and effect of curvature calculated for both responses

	y_m	y_{mCP}	Curvature (C)	Effect of curvature (EC)
X	0.8025	0.79	0.0125	0.0706
M_n	15512.5	15200	312.5	2117.7129

where *t* is the *t* parameter from the Student's t-distribution, *s* is the standard deviation, *N* is the number of experiments and *r* is the number of central points.

According to Table 4 the effect of curvature was not significant for any response. The lack of significance of the curvature indicates the validity of the pure design in the experimental range analyzed and shows that linear terms and their interactions are enough to describe the responses studied and, consequently, quadratic terms are not necessary.

3.2. Mass conversion

From results in Table 2 and using RSM (Table 3), the only factors affecting mass conversion are *T*, *IC* ratio, the binary interaction *T-IC* ratio and the binary interaction *MC-IC* ratio.

It can be concluded from the RSM that *T* is the main effect and it is positive along the interval. Obviously the polymerization reaction rate follows the Arrhenius Law and conversion increases for the same reaction time at higher temperatures. For that reason, in most of the experiments conversions above 0.95 are reached at 160ºC . However, for those experiments at 120ºC conversion falls down because the advance of the polymerization is much slower and conversion is still quite low at three hours.

The *IC* ratio had a negative effect according to Table 3. It can be explained taking into account that the initiator acts also as chain transfer agent. Its presence in the media favours the occurrence of termination reactions (chain transfer) which cuts the growth of the polymer chain even though a significant quantity of monomer remains in reaction medium. The observed effect is that the conversion decreases markedly. An excess of a chain transfer agent like methanol in the medium [15], which corresponds with *IC* ratio = 2 produces an early deceleration of the conversion growth.

Since both effects are opposed and a binary interaction *T-IC* ratio exists (Figure 5a), the combined effect of both produces different results depending on the considered level. As previously commented, temperature is the main effect according to RSM analysis. For that reason at the higher temperature level its effect on conversion prevail over the *IC* ratio because although there is an excess of methanol (initiator) in the reaction medium, the conversion reaches elevated values in a very short period of time. Nevertheless, for the low *T* level, the reaction rate is not fast enough to stand out its effect over higher values of *IC* ratio. As a result, the chain transfer reactions become more noticeable than polymerization reaction and the mass conversion

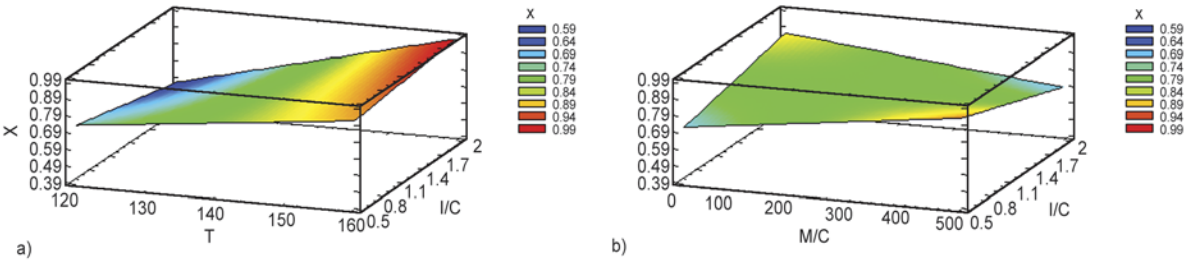

Figure 5. Response surfaces plot showing the combined effect *T-IC* ratio (a) and *MC-IC* ratios (b) on the mass conversion as a result of RSM analysis

decreases when *IC* ratio increases at this temperature.

Moreover, a binary interaction between *MC*-*IC* ratios also exists. In this case, the *MC* ratio has not signification and the results must be analyzed together *IC* ratio. Figure 5b shows the combined effect of both variables over the conversion. Mainly, the effect of a decrease in *MC* ratio, and therefore an increase in the quantity of catalyst added to the system, is an increase of conversion since polymerization rate is accelerated. Consequently, the effect is similar to previous interaction: at low *MC* ratios (high amount of catalyst in reaction medium) its effect is stronger than the effect of chain transference, so the mass conversion increases in all the interval of *IC* ratios. When *MC* ratio is high (low amount of catalyst) the chain growth is not so fast, so high values of *IC* ratio (large amounts of methanol which acts a chain transfer agent) produce a growth ineffective an earlier step of polymerization and as a consequence the mass conversion decreases.

As described before above, according to Table 4 the effect of curvature was no significant, indicating the validity of pure fractional design in the experimental range analyzed, so that second-order models were not necessary to describe the process. Equation (4) that relates the mass conversion to the independent variables can be expressed in the following terms:

$$X = -0.253 + 6.542\cdot10^{-3}\cdot T + 2.932\cdot10^{-3}\cdot\frac{M}{C} + 0.184\cdot\frac{I}{C} - 1.625\cdot10^{-5}\cdot T\cdot\frac{M}{C} - 5.833\cdot10^{-4}\cdot T\cdot\frac{I}{C} - 2.952\cdot10^{-3}\cdot\frac{M}{C}\cdot\frac{I}{C} + 1.750\cdot10^{-5}\cdot T\cdot\frac{M}{C}\cdot\frac{I}{C} \quad (4)$$

where the values of all variables are specified in their original units.

3.3. Number-average molecular weight

According to data shown in Table 2 and using RSM (Table 3), the more influential factor on the molecular weight is *T* together to the binary interaction *T*-*IC* ratio. In this case, the effect of temperature is also positive according to Arrhenius equation due to an increase in the polymerization rate promotes the chains growth and, consequently, their molecular weight.

Analogously to the previous section and according to Figure 6, the binary interaction *T*-*IC* ratio has a similar positive effect in M_n and *X* during the polymerization process. Comparing Figure 6 with Figure 5a, this similarity can be easily understood taking into account that a larger extension of the polymerization can be evaluated through the mass conversion (based on the ratio between the amount of initiated chains in relation to the amount of unreacted monomer) or the molecular weight of the synthesized polymer. At higher temperatures its effect is more noticeable than the action of methanol as chain transfer agent even when a large amount is added to the system. Therefore, M_n is always increasing in all the interval of *IC* ratios. At low temperature, the tendency is the same although less marked that for the case of mass conversion: reaction rate is slower due to the Arrhenius Law and consequently any reaction of chain transfer produced by methanol (especially at higher *IC* ratios) stops the polymerization. In this case, the decreasing of M_n is minor and for that reason the slope of the response surface is less pronounced.

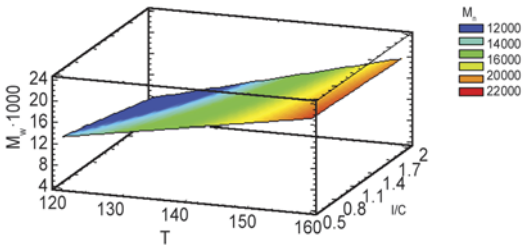

Figure 6. Response surface plot showing the combined effect of temperature together *IC* ratio on the number-average molecular weight

As it can be observed in Table 2, the experimental M_n values resulted quite low in comparison to theoretical *M* in experiments with *MC* ratio of 500. A possible explanation for these low molecular weights could be in the few quantity of catalyst employed that limits the conversion of zinc octoate into zinc alkoxide for the initiation reaction (Figure 2). This fact generates a competition between this reaction and other secondary reactions (transesterification, interesterification) that could be produced even by impurities or humidity traces in the polymerization mixture [20]. It would justify the negative influence of *MC* ratio although it has not signification in the statistical analysis. On the contrary, for experiments carried out with *MC* values of 100 the quantity of catalyst is not a limiting reagent in the reaction. In this case, experimental M_n values are significantly larger than theoretical ones which means that only

takes place the substitution of one carbolixate group from $Zn(Oct)_2$ for one methoxide group of initiator [21].

Due to the lack of significance of the effect of curvature, the fitting of data to a first-order model gave as a result an empirical relationship between the dependent variable M_n and the independent variables described by the Equation (5):

$$M_n = -21\,392.400 + 292.125 \cdot T + 68.720 \cdot \frac{M}{C} + 11\,655 \cdot \frac{I}{C} - 0.540 \cdot T \cdot \frac{M}{C} - 101.250 \cdot T \cdot \frac{I}{C} - 92.777 \cdot \frac{M}{C} \cdot \frac{I}{C} + 0.679 \cdot T \cdot \frac{M}{C} \cdot \frac{I}{C} \quad (5)$$

where the values of all variables are specified in their original units.

3.4. Equations fitting according the significant effects and comparison of predicted parameters with experimental values

Equations (4) and (5) have been considered as a result of applying the RSM. Once they were calculated, the non-influential effects were deleted in them and consequently changing into Equations (6) and (7) respectively:

$$X = -0.438 + 1.667 \cdot 10^{-3} \cdot T - 0.551 \cdot \frac{I}{C} + 4.667 \cdot 10^{-3} \cdot T \cdot \frac{I}{C} - 5.020 \cdot 10^{-4} \cdot T \cdot \frac{M}{C} \cdot \frac{I}{C} \quad (6)$$

$$M_n = -2925 + 131.250 \cdot T - 14350 \cdot \frac{I}{C} + 102.500 \cdot T \cdot \frac{I}{C} \quad (7)$$

These new equations gave different predicted values which were compared with the experimental ones according to Figure 7. Residuals of values given by both models versus fitted values were graphically represented. As it can be appreciated, the values predicted with the Run 2 fitted the experimental ones reasonably (the best accuracy was obtained with the mass conversion model) and additionally the scientific meaning with respect to the Run 1 was improved. If the residuals of both Runs are analyzed, it can be appreciated that the variability of the simplified model is slightly greater although the tendency continues to be linear, the residuals are quite symmetrical and there is no heteroscedasticity. Therefore, the acceptance of the model has been confirmed.

3.5. Global optimization of the polymerization process

From previous results, the optimization of polymerization process for variables X and M_n cannot be performed in a separated way due to different tendencies in the effects of the studied parameters depending on the range values. For that reason it is necessary to optimize the values of T, MC ratio and IC ratio in order to select the best operation conditions in the experimental range analyzed.

Regarding to the mass conversion of polymer, a high value is desired since it minimizes the quantity of unreacted monomer as potential impurity which could perturb the drug release process. The appropriate conditions which achieve this criterion included to work at high temperature (160ºC) and to use values of MC and IC ratios which do not promote the competition of the initiation step of polymerization with other ones and do no generate an

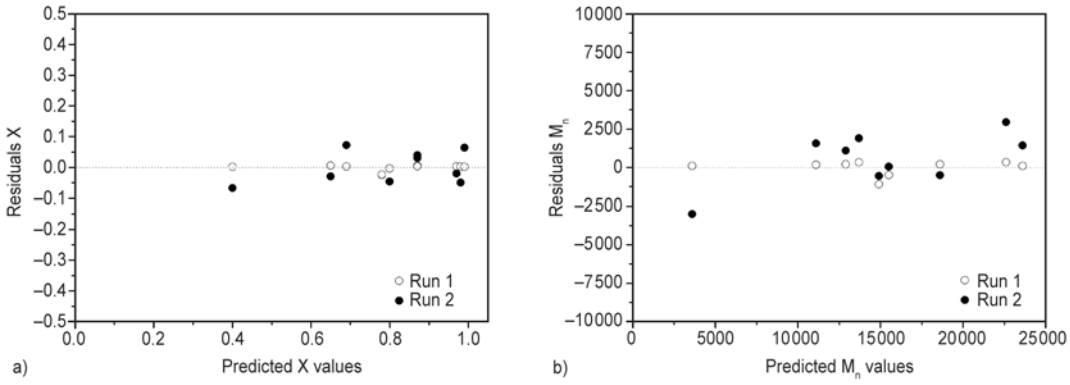

Figure 7. Graphical representation of residuals given by both models versus fitted values for: (a) X; (b) M_n. Empty circles corresponds to the first run of the model and filled circles corresponds to the second run

excess of methanol that acts as a chain transfer agent. Namely, values of 100 and 0.5 for *MC* ratio and *IC* ratio respectively.

However, in relation to M_n and according not only to the specific polymer characteristics but their subsequent use as biodegradable scaffold in controlled drug release, it is not necessary to achieve its maximum value. Authors [22–25] use a wide variety of values of PLGA molecular weight for this purpose, although molecules of PLGA with molecular weight values around 20000 seem to be suitable for their use in controlled drug release [26, 27]. So as long as a temperature of 160ºC is selected, this target value is reached and any value of *MC* ratio or *IC* ratio would be appropriate.

Finally, in order to determine globally the best operating conditions, it is necessary to consider copolymer composition because it plays a relevant role due to its influence to modulate the degradation rate of the scaffold [17]. For this reason, this variable should be taken into account. According to literature [22, 28, 29], L:G molar compositions of PLGA of 50:50, 85:15 and 75:25 are widely used and ratios around 75:25 are highly desirables since they achieve high control on the degradation rates [17]. From Table 2, the experimental conditions which accomplish all the previous requirements of mass conversion, number-average molecular weight and copolymer composition are: 160ºC, *MC* ratio of 100 and *IC* ratio of 2, and they can be determined as the optimal polymerization conditions.

4. Conclusions

RSM has been used in this work to screen variables affecting copolymerization in bulk of D,L-lactide and glycolide, to estimate the main effects caused by these variables individually and by their interaction and to develop an empirical model to optimize the resultant copolymer in order to get the best option for its subsequent use as tissue scaffold and drug release device. This model provides a practical tool in order to avoid a rigorous mechanistic study of the polymerization in this preliminary step of the research.

The regression models proposed to predict mass conversion (X) and number-average molecular weight (M_n) were found to fit experimental data properly after identified the experimental variables statistically significant and simplified the model only using them.

Temperature of 160ºC and molar *MC* ratio and *IC* ratio of 100 and 2 respectively were selected as the optimal experimental variables in order to maximize the value of X and produce a relatively high M_n, producing the appropriate PLGA for the subsequent stages of the synthesis of biodegradable scaffolds.

Acknowledgements

Financial support from JCCM project PBI05–014 is gratefully acknowledged.

References

[1] Davis S. S., Illum L., Stolnik S.: Polymers in drug delivery. Current Opinion in Colloid and Interface Science, **1**, 660–666 (1996). DOI: 10.1016/S1359-0294(96)80105-1

[2] Gilding D. K., Reed A. M.: Biodegradable polymers for use in surgery–polyglycolic/poly(actic acid) homo- and copolymers: 1. Polymer, **20**, 1459–1464 (1979). DOI: 10.1016/0032-3861(79)90009-0

[3] Temenoff J. S., Mikos A. G.: Review: Tissue engineering for regeneration of articular cartilage. Biomaterials, **21**, 431–440 (2000). DOI: 10.1016/S0142-9612(99)00213-6

[4] Okada M.: Chemical syntheses of biodegradable polymers. Progress in Polymer Science, **27**, 87–133 (2002). DOI: 10.1016/S0079-6700(01)00039-9

[5] Kricheldorf H. R.: Syntheses and application of polylactides. Chemosphere, **43**, 49–54 (2001). DOI: 10.1016/S0045-6535(00)00323-4

[6] Kricheldorf H. R., Bornhorst K., Hachmann-Thiessen H.: Bismuth(III) *n*-hexanoate and tin(II) 2-ethylhexanoate initiated copolymerizations of ε-caprolactone and L-lactide. Macromolecules, **38**, 5017–5024 (2005). DOI: 10.1021/ma047873o

[7] Kowalski A., Duda A., Penczek S.: Kinetics and mechanism of cyclic esters polymerization initiated with tin(II) octoate, 1. Polymerization of ε-caprolactone. Macromolecular Rapid Communications, **19**, 567–572 (1998). DOI: 10.1002/(SICI)1521-3927(19981101)19:11<567::AID-MARC567>3.0.CO;2-T

[8] Jerôme R., Lecomte P.: New developments in the synthesis of aliphatic polyesters by ring-opening polymerisation. in 'Biodegradable polymers for industrial applications' (ed.: Smith R.). Woodhead Publishing Limited, Cambridge, Vol 1, 77–106 (2005).

[9] Kowalski A., Libiszowski J., Majerska K., Duda A., Penczek S.: Kinetics and mechanism of ε-caprolactone and L,L-lactide polymerization coinitiated with zinc octoate or aluminum acetylacetonate: The next proofs for the general alkoxide mechanism and synthetic applications. Polymer, **48**, 3952–3960 (2007). DOI: 10.1016/j.polymer.2007.05.007

[10] Mazarro R., Cabezas L. I., de Lucas A., Gracia I., Rodríguez J. F.: Study of different catalysts and initiators in bulk copolymerization of D,L-lactide and glycolide. Journal of Macromolecular Science Part A: Pure and Applied Chemistry, **46**, 1049–1059 (2009). DOI: 10.1080/10601320903252090

[11] Cabezas L. I., Fernández V., Gracia I., de Lucas A., Rodríguez J. F.: Production of biodegradable porous scaffolds impregnated with indomethacin in supercritical CO_2. Journal of Supercritical Fluids, **63**, 155–160 (2012). DOI: 10.1016/j.supflu.2011.12.002

[12] Cabezas L. I., Gracia I., García M. T., de Lucas A., Rodríguez J. F.: Production of biodegradable porous scaffolds impregnated with 5-fluorouracil in supercritical CO_2. Journal of Supercritical Fluids, **80**, 1–8 (2013). DOI: 10.1016/j.supflu.2013.03.030

[13] Mazarro R., de Lucas A., Gracia I., Rodríguez J. F.: Copolymerization of D,L-lactide and glycolide in supercritical carbon dioxide with zinc octoate as catalyst. Journal of Biomedical Materials Research Part B: Applied Biomaterials, **85**, 196–203 (2008). DOI: 10.1002/jbm.b.30936

[14] Mazarro R., de Lucas A., Gracia I., Rodríguez J. F.: Kinetic study of D,L-lactide and glycolide homopolymerizations by differential scanning calorimetry. Macromolecular Chemistry and Physics, **209**, 818–824 (2008). DOI: 10.1002/macp.200700527

[15] Mazarro R., de Lucas A., Cabezas L. I., Gracia I., Rodríguez J. F.: Influence of the operative conditions on the characteristics of poly(D,L-lactide-co-glycolide) synthesized in supercritical carbon dioxide. Macromolecular Symposia, **287**, 111–118 (2010). DOI: 10.1002/masy.201050116

[16] Mazarro R., Gracia I., Rodríguez J. F., Storti G., Morbidelli M.: Kinetics of the ring-opening polymerization of D,L-lactide using zinc (II) octoate as catalyst. Polymer International, **61**, 265–273 (2012). DOI: 10.1002/pi.3182

[17] Miller R. A., Brady J. M., Cutright D. E.: Degradation rates of oral resorbable implants (polylactates and polyglycolates): Rate modification with changes in PLA/PGA copolymer ratios. Journal of Biomedical Materials Research, **11**, 711–719 (1977). DOI: 10.1002/jbm.820110507

[18] Box J. E. P., Hunter W. G., Hunter J. S.: Statistics for experimenters: An introduction to design, data analysis and model building. Wiley, New York (1978).

[19] Box J. E. P., Hunter W. G., Hunter J. S.: Statistics for experimenters: Design, discovery and innovation. Wiley, New Jersey (2005).

[20] Libiszowski J., Kowalski A., Duda A., Penczek S.: Kinetics and mechanism of cyclic esters polymerization initiated with covalent metal carboxylates, 5. End-group studies in the model ε-caprolactone and L,L-dilactide/Tin(II) and zinc octoate/butyl alcohol systems. Macromolecular Chemistry and Physics, **203**, 1694–1701 (2002). DOI: 10.1002/1521-3935(200207)203:10/11<1694::AID-MACP1694>3.0.CO;2-J

[21] Biela T., Kowalski A., Libiszowski J., Duda A., Penczek S.: Progress in polymerization of cyclic esters: Mechanisms and synthetic applications. Macromolecular Symposia, **240**, 47–55 (2006). DOI: 10.1002/masy.200650807

[22] Holy C. E., Dang S. M., Davies J. E., Shoichet M.: S. *In vitro* degradation of a novel poly(lactide-co-glycolide) 75/25 foam. Biomaterials, **20**, 1177–1185 (1999). DOI: 10.1016/S0142-9612(98)00256-7

[23] Miyajima M., Koshika A., Okada J., Kusai A., Ikeda M.: The effects of drug physico-chemical properties on release from copoly (lactic/glycolic acid) matrix. International Journal of Pharmaceutics, **169**, 255–263 (1998). DOI: 10.1016/S0378-5173(98)00133-1

[24] Siegel S. J., Kahn J. B., Metzger K., Winey K. I., Werner K., Dan N.: Effect of drug type on the degradation rate of PLGA matrices. European Journal of Pharmaceutics and Biopharmaceutics, **64**, 287–293 (2006). DOI: 10.1016/j.ejpb.2006.06.009

[25] Dorta M. J., Santoveña A., Llabrés M., Fariña J. B.: Potential applications of PLGA film-implants in modulating *in vitro* drugs release. International Journal of Pharmaceutics, **248**, 149–156 (2002). DOI: 10.1016/S0378-5173(02)00431-3

[26] Schliecker G., Schmidt C., Fuchs S., Wombacher R., Kissel T.: Hydrolytic degradation of poly(lactide-co-glycolide) films: Effect of oligomers on degradation rate and crystallinity. International Journal of Pharmaceutics, **266**, 39–49 (2003). DOI: 10.1016/S0378-5173(03)00379-X

[27] Kou J. H., Emmett C., Shen P., Aswani S., Iwamoto T., Vaghefi F., Cain G., Sanders L.: Bioerosion and biocompatibility of poly(*d*,*l*-lactic-co-glycolic acid) implants in brain. Journal of Controlled Release, **43**, 123–130 (1997). DOI: 10.1016/S0168-3659(96)01477-0

[28] Sheridan M. H., Shea L. D., Peters M. C., Mooney D. J.: Bioabsorbable polymer scaffolds for tissue engineering capable of sustained growth factor delivery. Journal of Controlled Release, **64**, 91–102 (2000). DOI: 10.1016/S0168-3659(99)00138-8

[29] Lu L., Peter S. J., Lyman M. D., Lai H-L., Leite S. M., Tamada J. A., Uyama S., Vacanti J. P., Langer R., Mikos A. G.: *In vitro* and *in vivo* degradation of porous poly(DL-lactic-*co*-glycolic acid) foams. Biomaterials, **21**, 1837–1845 (2000). DOI: 10.1016/S0142-9612(00)00047-8

eXPRESS Polymer Letters Vol.7, No.11 (2013) 895–899
Available online at www.expresspolymlett.com
DOI: 10.3144/expresspolymlett.2013.87

Advantages of polycarboxylic over dicarboxylic anhydrides in the melt modification of PPC

C. Barreto[1,2], *E. Hansen*[1], *S. Fredriksen*[2*]

[1]University of Oslo, Department of Chemistry Postboks 1033 Blindern, NO 0315 Oslo, Norway
[2]Norner AS, Department of Polymer Research, Asdalstrand 291. NO 3960 Stathelle, Norway

Received 27 May 2013; accepted in revised form 14 July 2013

Abstract. We present an alternative polymer modification of poly (propylene carbonate) (PPC). A conventional practice for PPC melt processing is the melt – modification with maleic anhydride (MAH) – a di-carboxylic anhydride –. In our work, PPC is melt-modified with pyromellitic di-anhydride (PDAH) – a tetra-carboxylic dianhydride –. Using MAH modified PPC as reference, the polymer degradation and the thermal and viscoelastic properties of the materials are studied. Both anhydrides after their melt compounding have similar efficiency in the conservation of the molecular weight. Strikingly, the use of PDAH is advantageous over MAH considering the improvement of the thermal stability, the decrease of the complex melt viscosity and higher storage modulus (stiffness) of the modified PPC. It is speculated that the changes in the material performance arise from the occurrence of long chain branching and non-covalent interactions from the PDAH modifier.

Keywords: *mechanical properties, thermal properties, pyromellitic dianhydride, polymer stability, poly(propylene carbonate)*

1. Introduction

The transformation of carbon dioxide as a low cost monomer into useful materials like poly (alkylene carbonates) for packaging and consumer goods, has been globally proposed by industry and academia as a contribution to the mitigation of the greenhouse effect [1]. Poly(propylene carbonate) (PPC), the most studied of these polymers, faces multiple challenges when it comes to material properties and processing, in particular with respect to its mechanical properties, warpage and polymer degradation upon melting extrusion [2–5]. The esterification of the hydroxyl end groups of PPC using *i.e.* maleic anhydride (MAH), a dicarboxylic anhydride, has proven successful to mitigate the thermal degradation via chain unzipping and minimize the loss of molecular weight during extrusion [2–8]. Using anhydrides containing three or more carboxylic groups, like the tetra-carboxylic pyromellitic dianhydride (PDAH), has however not been reported. In this short communication we want to report some advantages found for PDAH over MAH as melt modifiers of PPC, based on characterizations of the polymer stability, and the viscoelastic and thermal properties.

2. Material and methods

2.1. Sample preparation

PPC pellets (QPAC40 from Empower Materials, USA) (4.8% propylene carbonate) were dried under dry N_2 atmosphere at 25°C for 72 h prior to use. PDAH (Cat. # 412287, M_W 218.32, 97%, Sigma Aldrich, Germany) and MAH (Cat. # 63200, M_W 98.06, 99%, Sigma Aldrich, Germany). PPC pellets (300 g) and anhydride powder (0.1, 0.5, 1.0 and 3.0 wt%) was premixed and fed in a Prism Eurolab16 twin screw compounder (Thermo Electron Corporation, UK, Barrel *D:* 16 mm, *L*/*D*: 25, feed-

*Corresponding author, e-mail: siw.fredriksen@norner.no

ing speed: 2 kg/h, screw speed: 500 r.p.m, barrel and die temperature: 140°C). The extrudate was cooled by water, cut into pellets and dried under dry N_2. The initial and final portions of the extrudate were discarded and approximately 120 g of each melt compounded recipe was collected.

2.2. Characterization methods

Rheology: Complex viscosity (η^*), was measured within the linear viscoelastic range using the Rheometrics Scientific RDA II Analyzer, equipped with plate-plate geometry (diameter 25 mm), on hot pressed specimens (diameter 25 mm). Preheating time of 200 s, frequency interval 0.06 to 15.85 rad/s for isothermal/isostrain measurements at 140°C/10% was used.

TGA: Thermogravimetric analysis thermograms were recorded in a TGA Q500 instrument from TA Instruments in accordance to ISO 11358, using 3 mm diameter disks approximately of 10 mg, cut from plates 1 mm thick hot pressed at 150°C. Constant flow of N_2 was used during 5 min purging period and during the analysis. TGA runs were recorded over a temperature interval of 25–425°C using a heating rate of 10°C/min. The characterizations were made following the ICTAC guidelines for data acquisition [9].

GPC: The molecular-weight distribution was determined by size-exclusion chromatography (SEC). The analyses were performed in an Agilent PL-GPC 50 equipped with a refractive index detector and calibrated with narrow polystyrene standards using THF as the eluent at 40°C (triplicate measurements).

DMTA: Dynamic mechanical thermal analysis characterizations were performed in a DMA Q800 from TA Instruments using a single-cantilever fixture. Storage and loss moduli, E' and E'', were measured within the linear viscoelastic range. The scanned interval was –5 to 70°C using a dynamic strain of 0.01% and a frequency of 1 Hz; the test specimens were 2 mm × 5 mm × 25 mm strips cut from hot-pressed films at 150°C (triplicate measurements).

3. Results and discussion

The characterization of anhydride melt modified PPC (PPCMA: MAH modified, and PPCPA: PDAH

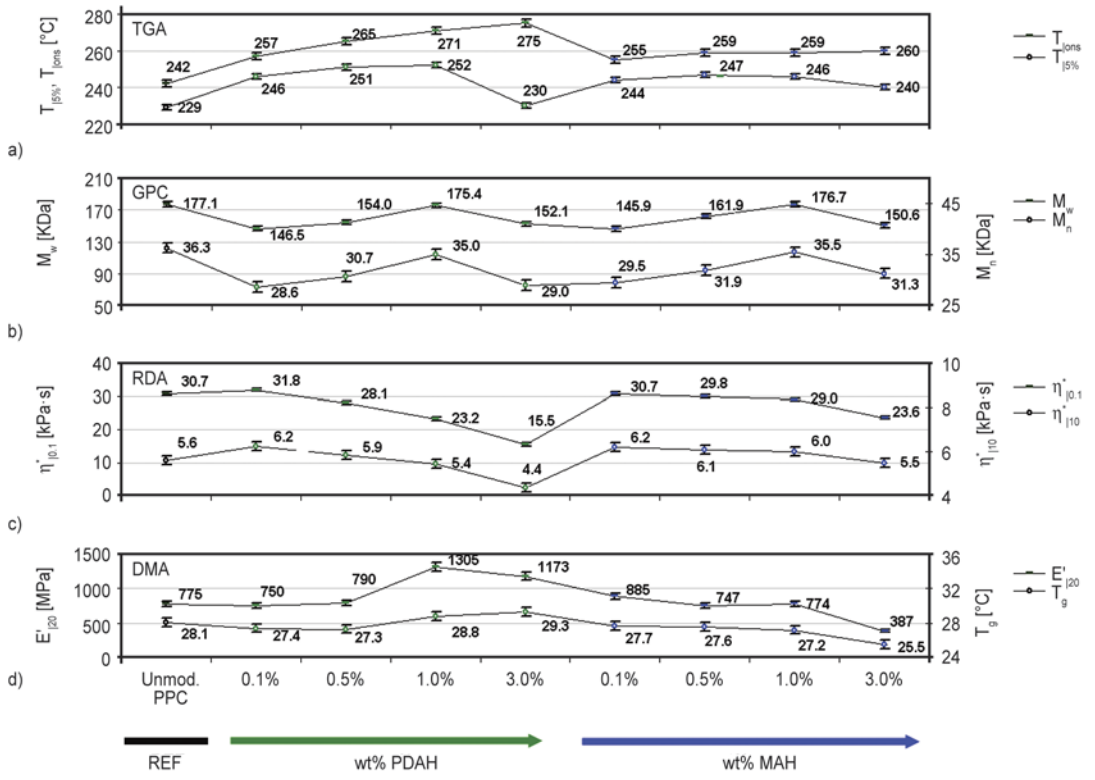

Figure 1. Characterization of unmodified PPC and melt modified PPC with maleic anhydride (MAH) and pyromellitic dianhydride (PDAH) at various wt% loadings. a) TGA: N_2 10°C/min, $T_{|5\%}$ [°C]: temperature at 5 wt% loss, $T_{|ons}$ [°C]: temperature at the onset of the main thermal decomposition. b) GPC: M_n [kDa]: molecular weight in number, M_w [kDa]: molecular weight in weight. c) RDA: $\eta^*_{|0.1}$ and $\eta^*_{|10}$ [kPa·s]: complex viscosity at 0.1 and 10 rad/s. d) DMA: T_g [°C]: glass transition temperature, $E'_{|20}$ [MPa]: storage modulus at 20°C

modified) by SEC, RDA, DMTA and RDA is shown in Figure 1. Reference samples are unmodified PPC (not extruded). The TGA parameters (Figure 1a) show the expected increase in the thermal stability for PPC after the addition of MAH and PDAH. At the highest level of anhydride addition (3 wt%), $T_{|5\%}$ decreases for both MAH and PDAH and $T_{|ons}$ increases steadily, clearly indicating the occurrence of degradation via chain unzipping (ChUz) probably caused by the excess of acidity in the system. This behavior at the 3 wt% level is consistent with the drop in the molecular weight M_n and M_w (Figure 1b), the decrease of the complex viscosity ($\eta^*_{|0.1}$ and $\eta^*_{|10}$) (Figure 1c), and the stiffness ($E'_{|20}$ in Figure 1d).

The stoichiometric amounts required to complete the end capping in both polymer ends correspond approximately to 0.3 wt% loading for both anhydrides. Hence, a stoichiometric excess of acid equivalents are present in most of the samples. Further, it may be assumed that incomplete end capping happens in practice due to, *e.g.*, short residence time and incomplete mixing in the compounder. Therefore, the improvement of properties approximately above 0.3 wt% anhydride are assumed to be explained also by non-covalent interactions between the unreacted anhydrides and the polymer chains or among unreacted anhydrides, *e.g.*, hydrogen bonding and other non-covalent interactions (*vide infra*).

One of the major concerns regarding PPC compounding is the polymer degradation due to simultaneous thermal and mechanical (shear) degradation. Random chain scission (RCS) and ChUz of freshly generated hydroxyl chain ends is commonly evidenced in our work with end capped PACs. This shear dependent process affects in particular the high molecular weight fraction of the polymer as evidenced from the higher drop of M_w compared to M_n (Figure 1b). Both anhydrides act as chain extenders or chain healers as evidenced by the observed mitigation of the molecular weight decrease, similar to previously reported for MAH [7]. The chain healing process is depicted in Figure 2 and can be described as follows: during PPC extrusion in the absence of any anhydride, RCS occurs and new hydroxyl end groups are generated (Figure 2a). These end groups cause increase in the ChUz with the concomitant formation of cyclic propylene carbonate (CPC). In the presence of a di or tetra carboxylic compound like MAH or PDAH (Figure 2b–2c), the hydroxyl ends react with the carboxyl moieties in two ways. On the one hand, end capping occurs for the free polymer ends thus reducing ChUz in the conventional way. On the other hand, it is suggested that the anhydrides participate in a 'healing' reaction that remedies the molecular weight drop caused by the RCS. The chain 'healing efficiency' is similar for both anhydrides as seen from the similar values of M_n and M_w at the same level of anhydride. This fact suggests that the esterification rate for the two anhydrides with PPC is similar under the conditions used. The molecular weight conservation can be expected at slightly higher levels than 1 wt% of anhydride.

PPC containing CPC is soft since the latter has a plasticizing effect. The polymer softness leads to warpage and shrinkage of PPC items that have been processed by conventional polymer converting techniques like injection molding. Therefore, it is desirable to increase the polymer stiffness in order to

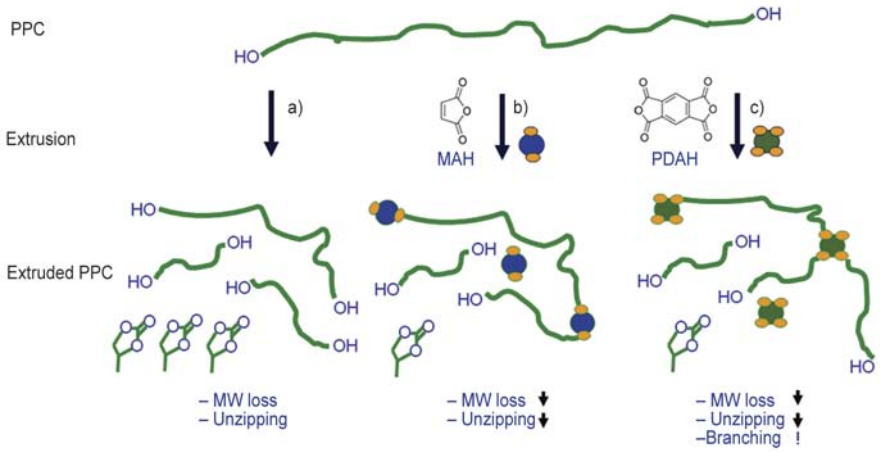

Figure 2. Hypothetical reaction paths during reactive extrusion in absence of additives a), in presence of dicarboxylic mono-anhydride (MAH) b) and tetracarboxylic di-anhydride (PDAH) c)

counteract the relaxation of the built up internal stresses in order to mitigate these phenomena. The storage modulus ($E'_{|20}$), a measure of the stiffness, shows that PDAH contributes to increased stiffness (Figure 1d). The presence of more than two carboxylic groups in PDAH may allow the tethering of multiple PPC chains to a single dianhydride molecule (Figure 2c). Also, the slight modification of T_g that is observed follows the trend for $E'_{|20}$. It is worthwhile to mention that the resulting modified polymer samples are fully thermoplastic, and fully soluble in acetone which allows discarding the occurrence of strong crosslinking. Instead this behavior suggests that the improved mechanical properties may arise from branching from at least three PPC chains tethered to a PDAH molecule (Figure 2c). This hypothesis is also supported from previous work on chain extension in PLA in which the addition of polyfunctional chain extenders with isocyanide or epoxy moieties result in branched polymer structures [10, 11]. Maleic anhydride reinforces the polymer at low loadings but softens the polymer at higher level. The drop in stiffness with increasing MAH loading is opposite to previous observations [7]. In our work it appears that the coupling of two maleate moieties which allows branching and explains the increase of stiffness in previous work [7] is a reaction of low significance. The changes in $E'_{|20}$ and T_g could also be understood as the result of a varying content of CPC in the samples. However, when evaluating the CPC content in the samples modified with 1.0 wt% of PDAH and MAH, both show insignificant differences in the CPC level. This observation allows discarding any significant effect of the CPC content in the changes in $E'_{|20}$ and T_g of samples modified with similar levels of both anhydrides under discussion. The characterization of CPC was done by ^{1}H-NMR however, for brevity, was not included.

When checking the DMA and TGA characterization of samples, the dissimilar modification of the thermal stability and stiffness may also be explained from non-covalent interactions. Hydrogen bonding has been reported to contribute to both performances in PPC [12, 13]. Also considering the presence of aromatic rings from PDAH, interactions with the π electron cloud (π–carbonyl, π–carboxyl or π–π interactions [14]) could also be the origin of the improvements observed in these properties. The changes in $T_{|ons}$ from TGA reveals the changes in the ability of the polymer to undergo degradation *via* RChSc. The samples modified by PDAH show higher values in this parameter which is a sign of different levels of thermal stabilization as the result of the modification of non-covalent interactions.

The thermomechanical properties of PPC may also be enhanced by the compounding with organic and inorganic micro- and nanofillers. This commonly results in a steep increase of the melt viscosity, which affects the processing performance of the resulting compounds. A lower melt viscosity of the resin can be achieved by decreasing the molecular weight, but this is most often undesired. Preferably, the final molecular weight should be high while at the same time decreasing the melt viscosity to facilitate processing. This type of performance is achieved after the compounding of PPC with anhydrides, evidenced from the drop of the complex viscosity both at high and low shear (Figure 1c). Taking into account the mitigation of the molecular weight drop when increasing the anhydride loading (Figure 1b), the observed decrease of the complex viscosity can clearly not be linked to the decrease of the molecular weight. These facts allow speculating on the polymer structural reconformation and/or the modification of the secondary interactions with the anhydrides.

4. Conclusions

The melt modification with multifunctional carboxylic anhydrides like PDAH is a useful tool in high-shear melt processing of PPC. It is found that this alternative compared to the modification with MAH improves the stiffness, the thermal stability and decreases the melt viscosity of PPC while mitigates the molecular weight drop caused by shear. It is suggested that in addition to conventional end-capping, branching due to the tethering of more than two PPC chains to a single anhydride molecule, and the influence of non-covalent interactions may explain these results.

Acknowledgements

This work was funded with resources of the GASSMAKS program of the Research Council of Norway, and from Norner AS. The authors gratefully acknowledge the Scientific Laboratories at Norner AS for the sample characterizations.

References

[1] Aresta M.: Carbon dioxide as chemical feedstock. Wiley, Weinheim (2010).

[2] Dixon D. D., Ford M. E., Mantell G. J.: Thermal stabilization of poly(alkylene carbonate)s. Journal of Polymer Science: Polymer Letters Edition, **18**, 131–134 (1980).
DOI: 10.1002/pol.1980.130180210

[3] Inoue S., Tsuruta T., Takada T., Miyazaki N., Kambe M., Takaoka T.: Synthesis and thermal degradation of carbon dioxide-epoxide copolymer. Applied Polymer Symposium, **26**, 257–267 (1975).

[4] Luinstra G., Borchardt E.: Material properties of poly (propylene carbonates). Advances in Polymer Science, **245**, 29–48 (2012).
DOI: 10.1007/12_2011_126

[5] Luinstra G. A.: Poly(propylene carbonate), old copolymers of propylene oxide and carbon dioxide with new interests: Catalysis and material properties. Polymer Reviews, **48**, 192–219 (2008).
DOI: 10.1080/15583720701834240

[6] Peng S., An Y., Chen C., Fei B., Zhuang Y., Dong L.: Thermal degradation kinetics of uncapped and end-capped poly(propylene carbonate). Polymer Degradation and Stability, **80**, 141–147 (2003).
DOI: 10.1016/S0141-3910(02)00395-6

[7] Yao M., Mai F., Deng H., Ning N., Wang K., Fu Q.: Improved thermal stability and mechanical properties of poly(propylene carbonate) by reactive blending with maleic anhydride. Journal of Applied Polymer Science, **120**, 3565–3573 (2011).
DOI: 10.1002/app.33565

[8] Zhang Z., Shi Q., Peng J., Song J., Chen Q., Yang J., Gong Y., Ji R., He X., Lee J-H.: Partial delamination of the organo-montmorillonite with surfactant containing hydroxyl groups in maleated poly(propylene carbonate). Polymer, **47**, 8548–8555 (2006).
DOI: 10.1016/j.polymer.2006.09.041

[9] Vyazovkin S., Burnham A. K., Criado J. M., Perez-Maqueda L. A., Popescu C., Sbirrazzuoli N.: ICTAC Kinetics Committee recommendations for performing kinetic computations on thermal analysis data. Thermochimica Acta, **520**, 1–19 (2011).
DOI: 10.1016/j.tca.2011.03.034

[10] Corre Y-M., Maazouz A., Duchet J., Reignier J.: Batch foaming of chain extended PLA with supercritical CO_2: Influence of the rheological properties and the process parameters on the cellular structure. The Journal of Supercritical Fluids, **58**, 177–188 (2011).
DOI: 10.1016/j.supflu.2011.03.006

[11] Di Y., Iannace S., Di Maio E., Nicolais L.: Reactively modified poly(lactic acid): Properties and foam processing. Macromolecular Materials Engineering, **290**, 1083–1090 (2005).
DOI: 10.1002/mame.200500115

[12] Chen L., Qin Y., Wang X., Li Y., Zhao X., Wang F.: Toughening of poly(propylene carbonate) by hyperbranched poly(ester-amide) via hydrogen bonding interaction. Polymer International, **60**, 1697–1704 (2011).
DOI: 10.1002/pi.3132

[13] Yu T., Zhou Y., Zhao Y., Liu K., Chen E., Wang D., Wang F.: Hydrogen-bonded thermostable liquid crystalline complex formed by biodegradable polymer and amphiphilic molecules. Macromolecules, **41**, 3175–3180 (2008).
DOI: 10.1021/ma7020562

[14] Gautrot J. E., Hodge P., Cupertino D., Helliwell M.: Experimental evidence for carbonyl–π electron cloud interactions. New Journal of Chemistry, **30**, 1801–1807 (2006).
DOI: 10.1039/b608628d

eXPRESS Polymer Letters Vol.7, No.11 (2013) 900–909
Available online at www.expresspolymlett.com
DOI: 10.3144/expresspolymlett.2013.88

Controlled anisotropic wetting behaviour of multi-scale slippery surface structure of non fluoro polymer composite

B. N. Sahoo, B. Kandasubramanian[*]*, B. Sabarish*

Department of Materials Engineering, Defence Institute of Advanced Technology, Girinagar, 411025 Pune, India

Received 2 May 2013; accepted in revised form 22 July 2013

Abstract. A facile process for in-situ modification of surface properties of Waste Expanded Polystyrene (WEP)/graphite film produced by spin coating technique has been described. The additives undergo spontaneous surface agglomeration with formation of islands of forest of flake structure during the spinning process. This results in polymer films with enhanced roughness and highly hydrophobic surfaces. Wettability was analyzed using static water contact angle, surface morphology was observed using atomic force microscopy (AFM) and field emission scanning electron microscopy (FE-SEM). The polymer composite exhibited maximum water contact angle (WCA) of 129°. Surface texture reveals the variation of surface roughness which enables anisotropic surface wettability property. The present work exhibits promising approach for fabricating nano flake forest in polymer structures for various industrial applications.

Keywords: *polymer composites, recycling, coatings, thin film, flake*

1. Introduction

Inspired by biological materials, effort has been made to replicate similar technology. Active research on wettability property finds tremendous applications in key industries and in daily life, which is precisely controlled by geometrical pattern and chemical composition of the surface. The self-cleaning property of good water repellent surface with water contact angle of more than 150° and angle of hysteresis less than 10° has stimulated researchers to replicate multifunctional properties of natural materials for fabricating artificial superhydrophobic surfaces [1–4]. The water wettability is determined by water-material interaction and surface morphology [5]. Superhydrophobic surfaces have received great interest due to their multifunctional applications in different areas such as self-cleaning, anticorrosion, drag reduction, ice-mitigation, window glasses, anti-icing textile, micro/macro fluid channels, optical devices, electronic and photonic material chemical sensors etc. [6–11]. Slippery surfaces are generally obtained by a combination of low surface energy materials and hierarchal structures, with trapped air pockets on which water droplets forms a liquid ball [12–17]. Earlier investigations on the surface texture of hydrophobicity were reported in terms of Wenzel and Cassie-Baxter model considering the water wettability of solid surface. Since then, low surface energy materials and fabrication techniques have been explored to design and create superhydrophobic surfaces [18, 19].

Nanostructured superhydrophobic surfaces have been fabricated using silica based materials and tridecafluoro-1,1,2,2-tetrahydrooctyldimethylchlorosilane (TFCS, $CF_3(CF_2)_5(CH_2)_2(CH_3)_2SiCl$) through dip coating technique [20]. Shang *et al*. [21] have fabricated superhydrophobic silica film on glass substrates using polystyrene particles and DFMS (dodecafluoroheptyl-methyl-dimethoxysilane) as low surface energy material. Superhydrophobic sur-

[*]Corresponding author, e-mail: meetkbs@gmail.com

faces using sodium chloride, sodium nitrate followed by fluorination treatment exhibiting water contact angle of 166° [22, 23]. Each technique so far invented requires significant advancement and innovation in fabrication process and materials for real and exact industrial applications of superhydrophobic surfaces.

Considerable attention has been drawn on fabrication of hydrophobic surface using polymer/clay nanocomposite structures. Uniformly dispersed clay either as intercalated or delaminated results in nanocomposite formation however, non-dispersed clay shows no formation of nanocomposites. Enhancement of mechanical properties leads to the formation of exfoliated nanocomposite as compared to those observed for intercalated systems. It has been suggested that layered materials may be beneficial for the enhancement of polymer properties. Once clay materials are dispersed uniformly in a polymer matrix, the properties can be largely enhanced [24, 25]. Graphite as a layered structured material demonstrates enhancement of properties. It consists of carbon layers in an alternate stacking sequence with covalently bonded carbon atoms in a hexagonal arrangement within the layers. The typical d-spacing between the carbon layers in graphite is approximately 0.335 nm [24, 25]. Graphite and graphite powder are valued in industrial applications due to its lubricating properties. Based on these observations, it would be assumed that there should be improvement of properties observed for the graphite-polymer composites. Micron sized particles are indispensable materials for industries due to their unique size dependent properties (such as optical, mechanical, and electrical) largely differ from their bulk materials. Such particles have a different tendency for adhesion and aggregation, thus it is necessary to control their aggregation/dispersion phenomena in order to use them in functional materials and final products. However, controlling the stability of suspension in organic media is still a challenging issue [26–31].

WEP is extensively used as thermal insulation, due to its moisture resistance, lifetime durability and flame retardancy. It is the largest commodity polymer with total demand more than 80 million tonnes per annum. Most of the used WEP materials are not recycled effectively and hence pose serious disposal issues. However, the impact of WEP on the environment has drawn a great interest. The present work focuses on the study of wettability property of WEP which is used as binder and graphite powder as additive for investigating the hydrophobic properties. Literature reports the use of fluoropolymers or organic/inorganic materials to achieve highly hydrophobic surfaces. We have proposed an alternative cost-effective versatile method for achieving hydrophobic surfaces without fluorination treatment.

2. Experimental

2.1. Materials

Graphite powder (250 μm, 99.99%), toluene (anhydrous, 99.8%), acetone (ACS reagent, ≥99.5%), and ethanol (ACS reagent, ≥99.5% (200 proof), absolute) were purchased from Sigma–Aldrich (India) and used as received. Glass slides (30 × 35 × 3 mm) were received from Fisher Scientific (India). WEP having excellent properties such as thermal insulation, water resistance, compressive strength, non-abrasive to delicate parts are procured from POLYFOAM Corporation (USA) and used as received.

2.2. Procedure for cleaning glass slides

Glass slides were ultrasonicated (Sonicator Model-EI-6LH-SP, Sl. No- 1209-122, India) at 20 kHz and 20 W in 20 mL ethanol for 15 min followed by ultrasonication with deionised water twice for next 5 min [32]. These cleaned glass slides were ready for use as substrates for hydrophobic coating.

2.3. Preparation of homogeneous WEP composites

In a typical process for fabrication of polystyrene blend, varying concentration of WEP (2–6 g) was mixed with 10 mL toluene. The viscosity of resulted solution was measured by Brookfield Viscometer. Appropriate amount of graphite powder (1–7 wt%) was dispersed in WEP solution followed by ultrasonication at 40 °C. The viscosity of 2 g WEP in 10 mL toluene was observed to be 900 mPa·s consistency. It is observed that viscosity of samples increases drastically with increase in concentration of WEP (3 to 6 g). Since solvent evaporation is high during the spin coating process, higher viscosity of the solution results in non-uniform layer on the substrate. For achieving uniform thin layer on the glass slide, it is necessary to control the viscosity of the

solution. It was observed that viscosity imparted by mixture of 2 g WEP in 10 mL toluene is suitable for formation of uniform thin layer on substrate.

2.4. Fabrication of hydrophobic coating

The optimized WEP/graphite solution was spin coated on a cleaned glass slide using spin coater, (Holmarc Model No. HO-TH-05, India). Briefly, two drops of solution were placed on a glass slide and spin coated at 2000 rpm for 90 sec. This step is repeated thrice for fabrication of a dense layer on the surface of the substrate. The thickness of spin coated samples was optimized to 20 micron and was maintained for comparative study of wettability property. Figure 1 illustrates schematically the fabrication process for formation of hydrophobic coating on the glass substrates.

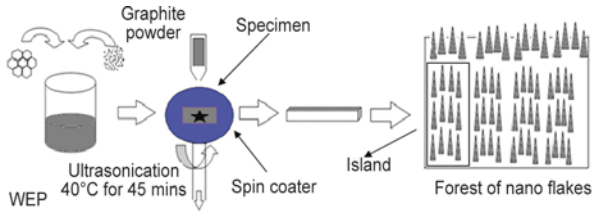

Figure 1. Schematic representation of the process for fabrication WEP film

2.5. Films characterization

The thickness of the coated layer was measured by 3D non contact surface profile (NewView™ 7100, Middlefield, USA). The morphology of the samples was observed using FE-SEM (JSM-6700F, JEOL, Japan). The roughness of the resulted coatings was evaluated using AFM (Asylum research, an Oxford Instrument company, UK) in tapping mode. The stability of the dispersed graphite powder in the polymer blend was monitored by the surface area analyzer (XiGo Nano Tools, Acorn Area, UK). This instrument was used for characterizing the stability of micro/nano sized particles present in the solution for fixed time duration. The stability of particles in the solution leads to homogeneous dispersion of particles i.e. particles do not aggregate or settle at the stipulated time period. The stability of the solvent (toluene), WEP/toluene, WEP/toluene/graphite was individually measured using the Acorn Area software version 0.82. These measurements were carried out in NMR tubes having outer diameter 5 mm. 0.5 mL samples were placed in different NMR tubes such that the tubes are filled till the minimum height of 54 mm ensuring that no air bubbles are trapped. The tubes were capped to prevent drying of samples. For accurate results, the tubes were filled to the same volume. Initially, the bulk relaxation time (T_1) of pure solvent (toluene) expressed in ms was quantified and saved as reference value for determining the relaxation time (T_2) for polymer composite (EPF/graphite 4 wt%, and WEP/graphite 5 wt%). Surface wettability property of the samples was measured by the sessile drop technique [33]. The water contact angle (WCA) measurements were carried out on a Krüss DSA100 (Germany) contact angle goniometer with deionised water at an ambient temperature. During water contact angle measurement, 4 μL of DI water was delivered from the syringe to form a sessile drop on the surface of the glass slide. An average of five measurements was used for the analysis.

3. Results and discussion

Surface modification of the particles is required to achieve enhanced stability of micron-sized particles in liquid media. This is done by introducing polymeric materials to generate an effective steric repulsive force from the polymer chains. This repulsive force increases the surface charge which controls the suspension rate of particles in the liquid medium. The nature of polymeric materials (hyrophilic/hydrophobic) also plays a major role for generation of steric repulsive force for effective dispersion and stability of particles. For dispersion of hydrophobic powders such as SiC, CNT, Coal, etc., polymers with hydrophilic group or hydrophobic groups are often used as a surfactant. For hydrophobic surface modification of particles is a well-known technique for obtaining good dispersion and stability. The hydrophobic segments aids in adsorption of dispersant on to hydrophobic particles. Aromatic compounds such as styrene is used to make an effective adsorption of hydrophobic particles by means of hydrophobic and pi-pi interactions [34–37]. PEI (polyethyleneimine) is also used as hydrophobic segments, which is known to improve the stability of SiC and CNT in aqueous media by PEI [38]. Uhl and Wilkie [24] and Min *et al.* [25] have reported that parallel hexagonal networks of carbon atoms in graphite sheet are held together at certain spacing by weak van der Waals forces. During sonication process, (20 kHz and 20 W) the individual layer of hexagonal network of carbon atoms in graphite particles are detached eas-

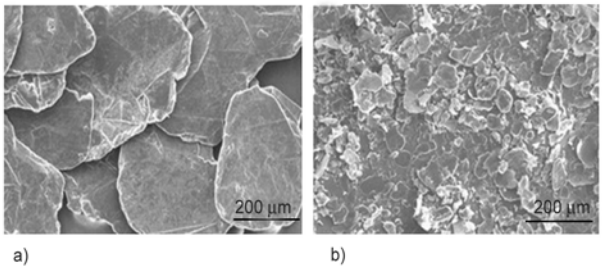

Figure 2. (a) SEM of graphite as supplied, (b) SEM of ultrasonicated graphite

ily due to weak van der Waals forces which leads to reduction in particle size from 250 to less than 50 µm which was confirmed in FESEM micrographs (Figure 2a–2b). Hence, sonication was contunued for 45 min. However, in the present WEP/graphite composite no charge effect was observed. Toluene is a nonpolar solvent, there is no steric effect and charge formation. Aggregation of small sized graphite particles (<50 µm) occurs in the solution, which has strong impact on the morphology of the films. These flakes are deposited during spin coating process and forms islands of flakes. During sonication homogeneous dispersion occurs, which has stability up to 30 min. Aggregation occurs during spin coating which results in formation of islands of flakes. These islands enhance the surface roughness which increases the hydrophobicity surface. The quality of dispersion of particles in the NMR tubes affects the suspension of graphite particles in the composite. 4 and 5 wt% graphite in WEP blend showed good dispersion of particles for 30 min. However, suspension of graphite particles from WEP/4 wt% graphite was found to be better as compared to suspension of graphite particles in WEP/5 wt% graphite. This is due to settling of graphite from WEP/5 wt% graphite, which leads to variation in the relaxation time as shown in Figure 3.

Uniform relaxation time was observed for WEP/4 wt% graphite confirming no aggregation or settling of particles. Thus the relaxation time required for settling of particles was measured through surface area analyzer and used to study the stability of particles in solution. These experimental results facilitate correlation of surface morphology of polymer film with wettability property.

Polymer films with uniform thickness of 20 µm thin film were fabricated using spin coater were fabricated using varied concentration of additives. The effect of concentration of additives on the water contact angle as shown in Figure 4 presents stepwise loss of hydrophilic property with increase in weight percentage of graphite powder. With 1 wt% graphite in the blend, WCA enhances from 89 to 98°. Further increase in graphite concentration to 2 wt%, WCA shows marginally increase in WCA from 98 to 101°. With 3 and 5 wt%, WCA was obtained to be 104 and 119° respectively which shows better hydrophobicity. Decrease in WCA was observed with further increase in graphite content. WCA in however increased from 119 to 129° with an increase in thickness of the film from 20 to 30 µm on the glass slide. This increase in hydrophobicity of film correlates the surface morphology of the developed film with different concentration of graphite loading.

The wetting behaviour of the surface depends upon the surface chemistry and surface topology. The surface topology follows the Wenzel and Cassie-Baxter water contact model, in which surface roughness increases the apparent water contact angle. For hydrophilic surfaces, the interaction between the substrate surface and water is favoured but for hydrophobic surfaces, this interaction is prevented due to the presence of surface roughness resulting in spontaneous increase in water contact angle. Systemati-

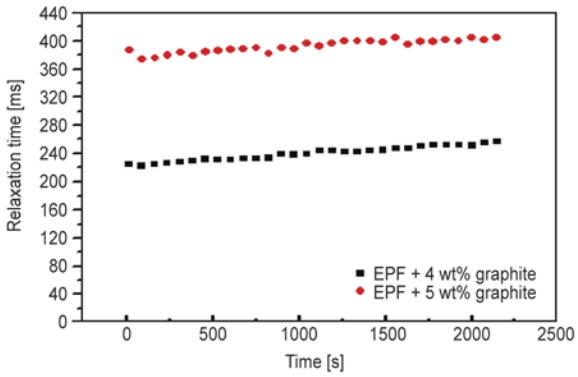

Figure 3. Stability test of graphite powders of 4 wt% and 5 wt% in the polymer solution

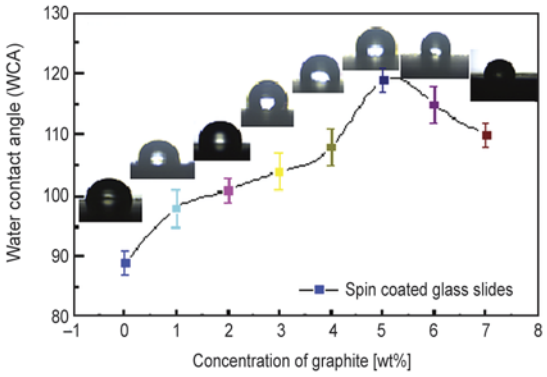

Figure 4. Effect of the different concentration of graphite on water contact angle

cally study the surface morphology of blend films were studied by formation of layer by layer of stable surface of graphite with WEP was generated on the surface of etched glass by spin coating technique. Surface roughness is a measure of the texture of the surface. It is quantified by the vertical deviation of the real surface from its ideal surface. The double layer structure improves the surface roughness as compared to single layer structure. When second layer structure is introduced over the single layer structure, the deposition of graphite particles takes place over the top first layer, which enhances roughness factor. This phenomenon is based on Wenzel Equation (1) [18]:

$$\cos(\theta^{w}) = r\cos\theta \quad (1)$$

where θ is the maximum WCA observed, r is the theoretical roughness calculated and θ^{w} is Wenzel water contact angle. The arithmetic mean height of surface along Z axis, of double layer structure is more than the single layer structure and hence hydrophobicity increases. The aggregation of graphite flakes occurs over each layer and arithmetic mean height of surface along Z axis is enhanced. The mean height affects the roughness (r) of the surface and hence hydrophobicity is enhanced. Table 1 presents gradual increase in WCA with increase in r values indicating WCA is related to air fraction on the surface.

FESEM studies of the polymer films revealed the evolution of different morphological images as shown in Figure 5. By spin coating, the solution of intrinsically hydrophobic polystyrene smooth film is formed on the surface of glass substrate. Previous studies regarding multiscale structures especially micro-nano scale structures, which are advantageous for obtaining hydrophobicity have been discussed using Wenzel and Cassie–Baxter models. Figure 5a, reveals the presence of large number of micro-sized particles on the surface. Aggregation of the particles was observed with 1 wt% graphite in the blend. Aggregation of the microsize particles and increase in the number of flakes was observed with 2 wt% graphite [39, 40]. The magnified image (Figure 5b) reveals more aggregation of graphite particles and enhanced non-wettability property. Similarly, the multiscale slippery surface is revealed with an increase in concentration of graphite from 2 to 3 wt% as shown in Figure 5c. Islands of flakes forest was observed (Figure 5d) with 4 wt% graphite which covers maximum are of the film and is the result of aggregation of graphite [41, 42]. With graphite content of 5 wt%, the entire surface was observed to be covered with large number of island-like surface structures. These islands are composed of forest of flakes, and these flakes originates from the balance of spin rate and time duration, which results in the enhancement of hydrophobicity as shown in Figure 5e. This island enhances the roughness of the substrate. The water contact angle is increased due to roughness factor (r) and hence water repellent property improved. Since large numbers of air pockets are trapped between these flakes, they result in enhancement of surface roughness on an island. FESEM image (Figure 5e) of spin coated specimen shows the presence of large number of islands indicating increased surface roughness. Thus, the micro scale structure with formation of forest of flakes, during the spin coating process provides more roughness for obtaining hydrophobicity [40]. Marginal decrease in WCA was observed with 7 wt% graphite polymer blend. Similalr behaviour was reported by Manoudis *et al*. and Ramaratnam *et al*. [43, 44]. Separation between the flakes in a single island decreased with the introduction of more flakes. It results in less trapping of air pockets and surface roughness will gradually loosen. However enhancement in WCA observed with 5 wt% graphite with introduction of the fourth layer on the glass surface as shown in Figure 6a reveals the formation of more islands and drastic enhancement of in roughness value.

To examine the influence of surface topology on wettability property, AFM analysis was adopted as shown in Figure 7. The images reveal that the islands are composed of a large number of flake

Table 1. Water contact angle and roughness of the surface of different polymer blends

Concentration of graphite [wt%]	Average roughness, Sa [nm]	Average height of peak [nm]	Water contact angle [°]
0	20.009	14	89
1	80.141	30	98
2	86.418	40	101
3	88.064	65	104
4	93.567	79	108
5	109.078	110	119
6	104.560	102	115
7	95.120	80	110

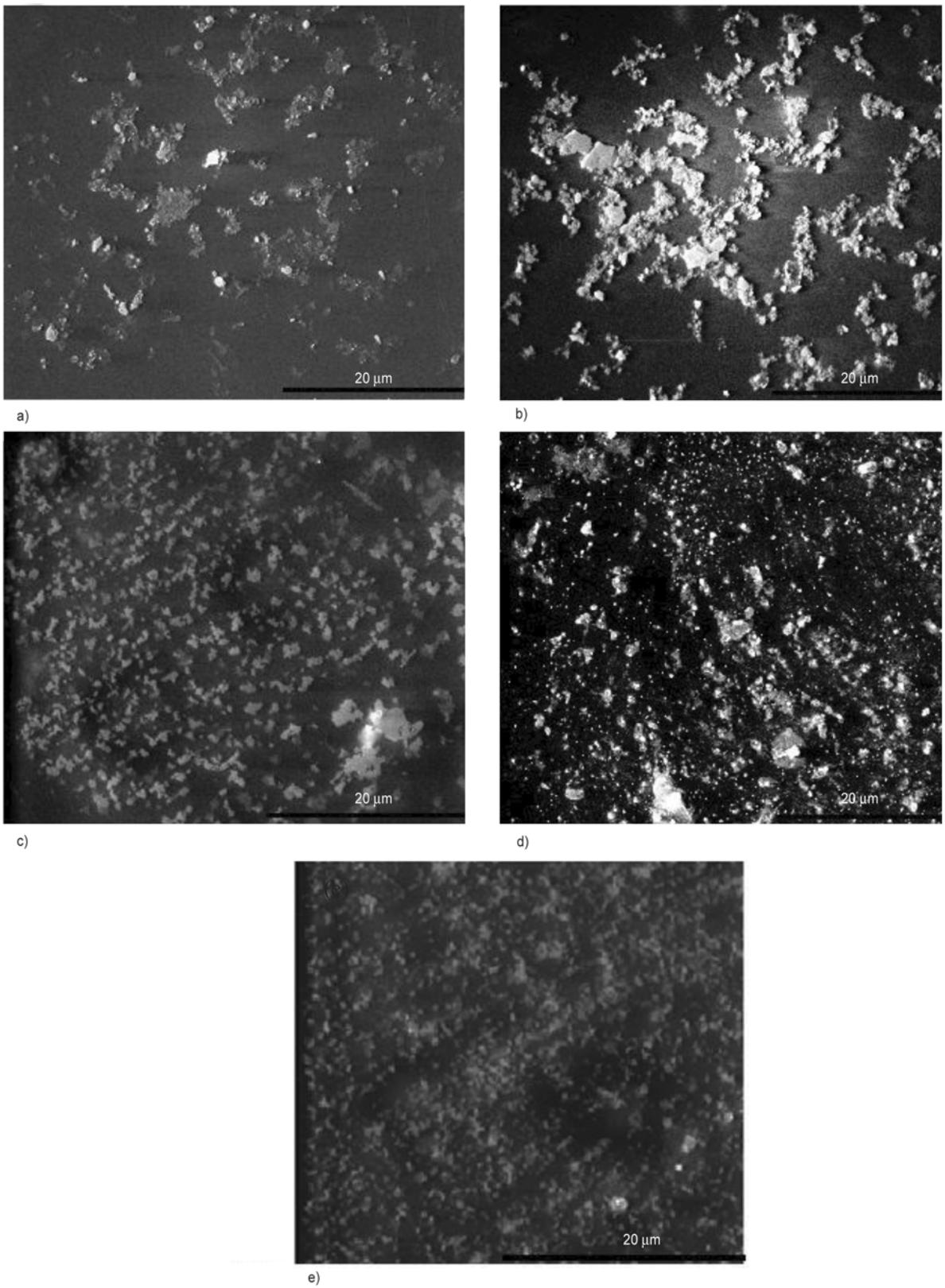

Figure 5. FE-SEM images of the WEP blend with different concentration of graphite powder (a) 1 wt%; (b) 2 wt%; (c) 3 wt%; and (d) 4 wt%; (e) 5 wt%

formed on the surface with hierarchal structures. Surface roughness was evaluated by the vertical deviation of a real surface from its original form. The average roughness of polymer film, Sa = 80.141 was quantified for WEP/1 wt% graphite film. Introduction of more number of islands with increase in graphite content to 2 wt% increased the average roughness to 86.418. Further increase in

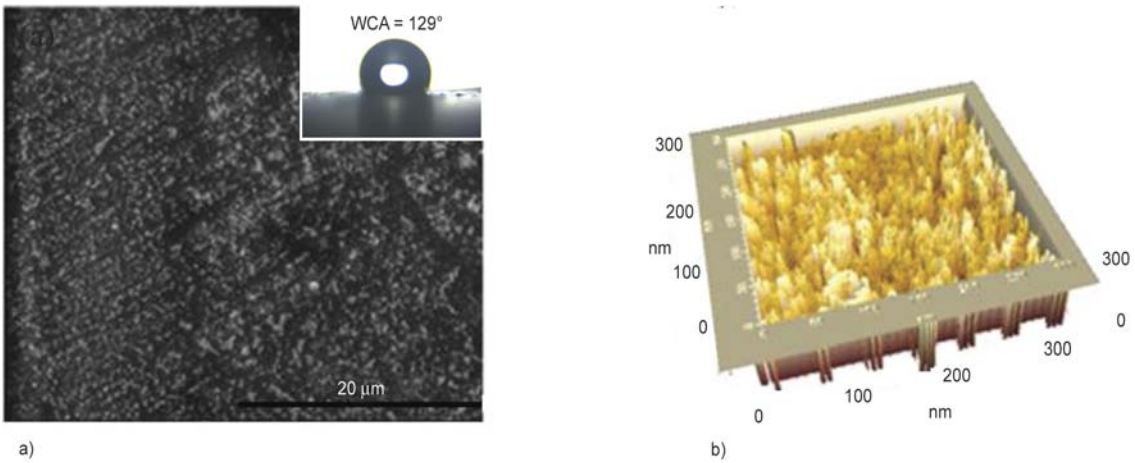

Figure 6. (a) FE-SEM images of the WEP blend (four layers) with 5 wt% of graphite powder, (b) AFM image WEP film with 5 wt% graphite powder for four layers

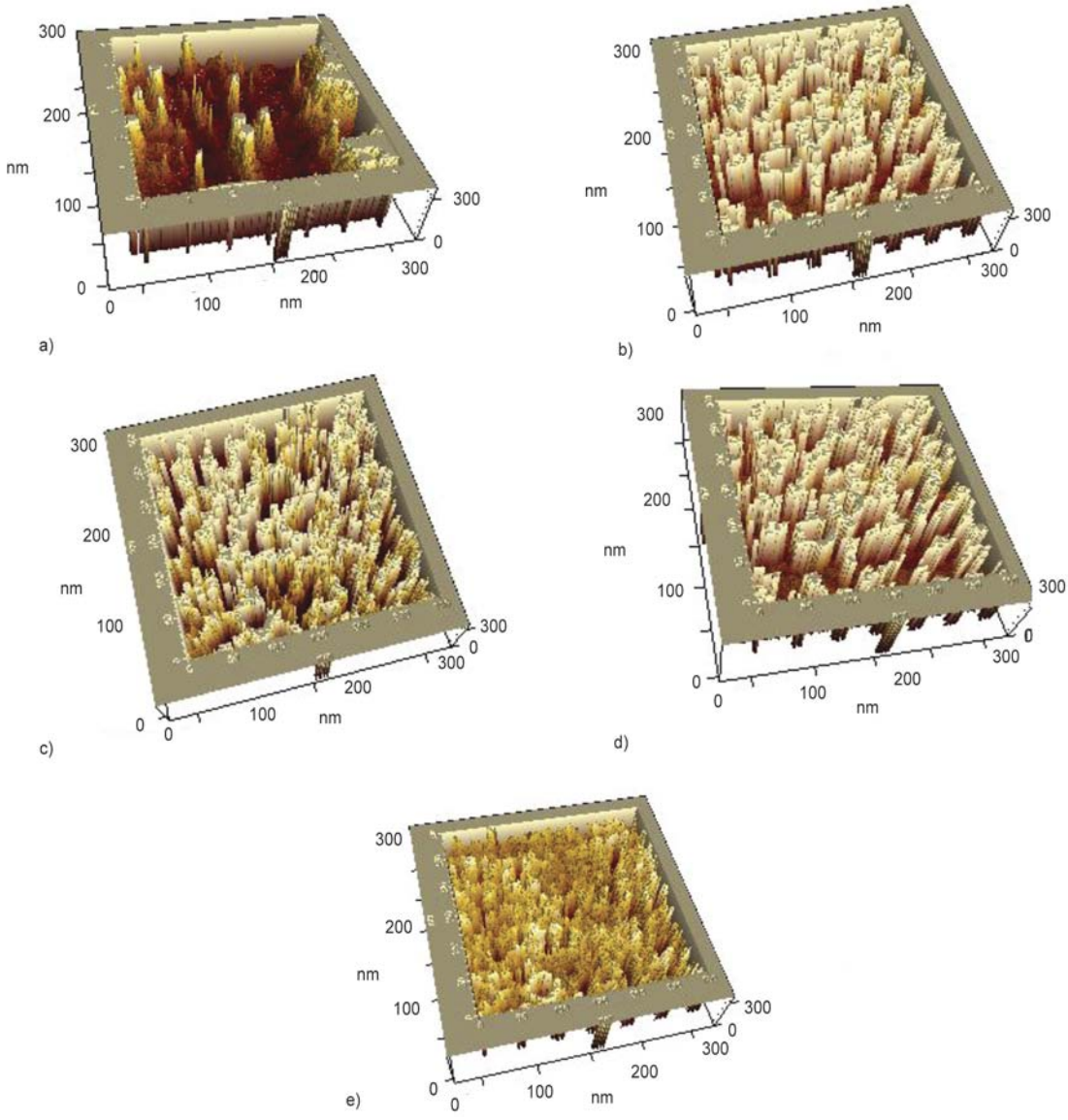

Figure 7. Tapping mode of AFM topology and 2D images of WEP film with content of graphite powder of (a) 1 wt %; (b) 2 wt%; (c) 3 wt%; (d) 4 wt%; (e) 5 wt%

graphite content to 3 wt%, shows increase in number of nano flakes formation which combines to form the forest as shown in Figure 7c. Our observation correlates well the roughness of the film with the water contact angle. Similarly, the relation between surface roughness and water contact angle for other samples was revealed [45]. The surface roughness and water contact angle data collected from all the samples are shown in Table 1. Maximum surface roughness of 109.078 was quantified for graphite concentration of 5 wt%. This increase in roughness was attributed to the formation of a large number of islands. We also noticed that maximum height of a single flake (160 nm) and separation between two flakes (0.2 nm) on the surface enables the anisotropic slippery surface. A single island consists of a forest of nano flakes formed on the surface, which covers maximum area with increasing graphite content. This trend translated into the increased hydrophobicity was indicated by WCAs (Figure 4). With increased graphite concentration the distance between the nano flakes decreased gradually. The average height of nano flakes also decreases simultaneously and hence roughness loosened widely. But with increasing thickness of the polymer film layer, surface roughness improves, which was clearly observed from in Figure 6b [46]. In Wenzel model, water droplet floats on the projection surface. The average height of the peaks is experimentally calculated as 110 nm for graphite concentration of 5 wt% from AFM images. With the introduction of more concentration of graphite powders, more nano flakes are formed on the surface, which reduces the average height of the peak. It was observed that with 7 wt% graphite, the average height of peak reduces to 80 nm. Similar observations are also revealed with the deposition of four layers on the surface. This observation supports the idea that surface topology plays an important role determining the wettability behaviour of the surface than surface composition.

4. Conclusions

In this study, we have described a facile and cost effective technique for fabrication of hydrophobic surface with good water repellent property using WEP, which can be self assembled into a forest of nano flakes by the spin coating process. These forests of nano flakes are combined to form small islands on the surface. The network of nano flakes of the spin coated sample was effectively controlled by the concentration of graphite, and the wettability property was analyzed by measurement of water contact angle. The stability of dispersed graphite powders with WEP materials clearly shows excellent suspension behaviour in the liquid medium. The induced roughnesses in the samples seem to be correlated to the surface morphology. The proposed water contact angle values were reflected from the surface topology. WCA was enhanced up to 129° due to modification of surface film by increase in thickness of film. This method could provide an alternative approach for fabricating superhydrophobic materials with hierarchical structures. We hope that this approach could provide to prepare the superhydrophobic surface with low adhesion.

Acknowledgements

Authors greatly appreciate the financial support from the Defence Institute of Advanced Technology, Pune. The authors would like to thank the Vice Chancellor Dr Prahlada, DIAT, Naval Head Quarters and 'DIAT—NANO project EPIPR/ER/1003883/M/01/908/2012/D (R&D)/ 1416' for encouragement and support. We are grateful to Dr. P. G. Ghosal, DMRL and Dr S. Datar for characterisation support.

References

[1] Barthlott W., Neinhuis C.: Purity of the sacred lotus, or escape from contamination in biological surfaces. Planta, **202**, 1–8 (1997). DOI: 10.1007/s004250050096

[2] Gao X., Jiang L.: Water-repellent legs of water striders. Nature, **232**, 36–38 (2004). DOI: 10.1038/432036a

[3] Zhai L., Berg M. C., Cebeci F. Ç., Kim Y., Milwid J. M., Rubner M. F., Cohen R. E.: Patterned superhydrophobic surfaces: Toward a synthetic mimic of the Namib desert beetle. Nano Letter, **6**, 1213–1217 (2006). DOI: 10.1021/nl060644q

[4] Goswami D., Medda S. K., De G.: Superhydrophobic films on glass surface derived from trimethylsilanized silica gel nanoparticles. ACS Applied Materials Interfaces, **3**, 3440–3447 (2011). DOI: 10.1021/am200666m

[5] Bravo-Gutiérrez M. E., Castro M., Hernández-Machado A., Poiré C. E.: Controlling viscoelastic flow in microchannels with slip. Langmuir, **27**, 2075–2079 (2011). DOI: 10.1021/la103520a

[6] Blossey R.: Self-cleaning surfaces – Virtual realities. Nature Materials, **2**, 301–306 (2003). DOI: 10.1038/NMAT856

[7] Choi C. H., Kim C. J.: Large slip of aqueous liquid flow over a nanoengineered superhydrophobic surface. Physical Review Letters, **96**, 066001/1–066001/4 (2006).
DOI: 10.1103/PhysRevLett.96.066001

[8] Choi C-H., Ulmanella U., Kim J., Ho C-M., Kim C-J.: Effective slip and friction reduction in nanograted superhydrophobic microchannels. Physics of Fluids, **18**, 087105/1–087105/8 (2006).
DOI: 10.1063/1.2337669

[9] Zhang F., Zhao L., Chen H., Xu S., Evans D. G., Duan X.: Corrosion resistance of superhydrophobic layered double hydroxide films on aluminum. Angewandte Chemie International Edition, **47**, 2466–2469 (2008).
DOI: 10.1002/anie.200704694

[10] Cao L., Jones A. K., Sikka V. K., Wu J., Gao D.: Anti-icing superhydrophobic coatings. Langmuir, **25**, 12444–12448 (2009).
DOI: 10.1021/la902882b

[11] Lee H. J.: Design and development of anti-icing textile surfaces. Journal of Materials Science, **47**, 5114–5120 (2012)
DOI: 10.1007/s10853-012-6386-2

[12] Sarkar D. K., Farzaneh M.: Superhydrophobic coatings with reduced ice adhesion. Journal Adhesion Science and Technology, **23**, 1215–1237 (2009).
DOI: 10.1163/156856109X433964

[13] Saleema N., Farzaneh M., Paynter R. W., Sarkar D. K.: Prevention of ice accretion on aluminum surfaces by enhancing their hydrophobic properties. Journal of Adhesion Science and Technology, **25**, 27–40 (2011).
DOI: 10.1163/016942410X508064

[14] Saleema N., Farzaneh M.: Thermal effect on superhydrophobic performance of stearic acid modified ZnO nanotowers. Applied Surface Science, **254**, 2690–2695 (2008).
DOI: 10.1016/j.apsusc.2007.10.004

[15] Sarkar D. K., Farzaneh M., Paynter R. W.: Superhydrophobic properties of ultrathin rf-sputtered Teflon films coated etched aluminum surfaces. Materials Letters, **62**, 1226–1229 (2008).
DOI: 10.1016/j.matlet.2007.08.051

[16] Sarkar D. K., Farzaneh M., Paynter R.: Wetting and superhydrophobic properties of PECVD grown hydrocarbon and fluorinated-hydrocarbon coatings. Applied Surface Science, **256**, 3698–3701 (2010).
DOI: 10.1016/j.apsusc.2009.12.049

[17] Safaee A., Sarkar D. K., Farzaneh M.: Superhydrophobic properties of silver-coated films on copper surface by galvanic exchange reaction. Applied Surface Science, **254**, 2493–2498 (2008)
DOI: 10.1016/j.apsusc.2007.09.073

[18] Wenzel R. N.: Resistance of solid surfaces to wetting by water. Industrial and Engineering Chemistry, **28**, 988–994 (1936).
DOI: 10.1021/ie50320a024

[19] Cassie A. B. D., Baxter S.: Wettability of porous surfaces. Transactions of the Faraday Society, **40**, 546–551 (1944).
DOI: 10.1039/TF9444000546

[20] Shang H. M., Wang Y., Takahashi K., Cao G. Z., Li D., Xia Y. N.: Nanostructured superhydrophobic surfaces. Journal of Material Science, **40**, 3587–3591 (2005)
DOI: 10.1007/s10853-005-2892-9

[21] Shang Q., Gao L., Liu H., Xiao G.: Fabrication of superhydrophobic silica film by removing polystyrene spheres. Journal of Sol-Gel Science Technology, **59**, 334–337 (2011).
DOI: 10.1007/s10971-011-2507-7

[22] Song J., Xu W., Lu Y.: One-step electrochemical machining of superhydrophobic surfaces on aluminum substrates. Journal of Materials Science, **47**, 162–168 (2012).
DOI: 10.1007/s10853-011-5783-2

[23] Xu W., Song J., Sun J., Dou Q., Fan X.: Fabrication of superhydrophobic surfaces on aluminum substrates using $NaNO_3$ electrolytes. Journal of Materials Science, **46**, 5925–5930 (2011).
DOI: 10.1007/s10853-011-5546-0

[24] Uhl F. M., Wilkie C. A: Polystyrene/graphite nanocomposites: Effect on thermal stability. Polymer Degradation and Stability, **76**, 111–122 (2002).
DOI: 10.1016/S0141-3910(02)00003-4

[25] Min X., Sun L., Liu J., Li Y., Gong K.: Synthesis and properties of polystyrene/graphite nanocomposites. Polymer, **43**, 2245–2248 (2002).
DOI: 10.1016/S0032-3861(02)00022-8

[26] Iijima M., Kamiya H.: Surface modification for improving the stability of nanoparticles in liquid media. KONA Powder and Particle Journal, **27**, 119–129 (2009).

[27] Marignier J. L., Belloni J., Delcourt M. O., Chevalier J. P.: Microaggregates of non-noble metals and bimetallic alloys prepared by radiation-induced reduction. Nature, **317**, 344–345 (1985).
DOI: 10.1038/317344a0

[28] Alivisatos P.: Semiconductor clusters, nanocrystals, and quantum dots. Science, **271**, 933–937 (1996).
DOI: 10.1126/science.271.5251.933

[29] Ozin G. A.: Nanochemistry: Synthesis in diminishing dimensions. Advanced Materials, **4**, 612–649 (1992).
DOI: 10.1002/adma.19920041003

[30] Jun Y-W., Huh Y-M., Choi J-S., Lee J-H., Song H-T., Kim S., Yoon S., Kim K-S., Shin J-S., Suh J-S., Cheon J.: Nanoscale size effect of magnetic nanocrystals and their utilization for cancer diagnosis via magnetic resonance imaging. Journal of American Chemical Society, **127**, 5732–5733 (2005).
DOI: 10.1021/ja0422155

[31] Dick K., Dhanasekaran T., Zhang Z., Meisel D.: Size-dependent melting of silica-encapsulated gold nanoparticles. Journal of American Chemical Society, **124**, 2312–2317 (2002).
DOI: 10.1021/ja017281a

[32] Yin L., Wang Y., Ding J., Wang Q., Chen Q.: Water condensation on superhydrophobic aluminum surfaces with different low-surface-energy coatings. Applied Surface Science, **258**, 4063–4068 (2012).
DOI: 10.1016/j.apsusc.2011.12.100

[33] Chen P., Hu Y., Wei C.: Preparation of superhydrophilic mesoporous SiO_2 thin films. Applied Surface Science, **258**, 4334–4338 (2012).
DOI: 10.1016/j.apsusc.2011.12.109

[34] Spyriouni T., Economou I. G., Theodorou D. N.: Molecular simulation of α-olefins using a new united-atom potential model: Vapor–liquid equilibria of pure compounds and mixtures. Journal of American Ceramic Society, **121**, 3407–3413 (1999).
DOI: 10.1021/ja982453y

[35] Xue C-H., Shi M-M., Yan Q-X., Shao Z., Gao Y., Wu G., Zhang X-B., Yang Y., Chen H-Z., Wang M.: Preparation of water-soluble multi-walled carbon nanotubes by polymer dispersant assisted exfoliation. Nanotechnology, **19**, 115605–115612 (2008).
DOI: 10.1088/0957-4484/19/11/115605

[36] Kakui T., Kamiya H.: Effect of sodium aromatic sulfonate group in anionic polymer dispersant on the viscosity of coal–water mixtures. Energy and Fuels, **18**, 652–658 (2004).
DOI: 10.1021/ef030154a

[37] Delozier D. M., Watson K. A., Smith J. G., Clancy T. C., Connell J. W.: Investigation of aromatic/aliphatic polyimides as dispersants for single wall carbon nanotubes. Macromolecules, **39**, 1731–1739 (2006).
DOI: 10.1021/ma051826u

[38] Zhang T., Zhang Z., Dong M., Zhang J., Lin Q., Jiang D.: The influence of polyethylene imine on the gel-casting of sic with two different initiators. Journal of American Ceramic Society, **90**, 3748–3756 (2007).
DOI: 10.1111/j.1551-2916.2007.01992.x

[39] Karmouch R., Guy G. R.: Superhydrophobic wind turbine blade surfaces obtained by a simple deposition of silica nanoparticles embedded in epoxy. Applied Surface Science, **257**, 665–669 (2010).
DOI: 10.1016/j.apsusc.2010.07.041

[40] He Z., Ma M., Xu X., Wang J., Chen F., Deng H., Wang K., Zhang Q., Fu Q.: Fabrication of superhydrophobic coating via a facile and versatile method based on nanoparticle aggregates. Applied Surface Science, **258**, 2544–2550 (2012).
DOI: 10.1016/j.apsusc.2011.10.090

[41] Xu M., Lu N., Qi D., Xu H., Wang Y., Shi S., Chi L.: Fabrication of superhydrophobic polymer films with hierarchical silver microbowl array structures. Journal of Colloid and Interface Science, **360**, 300–304 (2011).
DOI: 10.1016/j.jcis.2011.04.048

[42] Wang J., Chen X., Kang Y., Yang G., Yu L., Zhang P.: Preparation of superhydrophobic poly(methyl methacrylate)-silicon dioxide nanocomposite films. Applied Surface Science, **257**, 1473–1477 (2010).
DOI: 10.1016/j.apsusc.2010.08.075

[43] Manoudis P., Papadopoulou S., Karapanagiotis I., Tsakalof A., Zuburtikudis I., Panayiotou C.: Polymer-silica nanoparticles composite films as protective coatings for stone-based monuments. Journal of Physics: Conference Series, **61**, 1361–1365 (2007).
DOI: 10.1088/1742-6596/61/1/269

[44] Ramaratnam K., Iyer S. K., Kinnan M. K., Chumanov G., Brown P. J., Luzinov I.: Ultrahydrophobic textiles using nanoparticles: Lotus approach. Journal of Engineered Fibers, **3**, 1–14 (2008).

[45] Athauda T. J., Decker D. S., Ozer R. R.: Effect of surface metrology on the wettability of SiO_2 nanoparticle coating. Materials Letters, **67**, 338–341 (2012).
DOI: 10.1016/j.matlet.2011.09.100

[46] Meng L-Y., Park S-J.: Effect of fluorination of carbon nanotubes on superhydrophobic properties of fluoro-based films. Journal of Colloid and Interface Science, **342**, 559–563 (2010).
DOI: 10.1016/j.jcis.2009.10.022

eXPRESS Polymer Letters Vol.7, No.11 (2013) 910–924
Available online at www.expresspolymlett.com
DOI: 10.3144/expresspolymlett.2013.89

Effects of different epoxidation methods of soybean oil on the characteristics of acrylated epoxidized soybean oil-co-poly(methyl methacrylate) copolymer

P. Saithai[1,2], *J. Lecomte*[2], *E. Dubreucq*[2], *V. Tanrattanakul*[1*]

[1]Bioplastic Research Unit, Department of Materials Science and Technology, Faculty of Science, Prince of Songkla University, 90112 Songkla, Thailand
[2]Montpellier SupAgro, UMR 1208 IATE, 2 Place Viala, 34060 Montpellier Cedex, France

Received 13 May 2013; accepted in revised form 24 July 2013

Abstract. The effect of the type of epoxidation processes of soybean oil on the characteristics of epoxidized soybean oils (ESOs), acrylated epoxidized soybean oils (AESOs), and acrylated epoxidized soybean oil – poly(methyl metacrylate) copolymers (AESO-co-PMMA) has been investigated. Two epoxidation processes were used: an *in situ* chemical epoxidation using hydrogen peroxide and formic acid, and a chemo-enzymatic epoxidation using 2 enzymes: Novozyme® 435 (CALB) and a homemade lipase/acyltransferase (CpLIP2). ESOs containing different numbers of epoxide groups/molecule were synthesized. A commercial ESO (Vikoflex® 7170) was employed and it had the highest number of epoxide groups. Acrylation of ESOs was carried out using acrylic acid, and copolymerized with a methyl methacrylate monomer. The chemo-enzymatic epoxidation produced high acid value, particularly from the CpLIP2 (~ 46–48%) and indicated the formation of epoxidized free fatty acids. In contrast, the ESO synthesized from the chemical epoxidation showed a very low acid value, < 0.6%. The AESOs synthesized from the CALB-based ESO and the chemical-based ESO showed a similar number of acrylate groups/molecule while that from the CpLIP2-based ESO showed a very low number of acrylate groups because the carboxylic groups from the epoxidized free fatty acids impeded the acrylation reaction. The lower the number of acrylate groups the lower was the crosslink density, the T_g, and the gel content in the AESO-co-PMMA copolymer.

Keywords: *polymer synthesis, tailor-made polymers, biocomposites, thermosetting resins, thermal properties*

1. Introduction

In the last two decades bio-based polymers have received increasing attention from the industrial sector and researchers. These polymers or their monomers are derived from renewable resources. They could be a thermoplastic or a thermosetting plastic and they could be biodegradable or non-biodegradable. Plant oil is one of the interesting renewable monomers, particularly soybean oil as it is abundant and cheap. Typically, a triglyceride is the major component in all plant oils and these contain both saturated and unsaturated fatty acids. Their reactivity depends on the numbers of double bonds (C=C) or the type of fatty acid. Soybean oil has relatively high double bond content but these double bonds are not highly active for typical free radical polymerization. Therefore, the double bonds in the soybean oil have to be converted to more reactive functional groups such as epoxide groups, acrylate groups, hydroxyl groups, and even some bromoacrylated triglycerides, that can be used in the free radical polymerization [1–12]. Epoxidized soybean oil (ESO) has been produced for the last 30 years and is available under various trade names. ESO has

*Corresponding author, e-mail: varaporn.t@psu.ac.th

been polymerized to form plastic materials such as ESO-co-styrene/divinylbenzene resins [13–18], ESO thermosetting allyl resins [19], a sheet molding compound resin [20], and a hydrogel [21], or even polymer composites such as an organo clay nanocomposite [22], and fiber-reinforced composites [23–25]. According to Hazer and coworkers [26–33], vegetable oils were autooxidized by exposure to sunlight or daylight in air for a given time to produce epoxides, peroxides, peroxides, and hydroperoxides in the molecular chains and were also graft copolymerized by free radical polymerization with other materials such as methyl methacrylate and styrene. Recently, the vegetable oil-based polymers have been prepared by cationic, olefin metathesis and condensation polymerization reactions, including the use of 'click' chemistry and carbon dioxide [5, 34–37]. Acrylation of epoxidized vegetable oils is one of the interesting techniques for preparing the vegetable oil-based polymers. The mechanical and thermal properties of acrylated epoxidized soybean oil (AESO) have been reported [3, 5, 8, 20, 23, 38, 39]. It has been established that AESO shows higher mechanical properties than ESO [22, 39]. AESO has been used for copolymerization with other materials such as a vinyl ester resin containing styrene [8–10] and with poly(methyl methacrylate) [38–40]. It was found that the mechanical properties of an AESO-co-PMMA copolymer were higher than those of AESO. Furthermore, the AESO-co-PMMA copolymer is an interesting polymer owing to the high weathering resistance of PMMA.

Although ESO- and AESO-based polymers seem to be environmentally friendly materials, the epoxidation process should be improved by using more green chemistry. This is because on an industrial scale, ESO is produced by an *in situ* epoxidation in the presence of a strong acid as a catalyst such as H_2SO_4 and H_3PO_4. The drawbacks of this method are the corrosion of equipment due to the acidic solution and the product must be neutralized and purified. Moreover, these acids can initiate oxirane ring-opening reactions with water, and lead to the formation of hydroxyl group on the fatty acid backbone and other by-products [41]. To eliminate these problems, enzymes have also been used in the epoxidation process [41]. The enzymes involved in the chemo-enzymatic epoxidation were a peroxygenase and a lipase. Blee and Schuber [42, 43] used the peroxygenase enzyme for epoxidation of mono- and polyunsaturated fatty acids. Piazza and coworkers [44–46] developed a method for the rapid isolation and immobilization of peroxygenases on membranes, and conducted epoxidation reactions in organic solvents. Lipase B from *candida antartica* (CALB) is one of the enzymes used most frequently as a biocatalyst. Lipase enzymes have been shown to produce peroxy acids from hydrogen peroxide and fatty acids by a perhydrolysis reaction. Most of the developments of the lipase-catalyzed chemo-enzymatic epoxidation in plant oils or fatty acids have been studied using a commercial enzyme lipase (Novozyme® 435) [41, 47–54]. By using enzymes, the addition of free acids was not required in order to obtain a high conversion, i.e. > 80%, and the neutral pH of the reaction mixture was maintained [52]. While ESO has been synthesized by the chemo-enzymatic epoxidation, to the best of our knowledge the conversion of this ESO into AESO has not been reported.

The objectives of the present study were to investigate the effect of the different epoxidation methods on ESO and the effect of the degree of epoxidation (or number of epoxide groups/molecule) in ESO on the characteristics of the ESO, AESO and AESO-co-PMMA copolymer. ESO was synthesized by chemical and chemo-enzymatic epoxidation methods. Peroxy acid produced from formic acid and hydrogen peroxide was used in the chemical epoxidation process. Hydrogen peroxide and lipase were used in the chemo-enzymatic epoxidation. Novozyme® 435 and a lipase from *Candida parapsilosis* (CpLIP2) were also employed. CpLIP2 has been shown to catalyze the alcoholysis of various esters in the presence of a large molar excess of water in a biphasic aqueous/lipid reactant medium with hydrolysis of the esters and was also found to be effective for the production of fatty hydroxamic acids in an aqueous medium by an aminolysis of fatty acids [55]. There has been no previous report of the chemo-enzymatic epoxidation of ESO catalyzed by CpLIP2.

2. Experimental

2.1. Materials

Commercialized cooking-grade soybean oil was employed. Commercialized epoxidized soybean oil (Vikoflex® 7170) was produced by Arkema Inc. (Philadelphia, PA, USA). Novozyme® 435, lipase B from *Candida antarctica* (CALB) immobilized on

macroporous polyacrylate resin beads, was from Sigma-Aldrich Corp. (St. Louis, MO, USA). It has a bead size of 0.3–0.9 mm and its activity is approximately 7,000 PLU/g. An enzyme lipase/acyltransferase CpLIP2 (*Candida parapsilosis*) was produced in our laboratory. Anhydrous sodium sulfate, sulfuric acid, acrylic acid, methyl methacrylate (MMA) and benzoyl peroxide were from Sigma-Aldrich (St. Louis, MO, USA). Hydrogen peroxide, hydroquinone and glacial formic acid were from Merck (Darmstadt, Germany). All chemicals were used as received.

2.2. Synthesis of epoxidized soybean oil (ESO)

2.2.1. Chemical epoxidation catalyzed by sulfuric acid

A solution of soybean oil (100 g) and glacial formic acid (13.97 g) was heated at a 45–55°C. Sulfuric acid (0.5 mL) was added into the solution. Then, 116.98 g of 30 wt% H_2O_2 solution was added slowly from a dropping funnel and reacted at 45, 50 and 55°C for 1–7 h. The molar ratio of soybean oil: formic acid: hydrogen peroxide was 1:2.64:8.9. The crude product was filtered and washed with distilled water repeatedly until a pH of 7.0 was obtained. The oil phase was dried with anhydrous sodium sulfate then filtered. Finally, the residue (water) was removed using an evaporator at 45–50°C under pressure. The number of epoxide groups per molecule of ESO was calculated from the ^{1}H-NMR spectrum by using the peak at δ = 4.0–4.4 ppm for the glycerol backbone and the peak at 0.9 ppm for the methyl group as an internal standard, and using the peak intensity ratio between the peak at 2.8–3.2 and 4.0–4.4 ppm [56]. This number was used to represent the sample code of the ESO. The degree of epoxidation (*DOE*) or percentage of conversion from double bonds to epoxide groups was determined from Equation (1) and the number of starting double bonds of the soybean oil used in the present study was 4.60:

$$DOE = \frac{number\ of\ epoxide\ groups}{number\ of\ starting\ double\ bonds} \cdot 100 \quad (1)$$

We assumed that *DOE* (Degree of epoxidation) of Vikoflex® 7170 should be very high, i.e. ~100%. However, there was no data on the starting soybean oil; therefore, it was not possible to determine its *DOE* in the present study. ESOs containing 50 and 75% *DOE* were prepared, and Vikoflex® 7170 was a representative of 100% *DOE*.

2.2.2. Chemo-enzymatic epoxidation catalyzed by enzymes

About 18 g of soybean oil, 1.5 g of CALB (~8 wt% of soybean oil), and 9.24 g of 35 wt% hydrogen peroxide solution were mixed together and heated at 55°C in an incubator shaker. The mixture was then cooled and the enzyme was removed by filtration. The final product was purified in a similar way to the chemical epoxidation method.

About 0.5 g of soybean oil was mixed with 1.44 mL of 5 wt% hydrogen peroxide solution in a pH buffer of 5.35 at 30°C. The CpLIP2 content was 30, 90 and 300 U/mL. The mixture was stirred at 300 rpm with a magnetic stirrer. The enzyme was removed and final product was purified.

The number of epoxide groups per molecule of the derived ESOs was calculated from the ^{1}H-NMR spectrum [56] and the *DOE* was evaluated as described above. In order to compare the different epoxidation methods between the chemical epoxidation and the chemo-enyzmatic method, obtaining a similar *DOE* was our concern. As a result, 50 and 75% *DOE* were used.

2.3. Synthesis of acrylated epoxidized soybean oil (AESO)

AESO was prepared from a reaction between ESO and acrylic acid in a similar way to previous reports [39, 40]. About 50 g of ESO were placed in a 250 mL round-bottom flask equipped with a magnetic stirrer and a reflux condenser. Hydroquinone was used as a free radical inhibitor. The molar ratio of ESO: acrylic acid was 1:10. The reaction temperature and time was 110°C and 7 h, respectively. The mixture was cooled to room temperature and diluted with toluene before purifying by washing with distilled water. The final step was dehydration with anhydrous sodium sulfate and the solvent was evaporated using an evaporator. The number of acrylate groups/molecule of the resulting product was determined from the 1H-NMR spectrum [56]. The number of acrylate groups/molecule and epoxide groups/molecules were assigned in the sample designation of AESO.

2.4. Characterization of ESO and AESO

The ^{1}H-NMR, ^{13}C-NMR and 2D-NMR spectra were recorded qualitatively by a Unity Inova® spectrometer (Varian, Germany) at a frequency of 500 MHz using chloroform-d as a solvent. The Fourier trans-

form infrared (FTIR) spectra of the copolymer sheets were recorded by a Bruker® EQUINOX 55 spectrometer (Bruker, Rheinstetten, Germany) from 400 to 4000 cm^{-1}.

The acid value of oil corresponded to its free fatty acid content and can be expressed as the weight% of the most abundant fatty acid of the oil. The titrimetric method was based on the French standard NF T60-204 (December 1985). About 2.0 g of ESO and 40 mL of diethyl ether/ethanol (1:1 v/v) were added followed by adding 3 drops of 20 g/L ethanolic phenolphtalein solution with continuous agitation. This sample solution was titrated with a 0.1 N ethanolic potassium hydroxide solution until the pink color remained stable for at least 10 seconds. The acid value, in weight%, was calculated based on Equation (2):

$$Acid\ value\ [\%] = \frac{(V - V_0)\cdot N\cdot M}{10W} \quad (2)$$

where V was the mL of potassium hydroxide solution used for the sample titration, V_0 was the mL of potassium hydroxide solution used for the blank, N was the titer of the potassium hydroxide solution, M was the molar mass [g/mol] of the most abundant fatty acid in the sample and W was the sample weight [g].

The qualitative analysis of the ESO samples was performed by High-Performance Thin Layer Chromatography (HPTLC) on pre-coated silica gel 60 plates (200 µm thickness, 4–8 µm particle size) from Merck (Darmstadt, Germany). Samples and standards were diluted in a chloroform-methanol mixture (2:1, v/v) at a concentration of 1 mg/mL, except for the standard mixture of monoolein, diolein and triolein (0.33 mg/mL each). The sample and standard solutions were deposited on HTPLC plates in a band-shape of 10 mm width, using an automatic TLC sampler ATS4 by CAMAG® (Muttenz, Switzerland). The deposited volumes were the following: soybean oil 2 µL, ESO 4.2 µL, oleic acid (OA) 1 µL, linoleic acid (LA) 1 µL, cis-9,10-epoxystearic acid (ESA) 2 µL, cis-9,10-12,13-diepoxystearic acid (DESA) 1.3 µL. The development (65 mm migration distance) was performed vertically in an automatic developing chamber ADC2 by CAMAG, with hexane/diethyl ether/acetic acid (70:30:1; v/v/v) as the mobile phase. The plates were visualized after dipping the plate in a solution of phosphoric acid 85%/saturated aqueous copper sulphate solution/water/methanol (8:10:78:5, v/v/v/v) and heating for 10 minutes at 180ºC. The retention factors (*Rf*) of standard compounds were used for identification of the reaction products. The retention factor (*Rf*) was defined using Equation (3):

$$Rf = \frac{A}{B} \quad (3)$$

where A was the distance from the deposition line to the center of a spot and B was the distance from the starting point (deposition line) to the solvent front. The more closely the retention factor was close to 1, the more non-polar was the compound. Conversely, the more the retention factor was close to 0, the more polar was the compound.

2.5. Preparation of the AESO-co-PMMA copolymer

A mixture of 50 wt% of MMA and 50 wt% of AESO was well mixed before adding 1 wt% of benzoyl peroxide. The mixture was heated at 70°C for 15 min in a closed container before casting into a glass mold. Then, the mixture was cured at 90°C for 15 min in a thermal oven and at 90°C for 15 min in a vacuum oven sequentially.

2.6. Characterization of the AESO-co-PMMA copolymer

Dynamic mechanical thermal analysis (DMTA) was performed using a Rheometric Scientific® DMTA V (Piscataway, NJ, USA) at a frequency of 1 Hz from –80 to 180°C. The heating rate was 2°C/min in the tension mode had a strain control of 0.01%. The storage modulus (E'), the loss modulus (E'') and the loss tangent ($\tan\delta$) as a function of temperature were recorded. Differential scanning calorimetry (DSC) was carried out on a differential scanning calorimeter (Perkin Elmer® DSC7, Waltham, MA, USA) with a heating rate of 10°C/min from –50 to 100°C in a nitrogen atmosphere. Thermogravimetric analysis (TGA) was performed on a thermogravimetric analyzer (Perkin Elmer® TGA7, Waltham, MA, USA) with a heating rate of 10°C/min in a nitrogen atmosphere from 25 to 1000°C. The temperatures at 5, 10 and 50% of weight loss were determined.

A swelling test was carried out with common solvents for surface coating such as ethanol and water. The copolymer sheets with a sample size of 1 × 2 × 0.2 cm were swollen to an equilibrium state – a

constant weight. The degree of swelling was calculated based on Equation (4):

$$Degre\ of\ swelling\ [\%] = \frac{W_1 - W_0}{W_0} \cdot 100 \qquad (4)$$

where W_0 was the weight of the dried sample before the swelling test and W_1 was the weight of the swollen sample.

The gel content in the copolymer sheet was determined by the insoluble fraction left after treating with tetrahydrofuran (THF) that was a good solvent for AESO and PMMA. The copolymer sheets with the sample size of $1 \times 2 \times 0.2$ cm were immersed in THF at room temperature for 4 days. The insoluble part was removed from the solvent and dried at 60°C until the weight was constant (W_2), after approximately 24 h. The gel content was calculated based on Equation (5) [57, 58]:

$$Gel\ content\ [\%] = \frac{W_2}{W_0} \cdot 100 \qquad (5)$$

3. Results and discussion

3.1. Epoxidation of soybean oil

In order to investigate the effect of *DOE* on the AESO-co-PMMA copolymers, three *DOE* values were used: 100, 75 and 50%. It was expected that Vikoflex® 7170 has a very high *DOE* (~100%) because the C=C protons were not observed in its ^{1}H-NMR spectrum. ESO's containing 75 and 50% *DOE* were synthesized by chemical and chemo-enzymatic epoxidations. Owing to the chemical epoxidation, the reaction at 50°C for 3 h provided a 76% *DOE* and the reaction at 45°C for 1 h provided a 52% *DOE*. Their number of epoxide groups per molecule was 3.50 and 2.40, respectively. The structure of the epoxidized triglyceride was confirmed by ^{1}H-NMR, ^{13}C-NMR, 2D-NMR and FTIR (not shown here).

The chemo-enzymatic epoxidation process catalyzed by the enzyme was studied in terms of the enzyme content and reaction time. Using 8 wt% of CALB for 13.5 h produced an ESO with 72% *DOE* (3.30 epoxide groups/molecule). A lower *DOE* was obtained using milder conditions (5 wt% of CALB for 9 h). The resulting ESO contained 52% *DOE* and 2.40 epoxide groups/molecule.

The present study was a first attempt to use CpLIP2 for the preparation of ESO. Based on a preliminary study in the CpLIP2 system, the *DOE* increased with reaction time. By using 30 U/mL of CpLIP2 for 24 h, the maximum *DOE* was 60%. An increase in the CpLIP2 content and reaction time, i.e., 90 U/mL at 24 h, the *DOE* was 75–78%. A higher content of CpLIP2, i.e. 300 U/mL, did not significantly increase the *DOE*. Therefore, 90 U/mL of CpLIP2 was employed, and 49 and 78% *DOE* were obtained when the reaction time was 4 and 24 h, respectively.

3.2. Characteristics of ESO

The number of epoxide groups/molecule was calculated using the peak at $\delta = 4.0$–4.4 ppm for the glycerol backbone and the peak at 0.9 ppm for the methyl group as an internal standard and using the intensity ratio between the peak at 2.8–3.2 and 4.0–4.4 ppm [56]. This number is listed in Table 1, and it was used to represent the sample code of the ESO.

The acid value of all ESO products is listed in Table 1. This value depended on the epoxidation system. ESOs derived from the chemical epoxidation process (ESO4.60, ESO3.50, and ESO2.40) had a very low acid value (<0.6%). The CALB-based ESOs (ESO3.30-enz1 and ESO2.40-enz1) showed a higher acid value (3–4%), and the CpLIP2-based ESOs (ESO3.58-enz2 and ESO2.25-enz2) showed the highest value (46–48%). A high acid value indicated a high free fatty acid content. It

Table 1. Sample designation, number of epoxide groups, the *DOE* and acid values of the ESOs

ESO code	Epoxidation process	No. of epoxide groups/molecule	DOE [%]	Acid value [%]
ESO4.60	Chemical	4.60	–*	0.12±0.02
ESO3.50		3.50	76	0.54±0.03
ESO2.40		2.40	52	0.56±0.06
ESO3.30-enz1	CALB	3.30	72	3.59±0.02
ESO2.40-enz1		2.40	52	3.24±0.04
ESO3.58-enz2	CpLIP2	3.58	78	46.46±0.03
ESO2.25-enz2		2.25	49	48.15±0.03

*number of starting double bonds of Vikoflex® 7170 was unknown.

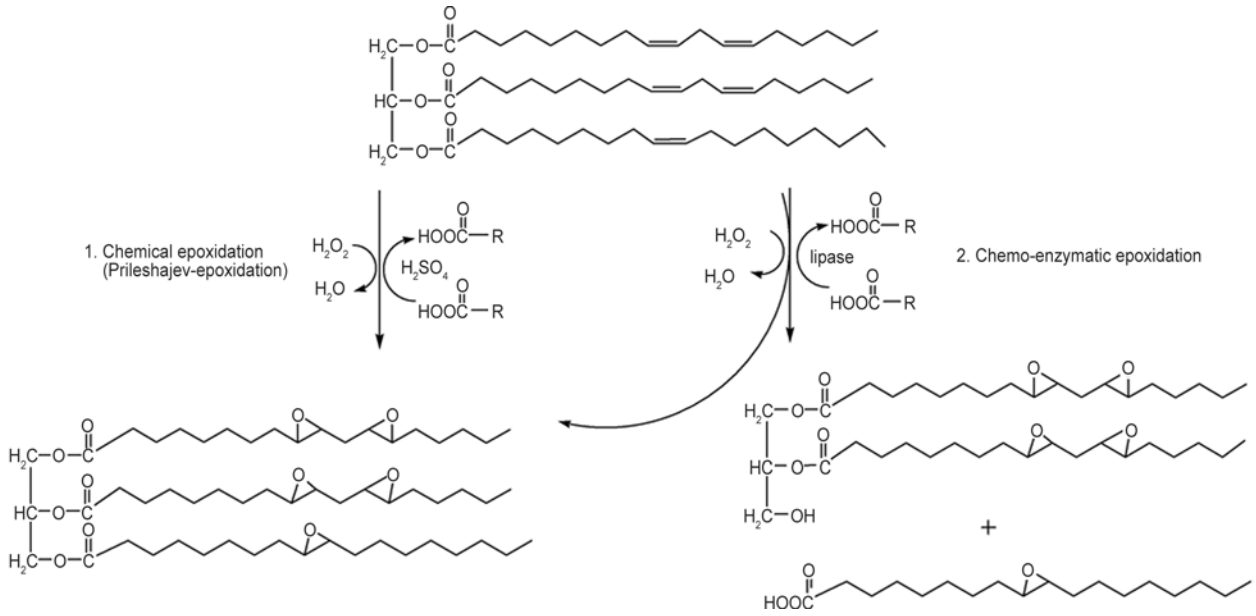

Figure 1. Schematic diagram of the chemical and chemo-enzymatic epoxidation process of soybean oil

was believed that these free fatty acids were epoxidized because the *DOE* or the number of epoxide groups/molecule of the enzyme-based ESO was as high as that of the chemical-based ESO. It was believed that CpLIP2 induced hydrolysis as well as epoxidation to provide the structure of an epoxidized mono-, di- and tri-glycerides including epoxidized free fatty acids as shown in Figure 1. These structures were substantiated by thin layer chromatography (TLC) and NMR/FTIR spectroscopy.

A thin layer chromatogram of the 14 samples listed in Table 2 is illustrated in Figure 2. Table 3 details the retention factor (*Rf*) of some epoxidized and non-epoxidized standard molecules separated by chromatography on HPTLC silica gel 60 plates. As depicted in Figure 2, the starting soybean oil (Track 1) exclusively contained triacylglycerols (TAG) that, owing to their non-polar character, was close to the front of the solvent ($Rf \approx 1$). Typically, soybean oil consists of 26.6% oleic acid, 52.8% linoleic acid and 5.4% of linolenic acid. The epoxidation of the double bonds of the oleic, linoleic and linolenic acids presented in TAGs increased the

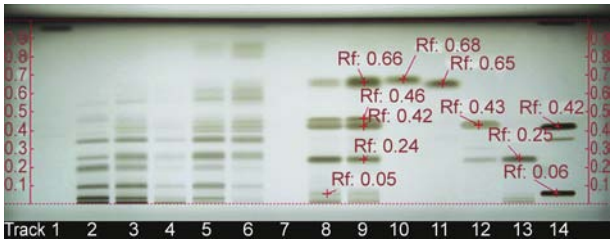

Figure 2. Thin layer chromatogram of samples listed in Table 2

Table 2. Sample ID and characteristics that corresponded to the TLC results shown in Figure 2

Track	Sample	Concentration [mg/mL]	Band width [mm]	Volume [µL]
1	Soybean oil	1	10	2.0
2	ESO4.60 (Vikoflex® 7170)	1	10	4.2
3	ESO3.50	1	10	4.2
4	ESO2.40	1	10	4.2
5	ESO3.30-enz1	1	10	4.2
6	ESO2.40-enz1	1	10	4.2
7	Blank	–		
8	ESO3.58-enz2	1	10	4.2
9	ESO2.25-enz2	1	10	4.2
10	Oleic acid (OA)	1	10	1.0
11	Linoleic acid (LA)	1	10	1.0
12	Epoxystearic acid (ESA)	1	10	2.0
13	Diepoxystearic acid (DESA)	1	10	1.3
14	MO+DO+TO*	0.33 each	10	10.0

*MO: monoolein, DO: diolein, TO: triolein

Table 3. Retention factor of some epoxidized and non-epoxidized standard molecules separated on HPTLC silica gel 60 plates

Compound type	Reference	Rf
Fully unsaturated TAG	Triolein	0.95–1.00
Partially epoxidized TAG	Triolein	0.80–0.87
Unsaturated fatty acids	Oleic acid	0.67
	Linoleic acid	0.65
Fully epoxidized fatty acids	Epoxystearic acid	0.43
	Diepoxystearic acid	0.24
Diacylglycerol	Diolein	0.42
Monoacylglycerol	Monoolein	0.05

TAG = triacylglycerols

polarity of the latter. As a result, the greater the number of epoxide groups, the more polar the TAGs. The commercial ESO, ESO4.60, (Track 2) contained neither fully unsaturated TAGs/free fatty acids ($0.63 < Rf < 0.68$) nor partially epoxidized TAGs ($0.80 < Rf < 0.87$). Moreover, its very low acid value (0.12%) meant that it was mainly composed of fully epoxidized TAGs and was probably fully or partially epoxidized di- and monoacyglycerols, and this was confirmed by the absence of DESA (Rf= 0.24) and only traces of ESA (Rf= 0.43) as shown in Table 3.

Samples of the chemically prepared ESO (Track 3 and 4) having a *DOE* of 76 and 52% respectively, exhibited a very similar profile to that of Vikoflex® 7170 (ESO4.60). The main differences essentially concerned compounds with Rf values > 0.35, that corresponded to partially epoxizided species and that again was consistent with the epoxidation content of these samples.

Profiles of the samples chemo-enzymatically epoxidized with CALB (Novozyme® 435) in track 5 and 6 were similar to the chemically prepared ESO. However, they contained significant amounts of fully unsaturated TAGs, thus revealing the incomplete conversion of soybean oil, but also there were partially epoxidized TAGs and fatty acids (no band exactly matched the fatty acid standards). It is worth mentioning that, despite the high water activity of the reaction medium, the hydrolysis of substrate and products remained limited as was shown by the moderate acid values of both samples (3.2–3.6%).

Finally, the composition of samples from the chemo-enzymatic epoxidation with CpLIP2 was radically different from all the others. Soybean oil was completely converted into unsaturated fatty acids ($0.65 < Rf < 0.68$), mono- and di-epoxidized fatty acids (ESA, Rf = 0.43; DESA, Rf = 0.24) and most likely mono- and diacylglycerols (Rf = 0.05 and Rf = 0.42 respectively). These results agreed well with the high acid values of the two samples that ranged from 46 to 48%. Thus, it can be assumed that in the CpLIP2 mediated epoxidation, hydrolysis reactions (substrates and peracids) were faster than the epoxidation itself.

To verify the ESO structure, ^{1}H-NMR and ^{13}C-NMR spectroscopy were used. Figure 3 shows the ^{1}H-NMR spectra of soybean oil, commercialized ESO and synthesized ESO, and their chemical shift (δ) assignment are listed in Table 4. The presence of an epoxide ring in all the ESO was confirmed with a δ at 2.8–3.2 ppm, epoxy proton (position 4 in the chemical structure). The glyceride backbone in the soybean oil was assigned to the δ at 4.0–4.4 and 5.1, and the δ at 5.2–5.6 ppm (methylene proton) represented the unsaturation or carbon-carbon double bond (C=C) of soybean oil (position 1 in the chemical structure). It was observable that there was no C=C in the commercialized ESO (ESO4.60) whereas the C=C bands continued to appear in the synthe-

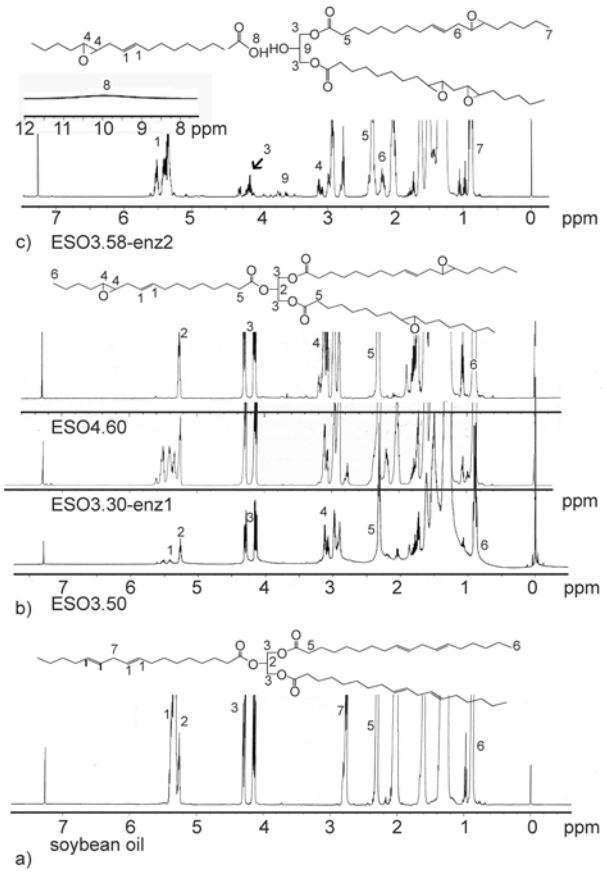

Figure 3. ^{1}H-NMR spectra: (a) soybean oil; (b) ESO4.60, ESO3.30-enz1 and ESO3.50; and (c) ESO3.58-enz2

Table 4. Assignment of the ^{1}H-NMR spectra of soybean oil, epoxidized soybean oil and epoxidized fatty acids

Chemical shift, δ [ppm]	Structure	Assignment
0.88 (triplet)		Terminal –C**H**$_3$
1.5 (broad singlet)		β–C**H**$_2$– to epoxy group
1.7 (broad singlet)	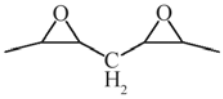	–C**H**$_2$– adjacent to two epoxy group
2.0 (broad singlet)		–C**H**$_2$–CH=CH–
2.0 (broad singlet)		–C**H**$_2$–CH=CH–
2.0 (broad singlet)	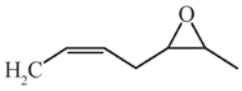	–C**H**$_2$–CH=CH–
2.2 (broad singlet)	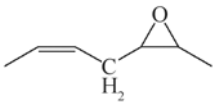	–C**H**$_2$– adjacent to one epoxy group and one C=C group
2.8 (broad singlet)	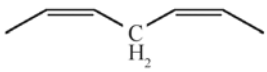	–C**H**$_2$– adjacent to two C=C group
2.9	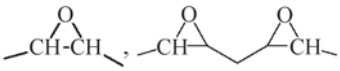	–C**H**– proton of epoxy group
3.1	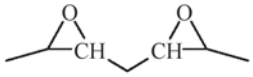	–C**H**– proton of epoxy group
3.7 (doublet)	OH–C**H**$_2$	C**H**$_2$ in diglyceride
4.0–4.4	C**H**$_2$–CH–C**H**$_2$	–C**H**$_2$– of glycerol backbone
5.1	CH$_2$–C**H**–CH$_2$	–C**H**– of glycerol backbone
5.3	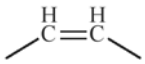	–C**H**– proton of C=C group
5.4	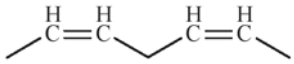	–C**H**– proton of C=C group

sized ESO from both the chemical and chemo-enzymatic epoxidations. The chemical- and CALB-based epoxidation seemed to produce a similar product based on their ^{1}H-NMR spectra. In contrast, epoxidation with CpLIP2 led to a different chemical structure as shown in Figure 3c. The disappearance of the glyceride protons at 4.2 ppm and the appearance of a methylene attached to a hydroxyl group at 3.7 ppm (position 9) in the diglyceride of ESO catalyzed by CpLIP2 were noticed. The inserted figure showed a small signal at 10 ppm that was assigned to a carboxylic acid (COOH) proton. These results substantiated the assumption that the hydrolysis of triglyceride by CpLIP2 produced the mono- or di-glyceride that generated the epoxidized free fatty acid in the CpLIP2-based ESO. The ^{13}C-NMR and 2D-NMR results (not shown here) agreed with the results described above. Both the TLC and NMR results indicated that the chemical-based ESO and the CALB-based ESO had epoxidized triglycerides while the CpLIP2-based ESO contained a mixture of epoxidized monoglycerides, epoxidized diglycerides, epoxidized triglycerides, and epoxidized free fatty acids.

Figure 4 shows the FTIR spectra of ESOs. All ESOs showed the C=O ester peak of the triglyceride at 1750 cm^{-1}. A unique peak at 1725 cm^{-1} was found only in the CpLIP2-based ESO (ESO3.45-enz2). It

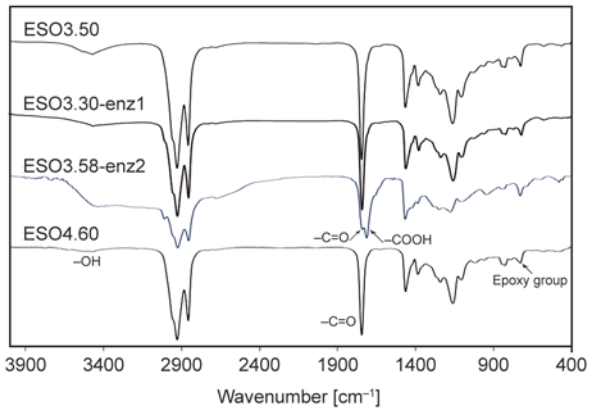

Figure 4. FTIR spectra of ESOs

belongs to the C=O ester peak of the carboxylic acid (COOH). The presence of epoxidized free fatty acid in the CpLIP2-based ESO was again proven by the FTIR result.

3.3. Acrylation of ESO and the characteristics of AESO

The formation of an acrylate group was determined using ^{1}H-NMR. Figure 5 shows the ^{1}H-NMR spectra of AESOs. The new peaks after acrylation were the peaks at 5.8–6.7 ppm that were assigned to the 3 protons of the acrylate esters. The AESOs also had peaks at 5.3–5.6 ppm (–C**H**=C**H**–) and 3.0–3.2 ppm (epoxide proton) which indicated an incomplete acrylation reaction. The acrylate group in AESO was investigated by FTIR spectroscopy (not shown here). We observed a peak at 1400, 985, 810 cm^{-1} that was attributed to the $CH=CH_2$ (acrylate group) and the peak of the residual epoxy groups at 822, 845 cm^{-1}. The number of acrylate groups/molecule of AESO calculated from its ^{1}H-NMR spectrum [56] is shown in Table 5. The number of acrylate

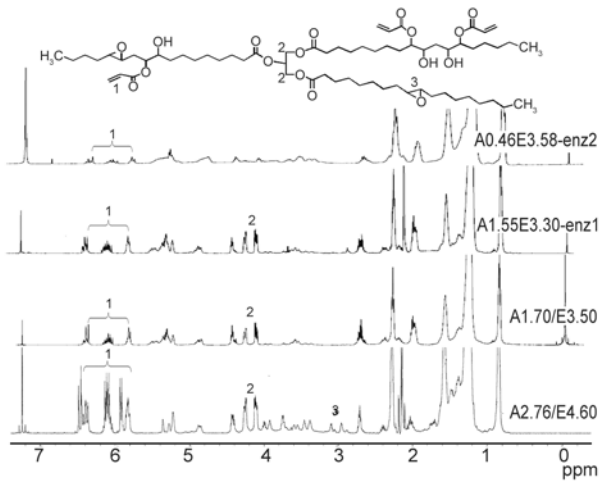

Figure 5. ^{1}H-NMR spectra of AESOs

groups of the AESO derived from the synthesized ESO was in the range of 0.42–1.70 while that from Vikoflex® 7170 was highest (2.76). An incomplete acrylation reaction was also found in the commercialized AESO (Ebecryl® 860) that have 3.50 acrylate groups/molecule (not shown here). Based on our knowledge, the complete acrylation reaction of ESO has not been reported. It should be noted that two samples, A1.54/E2.40 and A1.54/E2.40-enz1, were good representatives for comparisons between the chemical epoxidation and chemo-enzymatic epoxidation on the characteristics of the copolymer. They had the same number of epoxide groups and number of acrylate groups.

The number of acrylate groups represents the degree of acrylation. Typically, the acrylation reaction has a first-order dependence on the epoxide concentration of oil, pure triglyceride and fatty acid methyl ester. It seemed that the effect of the number of epoxide groups (or *DOE*) on the number of acrylate groups appeared only in the AESOs derived from the chemical-based ESO, i.e., the number of acrylate groups decreased from 1.70 to 1.54 when the number of epoxide groups decreased from 3.50 to 2.40 (Table 5). In contrast, the acid value played an important role on the acrylation of the enzyme-based ESOs for which the numbers of their acrylate groups did not change significantly although their numbers of epoxide groups were different. The CALB-based ESOs had 2 epoxide contents i.e., 3.30 (ESO3.30-enz1) and 2.40 (ESO2.40-enz1). After acrylation, the derived AESOs showed a similar number of acrylate groups, i.e., 1.55 (A1.55/E3.30-enz1) and 1.54 (A1.54/E2.40-enz1). This behavior was more clearly observed in the CpLIP2-based AESOs. Their starting ESO had a significantly different epoxide content, i.e., 3.58 (ESO3.58-enz2) and 2.25 (ESO2.25-enz2), but the derived AESOs had a similar number of acrylate groups, i.e.

Table 5. Sample designation and number of acrylate groups of the AESO

AESO code	No. of acrylate groups/molecule in AESO	No. of epoxide groups/molecule in ESO
A2.76/E4.60	2.76	4.60
A1.70/E3.50	1.70	3.50
A1.54/E2.40	1.54	2.40
A1.55/E3.30-enz1	1.55	3.30
A1.54/E2.40-enz1	1.54	2.40
A0.46/E3.58-enz2	0.46	3.58
A0.42/E2.25-enz2	0.42	2.25

0.42–0.46. This was because the epoxide group reacted with the carboxylic group of the epoxidized free fatty acid by an addition reaction [59, 60]. This indicated that the presence of epoxidized free fatty acid was very important for further modifications of ESO. The number of epoxide groups/molecule may not be a key factor for the synthesis of AESO by using the enzymatic ESO. The free fatty acid formed during the chemo-enzymatic epoxidation was able to be epoxidized and that was a reason for the high number of epoxide groups found in the ESO3.58-enz2. The occurrence of the carboxylic groups in the epoxidized free fatty acids did not favor the attraction of acrylic acid. Therefore, their number of acrylate groups was very low, i.e., 0.46.

3.4. Characteristics of the AESO-co-PMMA copolymer

The thermal stability of the AESO-co-PMMA copolymer was determined in terms of the thermal degradation temperature (T_d) at a selected weight loss such as 5, 10 and 50%. TGA thermograms of the copolymers are demonstrated in Figure 6 and their T_d are listed in Table 6. Sample designations of the copolymers followed the name of the AESO which included the number of acrylate groups and the number of epoxide groups. For example, Co-A2.76/E4.60 and Co-A1.55/E3.30-enz1 was synthesized from A2.76/E4.60 and A1.55/E3.30-enz1, respectively. PMMA had the lowest thermal stability because of its linear molecular structure. The network structure produced a much higher thermal stability of the copolymers, except for Co-A0.46/E3.58-enz2 that showed a slightly higher thermal stability than PMMA due to its low crosslinking. Excluding Co-A0.46/E3.58-enz2, there was no significant difference in the thermal stability among these copolymers. The high acid value and the very low acrylate groups in the CpLIP2-based AESO did not promote copolymerization with MMA. Consequently, the Co-A0.46/E3.58-enz2 was very soft and weak, and it was unable to copolymerize with A0.42/E2.25-enz2.

Table 6. Glass transition temperature (T_g) and thermal degradation temperature (T_d) of the PMMA and AESO-c-PMMA copolymer

Sample	T_g [°C]		T_d [°C] at weight loss of		
	DMTA	DSC	5%	10%	50%
PMMA	94	–	236	274	360
Co-A2.76/E4.60	40	3.92	340	368	425
Co-A1.70/E3.50	14	–15.96	278	355	427
Co-A1.55/E3.30-enz1	–1	–23.54	324	364	426
Co-A1.54/E2.40	–9	–26.13	313	359	422
Co-A1.54/E2.40-enz1	–8	–24.12	324	356	413
Co-A0.46/E3.58-enz2	N/A	N/A	236	280	383

N/A: not applicable (no data)

The glass transition temperature (T_g) of the copolymers was examined by DMTA and DSC. The tan δ as a function of the temperature of the copolymers is shown in Figure 7. The temperature at the maximum tan δ was the α transition temperature and equivalent to T_g but a different value was obtained by the DSC due to the different testing conditions. The Co-A0.46/E3.58-enz2 was unable to form a continuous sheet for DMTA testing. All copolymers and PMMA showed a very broad peak and their T_g is listed in Table 6. The T_g of PMMA was 94°C while the T_g of the copolymers were in the range of –9 to 40°C. The copolymers showed a lower T_g than PMMA although they were a thermosetting plastic. This is because the flexible and relatively short chains of the triglyceride in the copolymers

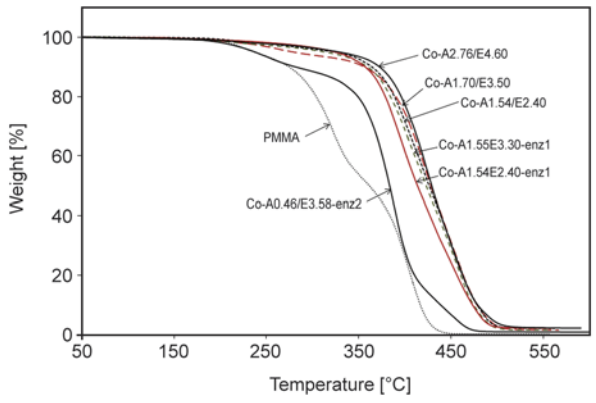

Figure 6. TGA thermograms of PMMA and AESO-co-PMMA copolymers

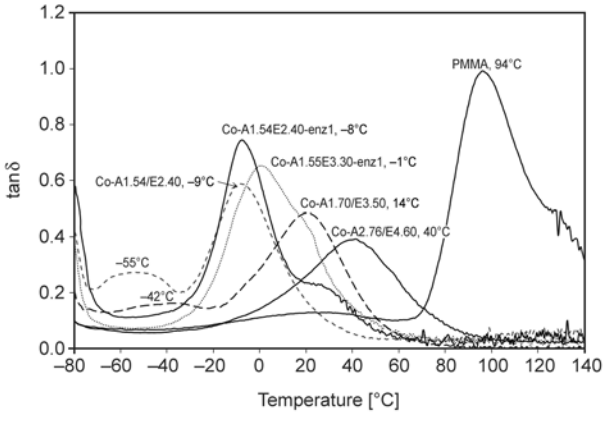

Figure 7. Tan δ as a function of the temperature of PMMA and AESO-co-PMMA copolymers

contributed to the lower T_g. The T_g also depended on the number of acrylate groups. More acrylate groups caused more crosslinking and produced a higher T_g. The single T_g indicated that a random copolymer has been derived. The Co-A1.70/E3.50 and the Co-A1.54/E2.40 showed a sub-T_g or β transition temperature while the CALB-based copolymers showed a shoulder. These may be due to phase segregation of the un-crosslinked structure or some homopolymer of PMMA, so a further study is required. The T_g of the copolymers obtained from DSC is listed in Table 6. It agreed with the results from the DMTA.

The degree of swelling in water and ethanol of the copolymers are tabulated in Table 7. The copolymers provided good stability in water (1–4%) whereas a lower stability in ethanol (15–18%) was observed. This is because ethanol is less polar than water; therefore, ethanol could penetrate into the non-polar chains of the copolymers more than water. Generally speaking, there were only slight differences in the degree of swelling among those copolymers.

Tetrahydrofuran (THF) is a good solvent of PMMA and AESO. To compare the crosslink density among these copolymers, the solubility in THF was investigated and reported as gel content (Table 7). The higher gel content indicated a higher density of crosslinks. The Co-A2.76/E4.60 had the highest gel content owing to it having the highest number of acrylate groups whereas the A0.46/E3.58-enz2 had the lowest gel content. The chemo-enzymatic epoxidation produced the lower gel content because of the formation of epoxidized free fatty acids that was attributed to a reduction in the molecules that could be crosslinked (epoxidized triglycerides). This effect was obvious in the A0.46/E3.58-enz2 with its starting ESO having a very high acid value and a high number of epoxide groups. On the other hand, the gel contents of the CALB-based copolymers were slightly lower than those of the chemical-based copolymers. Comparing the Co-A1.54/E2.40 with the Co-A1.54/E2.40-enz1, their physical properties were in the same range. Their T_g was –26 and –24°C, and their α transition temperature was –9 and –8°C, respectively. Furthermore, their degree of swelling was also similar. This behavior implied that the small acid value in the CALB-based ESO (~ 3%) did not affect the copolymerization. However, the presence of the free fatty acid in the CALB-based ESO did influence the degree of acrylation and copolymerization.

Table 7. The degree of swelling and gel content of the AESO-co-PMMA copolymer

Sample	Degree of swelling [%]		Gel content [%] (THF)
	Ethanol	Water	
Co-A2.76/E4.60	15.39	3.79	96.68
Co-A1.70/E3.50	16.89	3.58	92.27
Co-A1.55/E3.30-enz1	14.70	1.19	90.46
Co-A1.54/E2.40	17.08	0.98	91.50
Co-A1.54/E2.40-enz1	17.67	0.62	89.99
Co-A0.46/E3.58-enz2	–	–	65.58

Finally, we proposed models of the molecular structure of the copolymers which depended on the epoxidation method as shown in Figure 8. Figure 8a shows the molecular structure of the AESO-co-PMMA copolymer derived from the chemical epoxidation. By using chemo-enzymatic epoxidation, the molecular structure varied based on the epoxidized products. The epoxidized triglycerides provided the network structure as shown in Figure 8a. The epoxidized diglycerides with or without the free fatty acids would generate the network (Figure 8b). The epoxidized free fatty acids may lead to the crosslinked or linear structure that depended on the number of acrylate groups per fatty acid chain (Figure 8c and 8d).

4. Conclusions

The present work has provided a systematic study on the effect of the epoxidation process of soybean oil on the characteristics of the epoxidized soybean oil, acrylated epoxidized soybean oil, and acrylated epoxidized soybean oil-co-poly(methyl methacrylate) copolymer. Two different epoxidation processes were carried out: a chemical and chemo-enzymatic epoxidation. Novozyme® 435, lipase B from *Candida antarctica* (CALB) and an enzyme lipase/acyltransferase CpLIP2 (*Candida parapsilosis*) were employed. The epoxidation process had a strong influence on the resulting product. The CpLIP2-based epoxidation also generated free fatty acids, monoglycerides and diglycerides due to the hydrolysis reaction and subsequently these became epoxidized products, as indicated by a very high acid value and the ^{1}H-NMR and FTIR spectra and TLC chromatograms. The dependence of the acrylation reaction on the epoxide content or degree of epoxidation was observed only in the chemical-based epoxidized soybean oil. The presence of the epoxi-

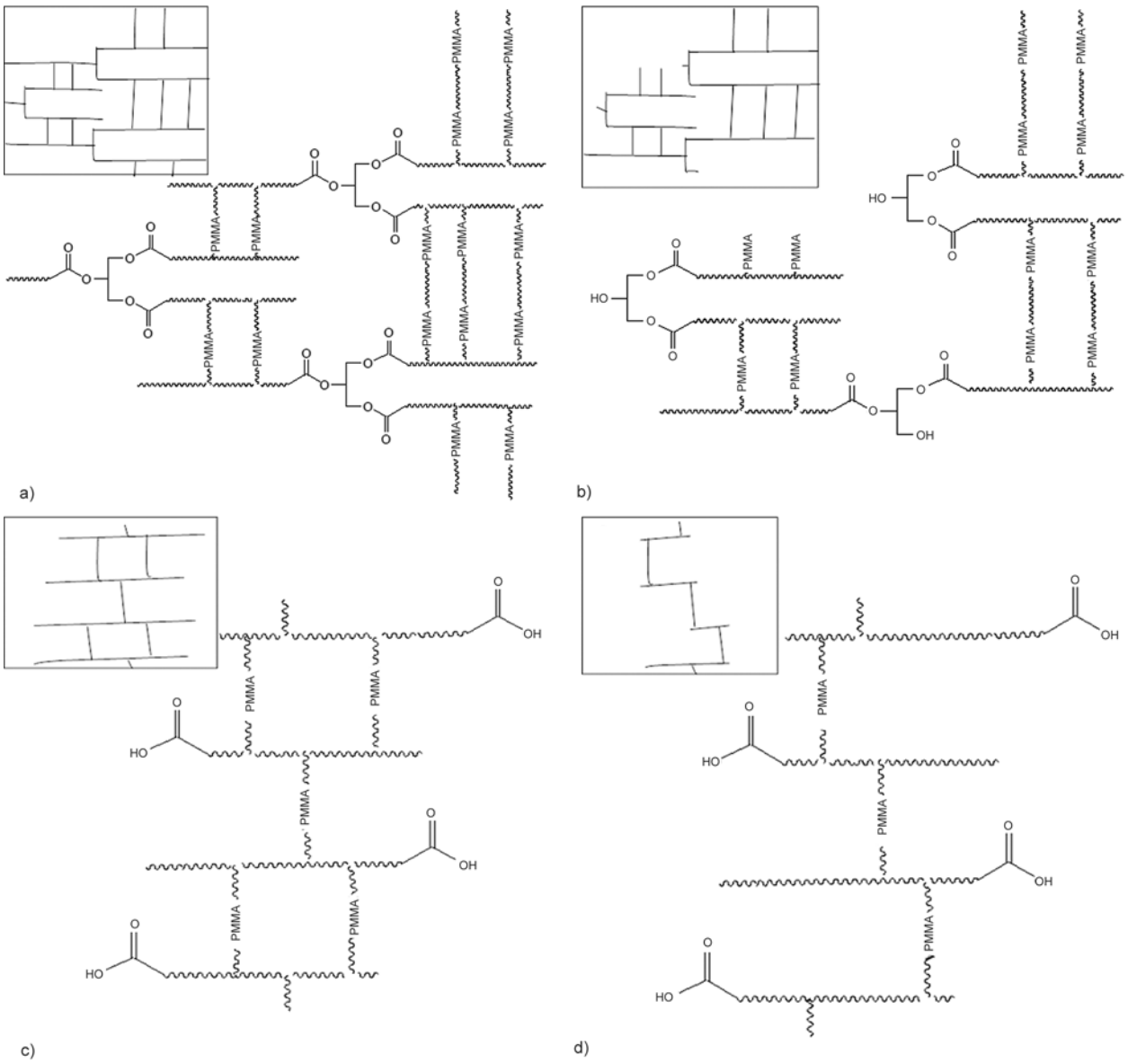

Figure 8. Molecular structure modeling of the AESO-co-PMMA copolymer derived from (a) the epoxidized triglyceride; (b) the epoxidized diglyceride with or without the free fatty acid; and (c–d) the epoxidized free fatty acid

dized free fatty acids in the enzymatic ESOs played a major role on the acrylation reaction. The higher the acid value in the ESO, the lower were the numbers of acrylate groups in the AESO obtained. The presence of carboxylic groups impeded the acrylation reaction. CpLIP2 was not suitable for synthesis of ESO under the present conditions. Although the small acid value in the CALB-based ESO did not affect the copolymers' properties, but it strongly affected the number of acrylate groups of the AESO.

Acknowledgements

The authors would like to acknowledge the financial support from the Research Development and Engineering (RD&E) fund through The National Nanotechnology Center (NANOTEC) Thailand (P-10-11333) to Prince of Songkla University. Thanks to Dr. Brian Hodgson for assistance with the English.

References

[1] Sinadinović-Fišer S., Janković M., Petrović Z. S.: Kinetics of *in situ* epoxidation of soybean oil in bulk catalyzed by ion exchange resin. Journal of the American Oil Chemists' Society, **78**, 725–731 (2001). DOI: 10.1007/s11746-001-0333-9

[2] Petrović Z. S., Zlatanić A., Lava C. C., Sinadinović-Fišer S.: Epoxidation of soybean oil in toluene with peroxoacetic and peroxoformic acids – Kinetics and side reactions. European Journal of Lipid Science and Technology, **104**, 293–299 (2002).
DOI: 10.1002/1438-9312(200205)104:5<293::AID-EJLT293>3.0.CO;2-W

[3] La Scala J., Wool R. P.: Property analysis of triglyceride-based thermosets. Polymer, **46**, 61–69 (2005).
DOI: 10.1016/j.polymer.2004.11.002

[4] Esen H., Küsefoğlu S., Wool R.: Photolytic and free-radical polymerization of monomethyl maleate esters of epoxidized plant oil triglycerides. Journal of Applied Polymer Science, **103**, 626–633 (2007).
DOI: 10.1002/app.25155

[5] Bonnaillie L. M., Wool R. P.: Thermosetting foam with a high bio-based content from acrylated epoxidized soybean oil and carbon dioxide. Journal of Applied Polymer Science, **105**, 1042–1052 (2007).
DOI: 10.1002/app.26182

[6] Biresaw G., Liu Z. S., Erhan S. Z.: Investigation of the surface properties of polymeric soaps obtained by ring-opening polymerization of epoxidized soybean oil. Journal of Applied Polymer Science, **108**, 1976–1985 (2008).
DOI: 10.1002/app.27784

[7] Liu A., Erhan S. Z.: Ring-opening polymerization of epoxidized soybean oil. Journal of the American Oil Chemistists' Society, **87**, 437–444 (2010).
DOI: 10.1007/s11746-009-1514-0

[8] Grishchuk S., Karger-Kocsis J.: Hybrid thermosets from vinyl ester resin and acrylated epoxidized soybean oil (AESO). Express Polymer Letters, **5**, 2–11 (2011).
DOI: 10.3144/expresspolymlett.2011.2

[9] Grishchuk S., Leanza R., Kirchner P., Karger-Kocsis J.: 'Greening' of unsaturated polyester resin based bulk molding compound with acrylated epoxidized soybean and linseed oils: Effect of urethane hybridization. Journal of Reinforced Plastics and Composites, **30**, 1455–1466 (2011).
DOI: 10.1177/0731684411421541

[10] Grishchuk S., Karger-Kocsis J.: Modification of vinyl ester and vinyl ester–urethane resin-based bulk molding compounds (BMC) with acrylated epoxidized soybean and linseed oils. Journal of Materials Science, **47**, 3391–3399 (2012).
DOI: 10.1007/s10853-011-6186-0

[11] Guo A., Cho Y., Petrović Z. S.: Structure and properties of halogenated and nonhalogenated soy-based polyols. Journal of Polymer Science Part A: Polymer Chemistry, **38**, 3900–3910 (2000).
DOI: 10.1002/1099-0518(20001101)38:21<3900::AID-POLA70>3.0.CO;2-E

[12] Eren T., Küsefoğlu S. H.: Synthesis and polymerization of the bromoacrylated plant oil triglycerides to rigid, flame-retardant polymers. Journal of Applied Polymer Science, **91**, 2700–2710 (2004).
DOI: 10.1002/app.13471

[13] Li F., Hanson M. V., Larock R. C.: Soybean oil–divinylbenzene thermosetting polymers: Synthesis, structure, properties and their relationships. Polymer, **42**, 1567–1579 (2001).
DOI: 10.1016/S0032-3861(00)00546-2

[14] Li F., Larock R. C.: New soybean oil–styrene–divinylbenzene thermosetting copolymers. I. Synthesis and characterization. Journal of Applied Polymer Science, **80**, 658–670 (2001).
DOI: 10.1002/1097-4628(20010425)80:4<658::AID-APP1142>3.0.CO;2-D

[15] Li F., Larock R. C.: New soybean oil–styrene–divinylbenzene thermosetting copolymers. II. Dynamic mechanical properties. Journal of Polymer Science Part B: Polymer Physics, **38**, 2721–2738 (2000).
DOI: 10.1002/1099-0488(20001101)38:21<2721::AID-POLB30>3.0.CO;2-D

[16] Li F., Larock R. C.: New soybean oil-styrene-divinylbenzene thermosetting copolymers. III. Tensile stress–strain behavior. Journal of Polymer Science Part B: Polymer Physics, **39**, 60–77 (2001).
DOI: 10.1002/1099-0488(20010101)39:1<60::AID-POLB60>3.0.CO;2-K

[17] Li F., Larock R. C.: New soybean oil-styrene-divinylbenzene thermosetting copolymers. IV. Good damping properties. Polymers for Advanced Technology, **13**, 436–449 (2002).
DOI: 10.1002/pat.206

[18] Li F., Larock R. C.: New soybean oil–styrene–divinylbenzene thermosetting copolymers. V. Shape memory effect. Journal of Applied Polymer Science, **84**, 1533–1543 (2002).
DOI: 10.1002/app.10493

[19] Luo Q., Liu M., Xu Y., Ionescu M., Petrović Z. S.: Thermosetting allyl resins derived from soybean oil. Macromolecules, **11**, 7149–7157 (2011).
DOI: 10.1021/ma201366e

[20] Lu J., Khot S., Wool R. P.: New sheet molding compound resins from soybean oil. I. Synthesis and characterization. Polymer, **46**, 71–80 (2005).
DOI: 10.1016/j.polymer.2004.10.060

[21] Xu J., Liu Z., Erhan S. Z.: Viscoelastic properties of a biological hydrogel produced from soybean oil. Journal of the American Oil Chemists' Society, **85**, 285–290 (2008).
DOI: 10.1007/s11746-008-1193-2

[22] Tanrattanakul V., Saithai P.: Mechanical properties of bioplastics and bioplastic–organoclay nanocomposites prepared from epoxidized soybean oil with different epoxide contents. Journal of Applied Polymer Science, **114**, 3057–3067 (2009).
DOI: 10.1002/app.30842

[23] Khot S. N., Lanscala J. L., Can E., Morye S. S., Williams G. I., Palmese G. R., Kusefoglu S. H., Wool R. P.: Development and application of triglyceride-based polymers and composites. Journal of Applied Polymer Science, **82**, 703–723 (2001).
DOI: 10.1002/app.1897

[24] Liu Z. S., Erhran S. Z., Xu J., Calvert P. D.: Development of soybean oil-based composites by solid free-form fabrication method: Epoxidized soybean oil with bis or polyalkyleneamine curing agents system. Journal of Applied Polymer Science, **85**, 2100–2107 (2002).
DOI: 10.1002/app.10763

[25] Liu Z. S., Erhran S. Z., Akin D. E., Barton F. E.: 'Green' composites from renewable resources: preparation of epoxidized soybean oil and flax fiber composites. Journal of Agricultural and Food Chemistry, **54**, 2134–2137 (2006).
DOI: 10.1021/jf0526745

[26] Cakmakli B., Hazer B., Tekin I. O., Kizgut S., Koksal M., Menceloglu Y.: Synthesis and characterization of polymeric linseed oil grafted methyl methacrylate or styrene. Macromolecular Bioscience, **4**, 649–655 (2004).
DOI: 10.1002/mabi.200300117

[27] Çakmakli B., Hazer B., Tekin I. O., Cömert F. B.: Synthesis and characterization of polymeric soybean oil-*g*-methyl methacrylate (and *n*-butyl methacrylate) graft copolymers: Biocompatibility and bacterial adhesion. Biomacromolecules, **6**, 1750–1758 (2005).
DOI: 10.1021/bm050063f

[28] Çakmaklı B., Hazer B., Tekin I. O., Açikgöz S., Can M.: Polymeric linoleic acid–polyolefin conjugates: Cell adhesion and biocompatibility. Journal of American Oil Chemists' Society, **84**, 73–81 (2007).
DOI: 10.1007/s11746-006-1011-7

[29] Alli A., Hazer B.: Poly(*N*-isopropylacrylamide) thermoresponsive cross-linked conjugates containing polymeric soybean oil and/or polypropylene glycol. European Polymer Journal, **44**, 1701–1713 (2008).
DOI: 10.1016/j.eurpolymj.2008.04.004

[30] Keleş E., Hazer B.: Autooxidized polyunsaturated oils/oily acids: Post-it applications and reactions with Fe(III) and adhesion properties. Macromolecular Symposia, **269**, 154–160 (2008).
DOI: 10.1002/masy.200850919

[31] Hazer D. B., Hazer B., Kaymaz F.: Synthesis of microbial elastomers based on soybean oily acids. Biocompatibility studies. Biomedical Materials, **4**, 035011/1–035011/9 (2009).
DOI: 10.1088/1748-6041/4/3/035011

[32] Hazer B., Hazer D. B., Çoban B.: Synthesis of microbial elastomers based on soybean oil. Autoxidation kinetics, thermal and mechanical properties. Journal of Polymer Research, **17**, 567–577 (2010).
DOI: 10.1007/s10965-009-9345-0

[33] Acar M., Çoban S., Hazer B.: Novel water soluble soya oil polymer from oxidized soya oil polymer and diethanol amine. Journal of Macromolecular Science Part A: Pure and Applied Chemistry, **50**, 287–296 (2013).
DOI: 10.1080/10601325.2013.755443

[34] Xia Y., Larock R. C.: Vegetable oil-based polymeric materials: Synthesis, properties, and applications. Green Chemistry, **12**, 1893–1909 (2010).
DOI: 10.1039/C0GC00264J

[35] Hong J., Luo Q., Wan X., Petrović Z. S., Shah B. K.: Biopolymers from vegetable oils via catalyst- and solvent-free 'click' chemistry: Effects of cross-linking density. Biomacromolecules, **13**, 261–266 (2012).
DOI: 10.1021/bm201554x

[36] Liu Z., Doll K. M., Holser R. A.: Boron trifluoride catalyzed ring-opening polymerization of epoxidized soybean oil in liquid carbon dioxide. Green Chemistry, **11**, 1774–1780 (2009).
DOI: 10.1039/B915742P

[37] Liu Z., Shrma B. K., Erhan S. Z.: From oligomers to molecular giants of soybean oil in supercritical carbon dioxide medium: 1. Preparation of polymers with lower molecular weight from soybean oil. Biomacromolecules, **8**, 233–239 (2007).
DOI: 10.1021/bm060496y

[38] Li Y., Fu L., Lai S., Cai X., Yang L.: Synthesis and characterization of cast resin based on different saturation epoxidized soybean oil. European Journal of Lipid Science and Technology, **112**, 511–516 (2010).
DOI: 10.1002/ejlt.200900191

[39] Saithai P., Tanrattanakul V., Chinpa W., Kaewtathip K., Dubreucq E.: Synthesis and characterization of triglyceride-based copolymer from soybean oil. Materials Science Forum, **695**, 320–323 (2011).
DOI: 10.4028/www.scientific.net/MSF.695.320

[40] Saithai P., Lecomte J., Dubreucq E., Tanrattanakul V.: Bioplastic nanocomposite prepared from acrylated epoxidized soybean oil-PMMA copolymer and nanotitanium dioxide. Advanced Science Letters, **19**, 862–865 (2013).
DOI: 10.1166/asl.2013.4811

[41] gen. Klaas M. R., Warwel S.: Complete and partial epoxidation of plant oils by lipase-catalyzed perhydrolysis. Industrial Crops and Products, **9**, 125–132 (1999).
DOI: 10.1016/S0926-6690(98)00023-5

[42] Blée E., Schuber F.: Efficient epoxidation of unsaturated fatty acids by a hydroperoxide-dependent oxygenase. Journal of Biological Chemistry, **265**, 12887–12894 (1990).

[43] Blée E.: Biosynthesis of phytooxylipins: The peroxygenase pathway. European Journal of Lipid Science and Technology: Lipid/Fett, **100**, 121–127 (1998).
DOI: 10.1002/(SICI)1521-4133(19985)100:4/5<121::AID-LIPI121>3.0.CO;2-4

[44] Piazza G. J., Foglia T. A., Nuñez A.: Optimizing reaction parameters for the enzymatic synthesis of epoxidized oleic acid with oat seed peroxygenase. Journal of the American Oil Chemists' Society, **78**, 589–592 (2001).
DOI: 10.1007/s11746-001-0309-9

[45] Piazza G. J., Nuñez A., Foglia T. A.: Epoxidation of carbon-carbon double bond with membrane bound peroxygenase. U.S. Patent 6485949, USA (2002).

[46] Piazza G. J., Nuñez A., Foglia T. A.: Epoxidation of fatty acids, fatty methyl esters, and alkenes by immobilized oat seed peroxygenase. Journal of Molecular Catalysis B: Enzymatic, **21**, 143–151 (2003).
DOI: 10.1016/S1381-1177(02)00122-4

[47] Hilker I., Bothe D., Prüss J., Warnecke H-J.: Chemoenzymatic epoxidation of unsaturated plant oils. Chemical Engineering Science, **56**, 427–432 (2001).
DOI: 10.1016/S0009-2509(00)00245-1

[48] Yadav G. D., Devi K. M.: A kinetic model for the enzyme-catalyzed self-epoxidation of oleic acid. Journal of the American Oil Chemists' Society, **78**, 347–351 (2001).
DOI: 10.1007/s11746-001-0267-2

[49] Orellana-Coca C., Billakanti J. M., Mattiasson B., Hatti-Kaul R.: Lipase mediated simultaneous esterification and epoxidation of oleic acid for the production of alkylepoxystearates. Journal of Molecular Catalysis B: Enzymatic, **44**, 133–137 (2007).
DOI: 10.1016/j.molcatb.2006.09.002

[50] Orellana-Coca C., Camocho S., Adlercreutz, D., Mahhiasson B., Hatti-Kaul, R.: Chemo-enzymatic epoxidation of linoleic acid: Parameters influencing the reaction. European Journal of Lipid Science and Technology, **107**, 864–870 (2005).
DOI: 10.1002/ejlt.200500253

[51] Orellana-Coca C., Törnvall U., Adlereutz D., Mattiasson R., Hatti-Kaul R.: Chemo-enzymatic epoxidation of oleic acid and methyl oleate in solvent-free medium. Biocatalysis and Biotransformation, **23**, 431–437 (2005).
DOI: 10.1080/10242420500389488

[52] Vlček T., Petrović Z. S.: Optimization of the chemoenzymatic epoxidation of soybean oil. Journal of the American Oil Chemists' Society, **83**, 247–252 (2006).
DOI: 10.1007/s11746-006-1200-4

[53] Tiran C., Lecomte J., Dubreucq E., Villeneuve P.: Chemo-enzymatic epoxidation of fatty compounds – Focus on processes involving a lipase-catalyzed perhydrolysis step. Dossier OCL, **15**, 179–183 (2008).
DOI: 10.1684/ocl.2008.0191

[56] de Cassia S. Schneider R., Lara L. R. S., Bitencourt T. B., da Graça Nascimento M., dos Santos Nunes M. R.: Chemo-enzymatic epoxidation of sunflower oil methyl esters. Journal of the Brazilian Chemical Society, **20**, 1473–1477 (2009).
DOI: 10.1590/S0103-50532009000800013

[55] Neugnot V., Moulin G., Dubreucq E., Bigey F.: The lipase/acyltransferase from *Candida parapsilosis*. European Journal of Biochemistry, **269**, 1734–1745 (2002).
DOI: 10.1046/j.1432-1327.2002.02828.x

[56] Campanella A., La Scala J. J., Wool R. P.: Fatty acid-based comonomers as styrene replacements in soybean and castor oil-based thermosetting polymers. Journal of Applied Polymer Science, **119**, 1000–1010 (2011).
DOI: 10.1002/app.32810

[57] Sangermano M., Malucelli G., Amerio E., Bongiovanni R., Priola A., Gianni A. D., Voit B., Rizza G.: Preparation and characterization of nanostructured TiO_2/epoxy polymeric films. Macromolecular Materials and Engineering, **291**, 517–523 (2006).
DOI: 10.1002/mame.200500420

[58] Zhang H., Qi R., Tong M., Su M., Huang M.: *In situ* solvothermal synthesis and characterization of transparent epoxy/TiO_2 nanocomposites. Journal of Applied Polymer Science, **125**, 1152–1160 (2012).
DOI: 10.1002/app.34699

[59] La Scala J., Wool R. P.: The effect of fatty acid composition on the acrylation kinetics of epoxidized triacylglycerols. Journal of the American Oil Chemists' Society, **79**, 59–63 (2002).
DOI: 10.1007/s11746-002-0435-4

[60] La Scala J. J., Sand J. M., Orlicki J. A., Robinette E. J., Palmese G. R.: Fatty acid-based monomers as styrene replacements for liquid molding resins. Polymer, **45**, 7729–7737 (2004).
DOI: 10.1016/j.polymer.2004.08.056

eXPRESS Polymer Letters Vol.7, No.11 (2013) 925–935
Available online at www.expresspolymlett.com
DOI: 10.3144/expresspolymlett.2013.90

Interfacial toughening and consequent improvement in fracture toughness of carbon fiber reinforced epoxy resin composites: induced by diblock copolymers

S. H. Deng[1], *X. D. Zhou*[1*], *M. Q. Zhu*[2], *C. J. Fan*[1], *Q. F. Lin*[2]

[1]State Key Laboratory of Chemical Engineering, East China University of Science and Technology, 130 Meilong Road, 200237 Shanghai, PR China
[2]School of Material Science and Engineering, East China University of Science and Technology, 130 Meilong Road, 200237 Shanghai, PR China

Received 6 June 2013; accepted in revised form 24 July 2013

Abstract. Carbon fibers chemically grafted with hydroxyl-terminated diblock copolymer poly (n-butylacrylate)-b-poly (glycidyl methacrylate) (OH-PnBA-b-PGMA), were used as the reinforcement for epoxy composites. The multi-filament composite specimens were prepared and measured by dynamic mechanical analysis (DMA), to study the interfacial toughness of carbon fiber reinforced epoxy composites with the diblock copolymers. The loss modulus and loss factor peaks of β-relaxation indicated that composites with diblock copolymers could dissipate more energy at small strain and possess better interfacial toughness, whereas composites without the ductile block PnBA having the worse interfacial toughness. The glass transition temperature and the apparent activation energy calculated from the glass transition showed that the strong interfacial adhesion existed in the composites with diblock copolymers, corresponding with the value of interfacial shear strength. Therefore, a strengthening and toughening interfacial structure in carbon fiber/epoxy composites was achieved by introducing the diblock copolymer OH-PnBA-b-PGMA. The resulting impact toughness, characterized with an Izod impact tester, was better than that of composite without the ductile block PnBA.

Keywords: *polymer composites, diblock copolymer, interface, fracture toughness, DMA*

1. Introduction

Carbon fiber reinforced epoxy composites are widely used in many fields, including aerospace, transportation, civil constructions, marine and automobile industries due to their good engineering properties such as high specific strength and stiffness, low density and so on. They have also attracted a long-standing attention [1–5]. However, epoxy resins are inherently brittle and hence have reduced damage tolerance, and consequently the damage tolerance of the epoxy composites. During the past decades, a large number of researches have been aimed at the toughening of epoxy composites. One of the most effective methods is by improving the matrix toughness. For example, ductile thermoplastics and rubbers were used to increase the resin toughness [6] through their plastic deformation. However, this approach may seriously affect modulus and thermal properties of the material for only a modest increase in the toughness. Other techniques include interleaving [7] or toughening with the thermoplastic fibers [8] and carbon nanotubes [9].

The other most effective method is by coating the carbon fibers with a ductile polymeric material before they are incorporated into a matrix. A variety of polymer coatings such as anhydride copolymers

*Corresponding author, e-mail: xdzhou@ecust.edu.cn

[10], acrylonitrile copolymers [11], polyvinyl alcohol [12] and epoxy coating [13] have been supplied to carbon fibers, and consequently improving the fracture toughness of reinforced composites by modifying the mode of failure and thus the potential energy absorbing capacity. However, these coatings usually provide weak bonding at the interface; thick coatings also result in the reduction of the composite strength and modulus.

Up to date, we synthesized and used the hydroxyl-terminated diblock copolymer poly (n-butylacrylate)-b-poly (glycidyl methacrylate) (OH-PnBA-b-PGMA) as macromolecular coupling agent for applying to the carbon fiber/epoxy composite to yield a strengthening and toughening interface. The Micro-Raman spectroscopy revealed that introducing flexible segment PnBA into the interface can significantly relax the interfacial stress between carbon fibers and epoxy resin. On the other hand, the microbond test showed that the interfacial shear strength of the composites (up to 52.3 MPa) was also significantly improved due to the grafting of diblock copolymer OH-PnBA-b-PGMA onto the carbon fiber surfaces [14]. However, there is no direct proof to show the improvement of the interfacial toughness and the consequent fracture toughness of composites.

The fracture behavior of polymers under large-scale deformations is of considerable interest for many thermal analysts who are interested in specifying polymers for use in critical load-bearing applications. Brostow and Corneliussen [15] and Chartoff *et al.* [16] indicated how linear viscoelastic dynamic mechanical analysis (DMA) data can be of benefit as an aid in deciding some practical criteria for selecting what material to use. The relevant relaxation processes are the first secondary relaxation below T_g. Hartmann and Lee [17] and Woo *et al.* [18] had reported a method that by doing a Fourier analysis to obtain the complete frequency spectrum of the impact pulse and comparing this spectrum with the room-temperature frequency spectrum of the loss factor of the secondary transition, the impact resistance was correlated with the secondary transition. They also obtained good agreement between the calculated value and the measured value. More recently, Karger-Kocsis *et al.* [19] reported that the intensity of the β-relaxation assigned to conformational changes of the cyclohexylene linkages correlates with the toughness of vinylester/epoxy-based thermosets. All the researches indicated that the impact properties of polymers can be correlated their β-relaxation.

To our knowledge, there are few reports about the relationship between fracture toughness with β-relaxation of fiber reinforced polymer composites, due to the complicated failure mechanisms such as matrix fracture, fiber-matrix interface debonding, post-debonding friction, fiber fracture, stress redistribution, fiber pull-out, etc. [12]. However, when small strain is given to composites, the energy absorption and dissipation is mainly dependent on the molecular chain mobility of matrix polymer and interface before failure. In other word, interfacial toughening contributes significantly to material toughness when matrix resin is fixed, and can be correlated with the β-relaxation of composites. For fiber reinforced polymer composites, we expect that they can not only absorb a large amount of impact energy when failure occurs, but dissipate energy by molecular chain mobility and deformation as encountering relatively small load. Therefore, DMA may be an effective method to analyze the interfacial toughness, although there is a philosophical difficulty in relating the DMA data to the fracture toughness of composites.

In this study, to prove that the hydroxyl-terminated diblock copolymer OH-PnBA-b-PGMA can yield a strengthening and toughening interfacial structure in carbon fiber/epoxy composites, the multi-filament composite specimens were prepared and tested by dynamic mechanical analysis (DMA), to thoroughly study the interfacial toughness of carbon fiber reinforced epoxy resin composites. The resulting impact toughness was also characterized with an Izod impact tester.

2. Experimental section

2.1. Materials

Carbon fibers (CFs) (T700, approximate diameter is 7 μm, 12 000 single filament in the tow) were purchased from Toray Industries, Inc. Japan. The surface treatments of the CFs were similar to those described in our previous study [14]. The CFs, extracted with acetone (Sinopharm Chemical Reagent Co., Ltd, AR grade, China) and petroleum ether (Shanghai Tianlian Fine Chemical Co., Ltd, AR grade, China) in a Soxhlet apparatus for 24 h respectively and then dried under vacuum at 60°C, were denoted as CF0. After extraction, the CFs were oxidized by nitric acid (Yixin Guanghui Addi-

tives Chemical Co., Ltd, AR grade, China) for 5 h at 100°C, denoted as CF-COOH. The as-prepared CF-COOH was immersed in thionyl chloride (Shanghai Lingfeng Chemical Reagent Co., Ltd, AR grade, China) and stirring at 70°C for 24 h, and then chemically grafted with the synthesized copolymers OH-PnBA-b-PGMA70 with various polymerization degrees (0, 130 and 220) of the PnBA blocks, named as CF-PGMA, CF-DI130 and CF-DI220, respectively.

The resin used in this study was the two part E-51(618)/T-31 epoxy system, provided by Shanghai Resin Factory Co. Ltd. China.

2.2. Preparation of the testing samples

2.2.1. Preparation of multi-filament composite specimens

All the multi-filament composite specimens were prepared as follows: Ten filaments were parallel aligned on a rectangular mould with a size of 30 × 5 × 0.3 mm using double-side tape, ensuring that each filament was non-overlapped to avoid the interference between interfaces. Then the resin E-51(618) and hardener T-31 were mixed with a mass ratio 10:3, poured into the mould and degassed under full vacuum to enable evaporation of entrapped air bubbles, followed by curing at 60°C for 6 h and subsequent 120°C for 5 h under compressive pressure of 200 kPa. The photograph of multi-filament specimen was shown in Figure 1. For all the specimens, the fiber contents were uniform by employing equal amounts of resin and equal numbers of filaments.

It is worth noting that the dimension of specimens must be precisely controlled, especially the thickness, significantly influencing the modulus of materials in DMA test. The specimens will be given up if their thickness does not fall in the range of 300 ~ 350 μm.

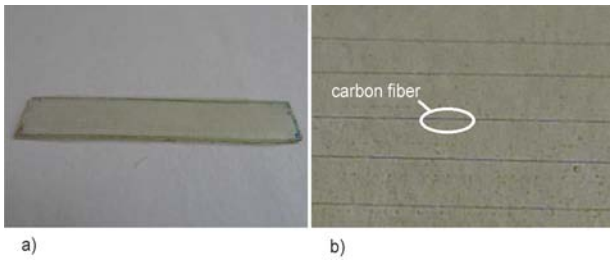

Figure 1. Samples of multi-filament composite specimens for DMA tests (a) photograph of the whole sample; (b) arrangement of single carbon fiber embedded in epoxy resin

2.2.2. Preparation of notched impact specimens

The quantitative bundles were first laid in three layers in the mould with the size of 60 × 10 × 2.5 mm, followed by pouring the quantitative resin mixture with vacuum degassing. Then the notched impact specimens of the unidirectional composites were obtained after the curing process similar to that described for the preparation of multi-filament specimens. The schematic diagram of the notched impact specimen was shown in Figure 2. The fiber content of all the notched impact specimens was 5% by weight.

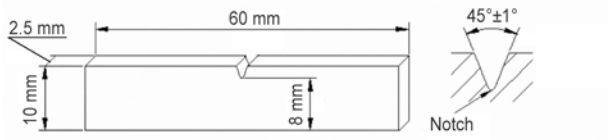

Figure 2. Schematic diagram of the notched impact specimen

2.3. Instruments and measurements

Dynamic mechanical thermal analysis (DMA) was performed in film tensile mode with a dynamic mechanical thermal analyzer (DMAQ800, TA Instruments, USA). Using DMA Multi-Frequency–Strain module, the prepared specimens were measured with various oscillation frequencies of 1, 5, 10, 30 and 50 Hz and a constant oscillation strain of 0.07%. The testing temperature ranged from –125 to 200°C at 2°C /min.

Both for the bulk matrix and for the multi-filaments composite specimens, an apparent activation energy ΔE for the glass transition has been calculated, as reported by other authors [20], using the Arrhenius equation as shown in Equation (1):

$$\omega = A \exp \frac{-\Delta E}{RT_g} \tag{1}$$

where ω is the oscillation frequency, T_g is the absolute temperature at the glass transition loss factor peak and A is a frequency factor.

The single fiber pull-out behavior of the multi-filament composites was recorded by the optical microscope (LV100POL, Nikon Corporation, Japan).

The fracture toughness of composites was evaluated using an Izod impact tester (XJU-22J, Chengde Teating Machine Co., Ltd, China) of full scale 4 J at an impact velocity of 1 m/s. The notched impact strength was calculated according to ASTM D-256

at -50°C. Each value obtained represented the average of five samples.

Scanning electron microscopy (SEM) was applicable to investigate the surface morphology of the fractured section of the impact specimens. Samples were fixed to a platform with conductive tape, vacuum-dried and sputtered with gold. Images were taken on an S-4800 scanning electron microscopy (Hitachi Company, Japan), operating at 15 kV.

3. Results and discussion

3.1. Dynamic mechanical thermal analysis

3.1.1. Multi-filament composite specimens

Considering the appropriate damping for impact would either be longitudinal or some combination of shear and longitudinal, the tensile mode was employed in DMA test. The additional advantage of this mode is benefit of the specimen preparation. It is easy for single filament to be parallel aligned in small dimension specimens. As shown in Figure 1, the multi-filament composite specimens were prepared with the dimension of 30 × 5 × 0.3 mm. To ensure all the samples been tested in linear viscoelastic region, the 0.07% oscillation strain was selected.

3.1.2. Loss modulus *E″* of β-relaxation

The variation of the dynamic loss modulus *E″* with temperature for the various samples was shown in Figure 3. The values sweeping at 5 and 50 Hz were selected respectively to be convenient for comparing. Besides the glass transition at the high-temperature end about 140 ~ 150°C, one secondary transition was found at –60 ~ –50°C. This phenomenon had been widely reported [21, 22]. The peak value of loss modulus and $S_{\beta\text{-}L}$, the area under the loss modulus curve at 5 and 50 Hz, were listed in Table 1.

For epoxy/amine networks, most authors associated the β-relaxation with the motion contributions of diphenylpropane groups and glyceryl units [21–23]. Comparing the loss modulus of the bulk matrix and the multi-filament composites at the secondary transition, the peak value of the neat epoxy resin was lower than that of CF-DI220 and CF-DI130 composites, whereas it higher than that of CF0 and CF-GMA composites, both sweeping at 5 and 50 Hz. The loss modulus is the viscous component of complex modulus and is related to the sample's ability to dissipate mechanical energy as heat through the molecular motion per cycle of sinusoidal deformation, when different systems are compared at the

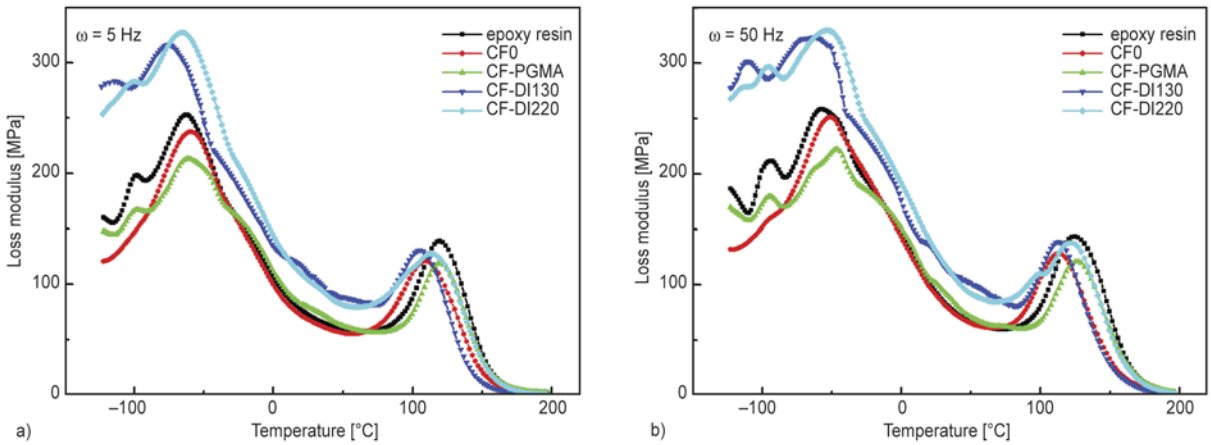

Figure 3. Loss modulus of various samples as a function of temperature, sweeping at (a) 5 Hz and (b) 50 Hz, respectively

Table 1. Data about β-relaxation of carbon fiber/epoxy resin composites

Sample	5 Hz			50 Hz		
	Loss modulus [MPa]	$S_{\beta\text{-}L}\cdot10^{-3}$	$S_{\beta\text{-}\delta}$	Loss modulus [MPa]	$S_{\beta\text{-}L}\cdot10^{-3}$	$S_{\beta\text{-}\delta}$
Epoxy	252.7	27.6	9.2	258.0	31.5	10.3
CF0	237.3	25.2	7.5	251.3	29.0	8.6
CF-PGMA	213.2	25.7	8.9	222.3	29.2	9.9
CF-DI130	316.8	31.2	12.9	323.1	41.5	13.9
CF-DI220	327.4	38.5	13.1	328.9	43.1	14.3

$S_{\beta\text{-}L}$ is area under the loss modulus curve, $S_{\beta\text{-}\delta}$ is area under the tan δ curve.

same strain amplitude. It is most sensitive to the molecular motions. The dissipation from the mechanical energy into thermal energy per cycle is described in Equation (2) [18]:

$$\Delta W(\omega) = \int_{''}^{2\pi/\omega} \sigma(\omega)\cdot\varepsilon(\omega)\mathrm{d}t$$

$$= \omega\cdot\sigma_0\cdot\varepsilon_0\int_0^{2\pi/\omega}[\cos\omega t\cdot\sin\omega t\cdot\cos\delta + \sin^2\omega t\cdot\sin\delta]\mathrm{d}t$$

$$= \pi\cdot\varepsilon_0^2(\omega)\cdot E''(\omega) \qquad (2)$$

where $\sigma(\omega)$ is the stress at frequency ω, $\varepsilon(\omega)$ is the resulting strain at ω with amplitude ε_0, δ is the phase angle between stress and the strain, $E''(\omega)$ is the loss modulus at ω.

It was found that $S_{\beta\text{-L}}$, area under the loss modulus curve, also had the similar trend as that of loss modulus: CF-DI220 > CF-DI130 > epoxy resin > CF0 ≈ CF-GMA.

Thus, it implied that the energy dissipation capacity of the neat epoxy resin was lower than that of CF-DI220 and CF-DI130 composites, and higher than that of CF0 and CF-GMA composites. At small strain (0.07%), the multi-filament composites have no detectable matrix fracture and fiber pull-out, the variation of toughness is mainly contributed by the interfacial toughness as the resin matrix is fixed. We have known that the glass transition of PnBA block in diblock copolymer occurs at about –50°C. It can increase the frictional shear work due to its high viscosity and the plastic deformation at the interface, and act as a stress relief medium which reduces compressive stresses caused by matrix shrinkage during curing and as a crack inhibitor [24]. In our previous study, Micro-Raman spectroscopy has also revealed the interfacial stress can significantly be relaxed owing to introducing the flexible segment PnBA [14]. Thus, the CF-DI220 and CF-DI130 composites possess better energy dissipation capacity and toughness than the neat epoxy matrix. It was noted that CF0 multi-filament composite showed lower energy dissipation than the neat epoxy matrix. Commonly, weak interfacial adhesion provides slight limit to the neighboring chain motion; whereas good interfacial adhesion seriously restricts the movement of the chain segments, resulting in the worst interfacial toughness of CF-GMA composite.

3.1.3. Loss factor tan δ of β-relaxation

The loss factor tan δ is the ratio of loss modulus to storage modulus, and represents the mechanical damping or the internal friction in a viscoelastic system. Compared with loss modulus, the loss factor eliminates the effect of sample's geometrical shapes. The variation of loss factor tanδ with temperature for various samples was shown in Figure 4, and $S_{\beta\text{-}\delta}$, the area under the tanδ curve was also shown in Table 1.

As can be seen from Table 1 and Figure 4, $S_{\beta\text{-}\delta}$ ranged as: CF-DI220 > CF-DI130 > epoxy resin > CF-GMA > CF0, both sweeping at 5 and 50 Hz. The similar trend with that of loss modulus, composites with diblock copolymer possessing the best interfacial toughness and composites without the ductile block PnBA having the worse interfacial toughness, was very significant. This is not in accordance with the principle that a composite with a poor matrix/fiber load transfer tends to dissipate more energy than one with good interfacial interaction [25]. As reported in our recent study, the micro-composite with diblock copolymer coupling agent had strong

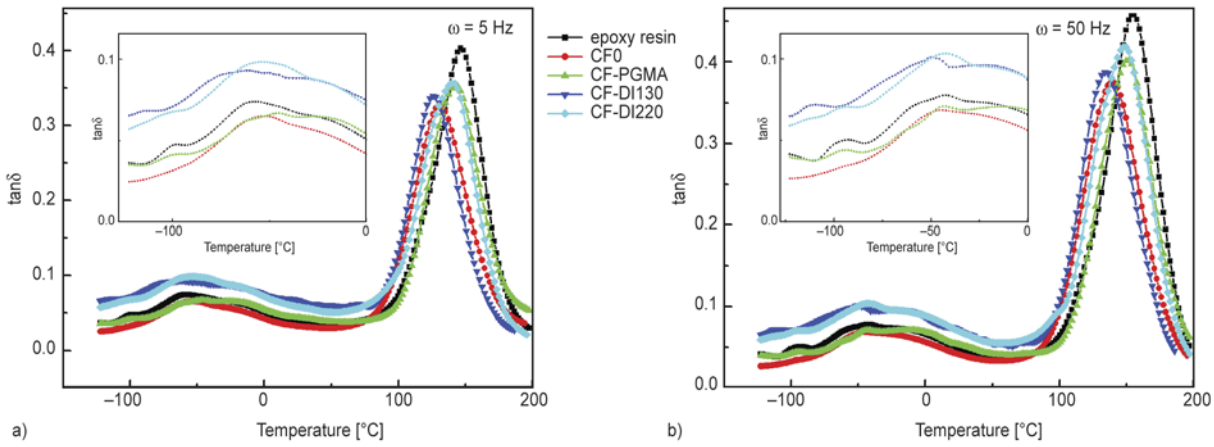

Figure 4. Loss factor of various samples as a function of temperature, sweeping at (a) 5 Hz and (b) 50Hz, respectively

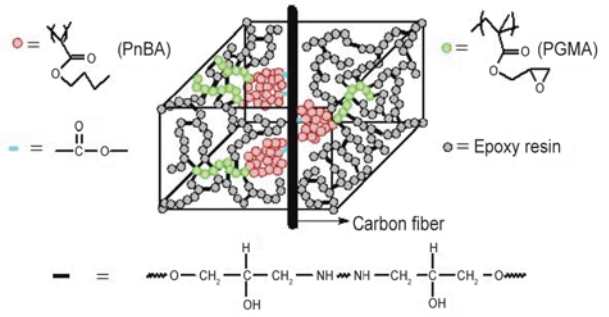

Figure 5. Schematic illustration on the interactions of grafted diblock copolymer at the interface between CF and epoxy resin

interfacial shear strength of 49.0 MPa (CF-DI220), while the micro-composite with PGMA and CF0 had only interfacial shear strength of 40.2 and 29.8 MPa, respectively [14].

We have reported in our other paper that, the ductile block PnBA will act as the ductile interlayer collapsing on fiber surface due to its low T_g and poor compatibility with the PGMA block and the epoxy resin [26], which is illustrated in Figure 5. It is well acceptable that the ductile PnBA interlayer with high viscosity will increase frictional shear stress at interface, and the movement of PnBA chain segments at interface also improves the plastic deformation of the interface region.

3.1.4. α-relaxation

Table 2 showed that the glass transition temperature, from the loss factor for bulk resin and composites at various testing frequencies. It is evident from the loss factor curves that all the multi-filament composites show a relaxation peak at temperatures lower than that obtained from bulk resin. Ratna [27] reported that the T_g for GFRP epoxy composite was 190°C whereas for unreinforced cured epoxy it was 217°C. Ghosh *et al*. [28] reported similar effects in the case of jute fiber reinforced composites. They explained that the organosilane coating used for commercial fibers, with unreactive organic groups led to an interface with many unrestrained or free end groups which resulted in reduction in the cross-link density of the polymer network in the interface region, and thereby caused a reduction in relaxation temperature [29]. In our experiments, we used the macromolecular coupling agents synthesized by ourselves, but not the commercial organosilane coating, the similar effects were also obtained. It was considered that the thickness of the prepared multi-filament specimens is only about 300 μm, the parallel arrangement of CF with and without coating slightly reduced the cross-link density and integrality of the polymer network in the interface region. Furthermore, for the CF0 composite, the presence of uncoated fibers can affect the initial stoichiometry of the epoxy-amine network due to the higher affinity of the carbon surface for one of the monomers. The generation of a non-stoichiometric interphase is possibly the reason of the decrease of T_g [29]. For the CF-GMA, CF-DI130 and CF-DI220 composites, some epoxy groups in PGMA block react with amine hardener during the curing process; the others unreacted are free or unrestrained and have a plasticization effect on the zone next to the interface, explaining the decrease in T_g of the composites.

Table 2. Data about α-relaxation of carbon fiber/epoxy resin composites

Sample	T_g [°C, 5 Hz]	T_g [°C, 50 Hz]	Activation energy, ΔE [kJ·mol^{-1}]
Epoxy	146.4	155.7	325.1
CF0	136.8	144.4	365.9
CF-PGMA	142.6	151.9	402.0
CF-DI130	142.2	149.8	427.9
CF-DI220	141.3	148.9	421.3

Obviously, the CF0 composite desized the commercial coating on carbon fibers had the lowest T_g. Usually, the good interfacial adhesion will restrict the chain segment movement, resulting in an increase in glass transition temperature. Thereby, the T_g of composites with macromolecular coupling agents was higher than that of CF0 composite. However, the ductile interlayer still affected the T_g. This is confirmed by the descending order of T_g value for CF-PGMA, CF-DI130 and CF-DI220 composites, in which the polymerization degree of PnBA block is 0, 130 and 220, respectively.

According to Equation (1), by plotting the logarithm of the frequency vs. the reciprocal absolute temperature corresponding to the tanδ peak, the apparent activation energy for the glass transition can be calculated from the slope of the regression line. Figure 6 showed this relationship, and the calculated values for the apparent activation energies of epoxy matrix and multi-filament composites were listed in Table 2. As can be seen, the relaxation of the epoxy matrix required the least energy compared with all the multi-filament composites. The desized fibers micro-composites CF0 had a bit higher value, implying that the molecular motion was only

slightly restricted by the reinforcing fibers. This is due to the weak interfacial adhesion between CF0 and epoxy matrix. The relaxation of the epoxy resin in composites with dibock copolymer required the most energy, relating to the best interfacial adhesion. It could be clearly seen that there was a very good agreement between the activation energy and the interfacial adhesion, indicating the strengthening and toughening interfacial structure in carbon fiber reinforced epoxy resin composites induced by diblock copolymer OH-PnBA-b-PGMA.

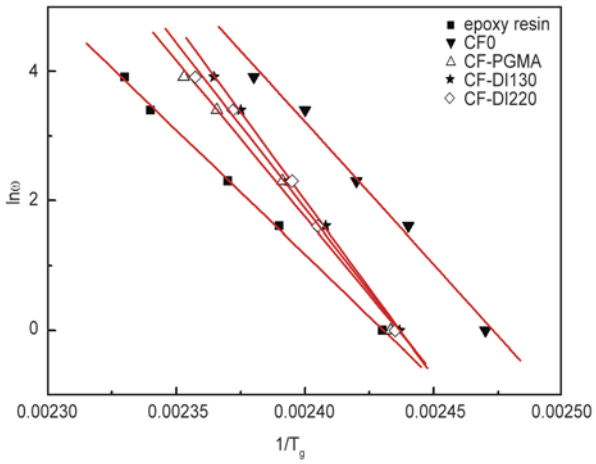

Figure 6. The relationship curves between $1/T_g$ and $\ln\omega$ in pure epoxy resin and carbon fibers with various surface modification reinforced epoxy resin composites

3.2. Single fiber pull-out

Many researchers have proved the fiber pull-out work (R_{po}) to be a predominant component of the fracture toughness (more than 90%) of carbon fiber reinforced plastics [12, 30]. Kim and Mai employed Equation (3) to estimate the fiber pull-out work:

$$R_{po} = \frac{V_f \cdot \sigma_f \cdot l_c}{12} = \frac{V_f \cdot \sigma_f \cdot \bar{l}_{po}}{3} \tag{3}$$

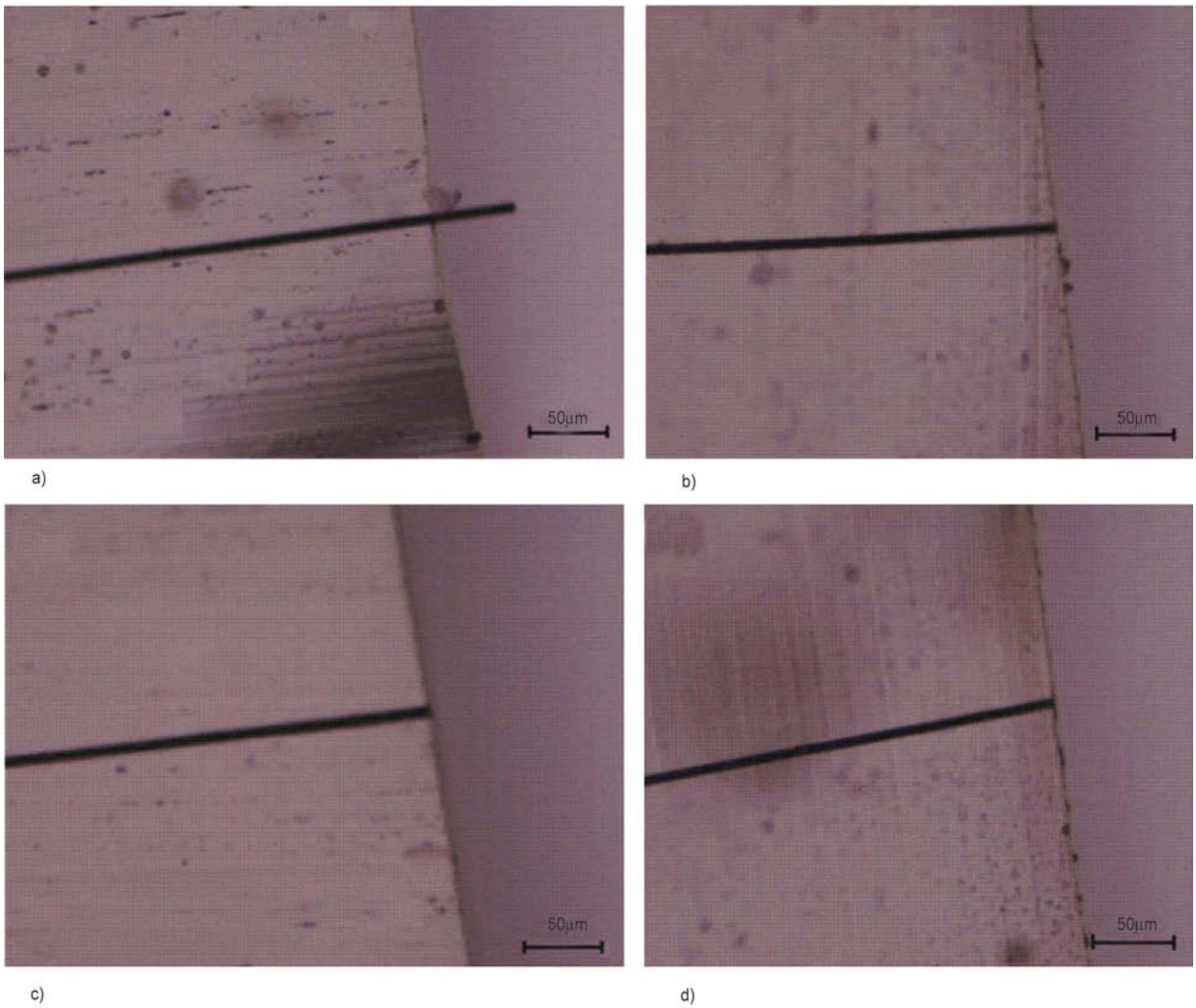

Figure 7. Optical micrographs of the multi-filament composites after fracture under the dynamic load of 50Hz. (a) CF0/epoxy resin; (b) CF-COOH/epoxy resin; (c) CF-PGMA/epoxy resin; (d) CF-DI220/epoxy resin

where V_f is the volume fraction of fibers, σ_f is the tensile strength of carbon fibres, and $\bar{l}_{po}$ is the average fiber pull-out length.

In our experiments, after specimens fracture under the dynamic load of 50 Hz, the fiber pull-out length of the multi-filament composites is easy to measure when employing optical microscope or SEM. As can be seen in Figure 7, the average fiber pull-out length and number of CF0 composite was significantly higher than all the other samples. CF-GMA, CF-DI130 and CF-DI220 composites were seldom observed the phenomenon of fiber pull-out, according with Beaumont's and Anstice [31] opinion that the debonding of single fibers seldom occurs because the debond stress is greater than the fiber strength for carbon-epoxy composites with strong interfacial bond strength and high-stiffness fibers. Therefore, for the composites with diblock copolymer, the energy dissipation cannot be improved through the interfacial debonding and fiber pull-out.

3.3. Impact fracture toughness

Figure 8 showed the notched impact strength of carbon fibers reinforced epoxy composites with various surface modifications. It can be found that the impact strength of CF0 composite was as high as 19.05±2.10 kJ/m^2. It is due to the fact that the weak interfacial bonding between CF0 and epoxy resin allows more interfacial debonding and fiber pull-out during the whole fracture process, giving large contributions to the fracture toughness of the composite. Compared to CF0 composite, much lower impact strength was observed in CF-COOH and CF-PGMA composites, only 4.50±0.52 and 3.80±1.21 kJ/m^2, respectively. This is because that

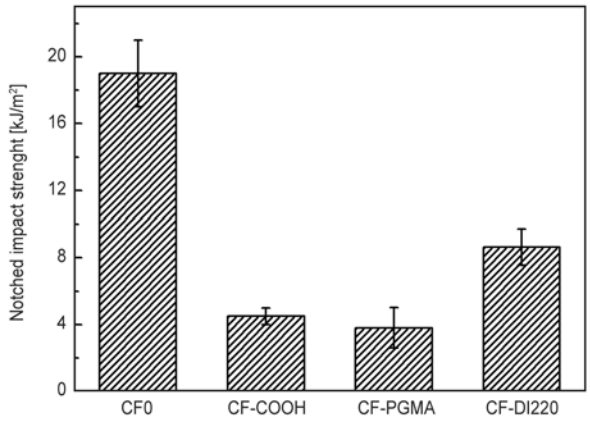

Figure 8. The notched impact strength of carbon fibers with various surface modification reinforced epoxy resin composites

the increase of the oxygen-containing functional groups on CF-COOH surface and the strong interaction between the grafted homopolymers PGMA and epoxy resin greatly improved the interfacial adhesion of the systems. In the case of strong bonding, the interfacial debonding during the fracture process is so difficult that the advancing crack propagates through the fibers, resulting in the low energy dissipation. As a consequence, the fracture toughness significantly reduced.

However, with the introducing of PnBA blocks, the impact fracture toughness of the composite was slightly increased due to the low grafting density of diblock copolymer. As we known, the strong bonding between carbon fiber and epoxy resin is essential for efficient stress transfer and thus to achieve high strength in CF-DI220 composite, suggesting that the dominant source of the fracture toughness in the system is not attributed to the said toughening mechanisms of interfacial debonding and fiber full-out, which was also indicated by the result of single fiber pull-out. It can be explained as follows: first, the flexible interlayer can bear larger imposed deformation and relax the stress concentration at interface, which delays the occurrence of interfacial slippage and the interfacial debonding, and effectively enhance the number of starting points of the material damage; second, the flexible interlayer can act as a crack arrester to prevent the crack propagation through the fibers and thus prolong the crack propagation path; finally, the composite can overall deform more largely before failure. All of these delay the material damage and increase the energy absorption capacity. Therefore, the notched impact strength of CF-DI220/epoxy resin composite was increased to 9.21±1.42 kJ/m^2.

Figure 9 demonstrated the fracture morphology in different carbon fiber reinforced epoxy resin composites. For CF0 composite, as seen in Figure 9a, CF was obviously pulled out with a smooth surface from the epoxy resin, and a number of holes were residual, proving that the main failure mechanism of the CF0 composite was the fiber debonding and pull-out. While with an increase in the interfacial adhesion, the brittle fracture occurred in CF-PGMA composite as illustrated in Figure 9b. As for CF-DI220 composite (Figure 9c), the fiber debonding phenomenon was also seldom observed due to the strong interfacial bonding. Nevertheless, the fracture model was changed with introducing the flexi-

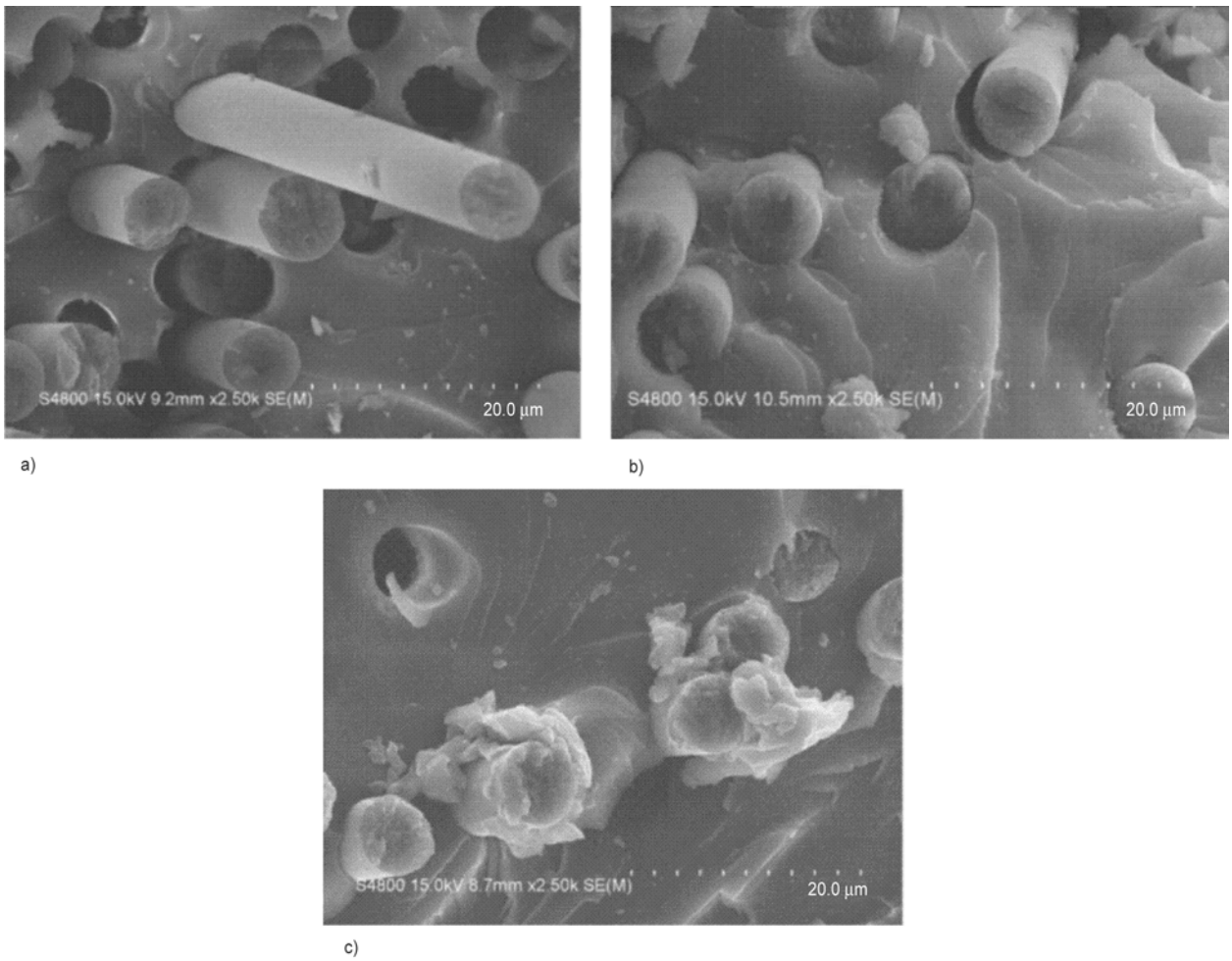

Figure 9. SEM photographs of impact fracture surfaces for (a) CF0/epoxy resin; (b) CF-PGMA/epoxy resin; and (c) CF-DI220/epoxy resin composites

ble block PnBA, where amount of the residual resin adhered around the fractured fibers.

4. Conclusions

Based on our previous study, the influence of the grafted diblock copolymer OH-PnBA-b-PGMA, which could effectively improve the interfacial adhesion between carbon fiber and epoxy resin, on the interfacial toughness and consequent fracture toughness of the composites was studied by DMA and Izod impact test in this study.

The loss modulus and loss factor peaks of β-relaxation in DMA spectra showed that the composites with diblock copolymers could dissipate more energy at small strain and possess better interfacial toughness, whereas composites without the ductile block PnBA having the worse interfacial toughness. The glass transition temperature and the apparent activation energy calculated from the glass transition displayed that the strong interfacial adhesion existed in the composites with diblock copolymers, corresponding with the value of the interfacial shear strength.

The ductile block PnBA can bear larger imposed deformation and relax the stress concentration at interface, which delays the occurrence of interfacial slippage and the interfacial debonding, increasing the energy absorption capability and thus improving the impact fracture toughness of the composites.

Therefore, it can be concluded that a strengthening and toughening interfacial structure in carbon fiber reinforced epoxy resin composite was successfully achieved by introducing the diblock copolymer OH-PnBA-b-PGMA.

Acknowledgements

The authors sincerely acknowledge the support of NSFC 51073055 and the Fundamental Research Funds for the Central Universities.

References

[1] Li M., Gu Y., Liu Y., Li Y., Zhang Z.: Interfacial improvement of carbon fiber/epoxy composites using a simple process for depositing commercially functionalized carbon nanotubes on the fibers. Carbon, **52**, 109–121 (2013).
DOI: 10.1016/j.carbon.2012.09.011

[2] Ma K., Chen P., Wang P., Cui G., Xu X.: A study of the effect of oxygen plasma treatment on the interfacial properties of carbon fiber/epoxy composites. Journal of Applied Polymer Science, **118**, 1606–1614 (2010).
DOI: 10.1002/app.32549

[3] Wang C., He X., Tong L., Peng Q., Wang R., Li Y., Li Y.: Theoretical prediction and experimental verification of pulling carbon nanotubes from carbon fiber prepared by chemical grafting method. Composites Part A: Applied Science and Manufacturing, **50**, 1–10 (2013).
DOI: 10.1016/j.compositesa.2013.03.008

[4] Zhao F., Huang Y., Liu L., Bai Y., Xu L.: Formation of a carbon fiber/polyhedral oligomeric silsesquioxane/carbon nanotube hybrid reinforcement and its effect on the interfacial properties of carbon fiber/epoxy composites. Carbon, **49**, 2624–2632 (2011).
DOI: 10.1016/j.carbon.2011.02.026

[5] Shams S. S., El-Hajjar R. F.: Overlay patch repair of scratch damage in carbon fiber/epoxy laminated composites. Composites Part A: Applied Science and Manufacturing, **49**, 148–156 (2013).
DOI: 10.1016/j.compositesa.2013.03.005

[6] Pearson R. A., Yee A. F.: Toughening mechanisms in elastomer-modified epoxies. Journal of Materials Science, **24**, 2571–2580 (1989).
DOI: 10.1007/BF01174528

[7] Kuwata M., Hogg P. J.: Interlaminar toughness of interleaved CFRP using non-woven veils: Part 1. Mode-I testing. Composites Part A: Applied Science and Manufacturing, **42**, 1551–1559 (2011).
DOI: 10.1016/j.compositesa.2011.07.016

[8] Wong D. W. Y., Lin L., MaGrail P. T., Peijs T., Hogg P. J.: Improved fracture toughness of carbon fibre/epoxy composite laminates using dissolvable thermoplastic fibres. Composites Part A: Applied Science and Manufacturing, **41**, 759–767 (2010).
DOI: 10.1016/j.compositesa.2010.02.008

[9] Gkikas G., Barkoula N-M., Paipetis A. S.: Effect of dispersion conditions on the thermo-mechanical and toughness properties of multi walled carbon nanotubes-reinforced epoxy. Composites Part B: Engineering, **43**, 2697–2705 (2012).
DOI: 10.1016/j.compositesb.2012.01.070

[10] Subramanian R. V., Crasto A. S.: Electrodeposition of a polymer interphase in carbon-fiber composites. Polymer Composites, **7**, 201–218 (1986).
DOI: 10.1002/pc.750070403

[11] Chang J., Bell J. P., Shkolnik S.: Electro-copolymerization of acrylonitrile and methyl acrylate onto graphite fibers. Journal of Applied Polymer Science, **34**, 2105–2124 (1987).
DOI: 10.1002/app.1987.070340605

[12] Kim J. K., Mai Y-W.: Effects of interfacial coating and temperature on the fracture behaviours of unidirectional Kevlar and carbon fibre reinforced epoxy resin composites. Journal of Materials Science, **26**, 4702–4720 (1991).
DOI: 10.1007/BF00612409

[13] Guo H., Huang Y., Liu L., Shi X.: Effect of epoxy coatings on carbon fibers during manufacture of carbon fiber reinforced resin matrix composites. Materials and Design, **31**, 1186–1190 (2010).
DOI: 10.1016/j.matdes.2009.09.034

[14] Deng S., Zhou X., Fan C., Lin Q., Zhou X.: Release of interfacial thermal stress and accompanying improvement of interfacial adhesion in carbon fiber reinforced epoxy resin composites: Induced by diblock copolymers. Composites Part A: Applied Science and Manufacturing, **43**, 990–996 (2012).
DOI: 10.1016/j.compositesa.2012.01.004

[15] Brostow W., Corneliussen R. D.: Failure of plastics. Hanser, New York (1986).

[16] Chartoff R. P., Menczel J. D., Dillman S. H.: Dynamic mechanical analysis (DMA). in 'Thermal analysis of polymers, fundamentals and applications' (eds.: Menczel J. D., Bruce P. R.) Wiley, New Jersey, 428–432 (2009).
DOI: 10.1002/9780470423837.ch5

[17] Hartmann B., Lee G. F.: Impact resistance and secondary transitions. Journal of Applied Polymer Science, **23**, 3639–3650 (1979).
DOI: 10.1002/app.1979.070231219

[18] Woo L., Westphal S., Ling M. T. K.: Dynamic mechanical analysis and its relationship to impact transition. Polymer Engineering and Science, **34**, 420–427 (1994).
DOI: 10.1002/pen.760340507

[19] Karger-Kocsis J., Gryshchuk O., Jost N.: Toughness response of vinylester/epoxy-based thermosets of interpenetrating network structure as a function of the epoxy resin formulation: Effects of the cyclohexylene linkage. Journal of Applied Polymer Science, **88**, 2124–2131 (2003).
DOI: 10.1002/app.11946

[20] Pothan L. A., Oommen Z., Thomas S.: Dynamic mechanical analysis of banana fiber reinforced polyester composites. Composites Science and Technology, **63**, 283–293 (2003).
DOI: 10.1016/S0266-3538(02)00254-3

[21] Lauprêtre F., Eustache R-P., Monnerie L.: High-resolution solid-state ^{13}C nuclear magnetic resonance investigation of local motions in model epoxy resins. Polymer, **36**, 267–274 (1995).
DOI: 10.1016/0032-3861(95)91313-V

[22] Garcia F. G., Soares B. G., Pita V. J. R. R., Sánchez R., Rieumont J.: Mechanical properties of epoxy networks based on DGEBA and aliphatic amines. Journal of Applied Polymer Science, **106**, 2047–2055 (2007). DOI: 10.1002/app.24895

[23] Delatycki O., Shaw J. C., Williams J. G.: Viscoelastic properties of epoxy-diamine networks. Journal of Polymer Science Part A2, **7**, 753–762 (1969). DOI: 10.1002/pol.1969.160070501

[24] Kim J. K., Mai Y. W.: High strength, high fracture toughness fibre composites with interface control – A review. Composites Science and Technology, **41**, 333–378 (1991). DOI: 10.1016/0266-3538(91)90072-W

[25] Dong S., Gauvin R.: Application of dynamic mechanical analysis for the study of the interfacial region in carbon fiber/epoxy composite materials. Polymer Composites, **14**, 414–420 (1993). DOI: 10.1002/pc.750140508

[26] Deng S., Ma W., Zhou X., Fan C.: Maintenance of highly interfacial shear strength by diblock copolymer between carbon fiber and epoxy resin in hostile environment. Composite Interfaces, **19**, 499–509 (2012). DOI: 10.1080/15685543.2012.761810

[27] Ratna D.: Toughened FRP composites reinforced with glass and carbon fiber. Composites Part A: Applied Science and Manufacturing, **39**, 462–469 (2008). DOI: 10.1016/j.compositesa.2007.12.005

[28] Ghosh P., Bose N. R., Mitra B. C., Das S.: Dynamic mechanical analysis of FRP composites based on different fiber reinforcements and epoxy resin as the matrix material. Journal of Applied Polymer Science, **64**, 2467–2472 (1997). DOI: 10.1002/(SICI)1097-4628(19970620)64:12<2467::AID-APP21>3.0.CO;2-X

[29] Gupta V. B., Drzal L. T., Lee C. Y-C., Rich M. J.: The effects of stoichiometry and structure on the dynamic torsional properties of a cured epoxy resin system. Journal of Macromolecular Science Part B: Physics, **23**, 435–438 (1984). DOI: 10.1080/00222348408219470

[30] Kirk J. N., Munro M., Beaumont P. W. R.: The fracture energy of hybrid carbon and glass fibre composites. Journal of Materials Science, **13**, 2197–2204 (1978). DOI: 10.1007/BF00541674

[31] Beaumont P. W. R., Anstice P. D.: A failure analysis of the micromechanisms of fracture of carbon fibre and glass fibre composites in monotonic loading. Journal of Materials Science, **15**, 2619–2635 (1980). DOI: 10.1007/BF00550768

eXPRESS Polymer Letters Vol.7, No.11 (2013) 936–949
Available online at www.expresspolymlett.com
DOI: 10.3144/expresspolymlett.2013.91

Organically modified hydrotalcite for compounding and spinning of polyethylene nanocomposites

I. Dabrowska[1], *L. Fambri*[1*], *A. Pegoretti*[1], *G. Ferrara*[2]

[1]Department of Industrial Engineering, University of Trento, via Mesiano 77, 38123 Trento, Italy, National Interuniversity Consortium for Science and Technology of Materials (INSTM), Via G. Giusti 9, 50121 Firenze, Italy
[2]LyondellBasell Industries - Basell Poliolefine Italia S.r.l. 'Giulio Natta' R&D, P.le Donegani 12, 44100 Ferrara, Italy

Received 4 June 2013; accepted in revised form 27 July 2013

Abstract. Organically modified hydrotalcite is a recent class of organoclay based on layered double hydroxides (LDH), which is anionically modified with environmental friendly ligands such as fatty acids. In this paper the influence of hydrotalcite compounded/dispersed by means of two different processes for production of plates and fibers of polyolefin nanocomposites will be compared. A polyethylene matrix, suitable for fiber production, was firstly compounded with various amounts of hydrotalcite in the range of 0.5–5% by weight, and then compression moulded in plates whose thermomechanical properties were evaluated. Similar compositions were processed by using a co-rotating twin screw extruder in order to directly produce melt-spun fibers. The incorporation of clay into both bulk and fiber nanocomposites enhanced the thermal stability and induced heterogeneous nucleation of polyethylene crystals. Hydrotalcite manifested a satisfactory dispersion into the polymer matrix, and hence positively affected the mechanical properties in term of an increase of both Young's modulus and tensile strength. Tenacity of nanocomposite as spun fibers was increased up to 30% with respect to the neat polymer. Moreover, the addition of LDH filler induced an increase of the tensile modulus of drawn fibers from 5.0 GPa (neat HDPE) up to 5.6–5.8 GPa.

Keywords: *nanocomposites, hydrotalcite, polyethylene (HDPE), fiber spinning, mechanical properties*

1. Introduction

In recent years several research efforts have been focused on the preparation of polymer/layered inorganic nanocomposites [1–3] because of the excellent properties in comparison to the neat polymer. The main reason of this interest lies certainly in the properties of the nanoclay, like high stiffness, and high aspect ratio, that may induce enhancement of various polymer properties (thermal stability, mechanical properties, flame resistance and gas barrier) even with small amount of filler [3, 4]. The nanocomposite materials can exhibit properties over those expected from continuum mechanics predictions, not achieved with larger scale reinforcement [5]. Moreover, nanocomposites can be processed more easily than microcomposites.

Most of the research has been focused on the smectite-type fillers, such as montmorillonite or hectorite. On the contrary, much less work [6–11] has been focused on the effects of layered double hydroxides (LDH) in polyolefins. The structure of LDH, also referred as hydrotalcite, is derived from brucite or $Mg(OH)_2$, where some Mg^{2+} cations are replaced by trivalent cations yielding positively charged layer [6–8]. Organic modification is adopted to enlarge the interlayer distance of the pristine clay and to increase the hydrophobic nature, thus decreasing the interaction between platelets in order to

*Corresponding author, e-mail: luca.fambri@unitn.it

facilitate its dispersion in hydrophobic polymers [6]. The commercially available nanoparticles consist of aggregates or stacks of platelets which are broken up by stress applied during melt mixing. With proper processing conditions, organically modified nanofiller can be melt-dispersed into polyolefins and exfoliated, while it is not very good as that observed in polyamides, polyurethanes, and some other polar polymers [5]. However, significant improvement of thermo-mechanical, flame retardant, barrier, rheological properties and frequently better thermoforming properties were observed in nanofilled polyethylene [6–8, 12], polypropylene [10] and polybutene [11].

Some polyolefin nanocomposites have been also processed by melt spinning, that is the most common textile process [13]. However, it should be noted that even in the case of low molecular weight polymers, the presence of nanofiller and sometimes the lower level of chain extension determine the formation of various type of defects, and hence relatively low modulus and strength values of the spun fibers. In the case of polyethylene fibers, both linear low density and high density polymers at very low melt flow, between 0.27 and 0.9 dg/min (190°C, 2.16 kg), were spun with various organo-modified clays or with fumed silica [14–18]. The high molecular weight of polymers allowed an efficient drawing process and the achievement of higher mechanical properties of drawn nanocomposite fiber with respect to those of neat polymer. In particular, the organo-modified clay was considered responsible for the reduction of the fiber defects during drawing and for the higher attainable draw ratios [17]. On the other hand, various authors described the production of isotactic polypropylene fibers containing organo-modified clay with a double-step process consisting in a preliminary melt compounding with or without compatibilizer, followed by fiber spinning [19–22] or melt-spun bonding [23]. The fiber properties were found to be dependent on the polypropylene melt flow, ranging between 12 and 35 dg/min (230°C, 2.1 6kg), the nanoclay composition, and the spinning and drawing conditions. Recently, the preparation of polypropylene-nanoclay composite fibers starting from hydrotalcite has been described by Guo and Hagstrom [24].

The present work details the formulation of hydrotalcite/polyethylene composite and the production of melt spun fiber. In particular, HDPE was compounded via melt mixing with an organically modified hydrotalcite masterbatch. Processing and properties of both compression molded plates and melt spun fibers are reported.

2. Experimental

2.1. Materials

High density polyethylene Eltex® A4009 (density 0.96 g/cm^3; melt flow index 0.85 dg/min at 190°C, 2.16 kg) was supplied by BP Solvay (Brussels, Belgium) in the form of fine powder.

Synthetic hydrotalcite organically modified with fatty acid, Perkalite F100 from Akzo-Nobel (CAS number 39366-43-3 and 67701-03-5; density 1.35–1.40 g/cm^3) was provided from Clariant Masterbatches S.p.A. (Pogliano Milanese, MI, Italy) in the form of HDPE pellets containing 12% by weight of LDH and 12% by weight of maleated polyethylene (HDPE-g-MA) as compatibilizer. Before processing, masterbatch was dried in a vacuum oven for 24 h at 90°C.

2.2. Processing

Samples of both neat and nanofilled polymers were prepared by using two types of manufacturing processes: i) plates were produced by mixing in an internal mixer and compression molding; ii) fibers were obtained in a single step by extrusion/compounding in a twin screw extruder.

In the case of plate production, HDPE powder and the selected amount of clay (0.5, 1, 2 and 5% by weight) were physically mixed at room temperature according to the percentage formulation summarized in Table 1. Each mixture was melt compounded in a co-rotating Thermo-Haake (Karslruhe, Germany) Polylab Rheomix internal mixer (155°C; rotor speed 60 rpm; residence time 10 minutes). Subsequently, square sheets (160 mm wide and 1.5 mm thick) were obtained by compression molding in a Carver (Wabash, IN, USA) Laboratory press (155°C; 10 minutes; consolidation pressure 0.2 MPa). The molten plates were then water cooled at 20°C·min^{-1}.

Neat HDPE and nanofilled HDPE fibers were produced after direct mixing and compounding of selected formulation by using a Thermo Haake (Karslruhe, Germany) PTW16 intermeshing co-rotating twin screw extruder (screw diameter = 16 mm; L/D ratio = 25; rod die diameter 1.65 mm). The screws rotation speed was regulated in the range of

Table 1. Designation and formulation of HDPE nanocomposites (in percentage by weight). Dependence of melt flow (230°C, 2.16 kg), hardness Shore D and Vicat Softening Temperature VST on the composition

Sample designation	HDPE [%]	Compatibilizer HDPE-g-MA [%]	Hydrotalcite [%]	MFI [dg/min]	Shore D [Hs]	VST [°C]
HDPE	100	0	0	0.90±0.03	62.2±0.6	136.6±0.3
Masterbatch	76	12	12	1.59±0.02	62.0±0.5	127.8±1.5
LDH-0.5	99	0.5	0.5	0.91±0.03	62.5±0.5	135.9±0.4
LDH-1	98	1	1	1.03±0.02	64.5±0.6	135.8±0.6
LDH-2	96	2	2	1.12±0.02	64.3±0.6	135.4±0.5
LDH-3	94	3	3	–	–	–
LDH-5	90	5	5	1.26±0.03	63.5±0.4	134.0±0.4

3–5 rpm with residence time of 20 min in order to produce HDPE and nanofilled polyethylene fibers with diameter of about 500 μm. The temperature profile was gradually increased from hopper to rod die (T1 = 130, T2 = 200, T3 = 210, T4 = 220, T5 = 220°C) with an output of 140 g/h. The spun fibers were rapidly cooled in water and wounded around a collecting roll/drum at room temperature.

Fibers were drawn ten times at 100°C by using a modified hot-plate drawing apparatus (SSM-Giudici srl, Galbiate, LC, Italy), defining the draw ratio, DR, as the ratio between the initial D_i and final D_f diameter according to Equation (1):

$$DR = \left(\frac{D_i}{D_f}\right)^2 \quad (1)$$

Nanocomposites were designated as LDH (hydrotalcite abbreviation) followed by the filler percentage by weight. For instance, LDH-2 indicates a nanocomposite sample filled with 2 wt% of hydrotalcite.

2.3. Characterization

Melt Flow Index measurements were performed by a Dynisco LMI 400 plastometer (Heilbronn, Germany) according to ASTM D1238-10. About 3 grams of material were preheated at 190°C for 5 min following procedure A and then extruded with an applied load of 2.16 kg.

Scanning electron micrographs (SEM) were obtained by using a Philips XL30 Environmental Scanning Electron Microscopy (Eindhoven, The Netherlands), at an acceleration voltage between 20 and 25 kV. Samples were fractured in liquid nitrogen.

The XRD analysis over 2θ = 1.8–40° for plates and 2θ = 3–30° for fibers, in steps of 0.02° and 5 s measuring time for each point were carried out using a Rigaku III D-Max diffractometer (Tokyo, Japan) in the Bragg-Brentano configuration with Cu-K_α radiation (λ = 0.154 nm) generated at 30 mA and 40 kV.

Shore D hardness was evaluated according to ASTM D2240-05 at 25 °C on 3mm thick rectangular specimen by using an ATS-Faar S.p.A (Milano, Italy) durometer as average of 5 measurements in different positions under an indentation time of 5 sec.

Vicat softening temperature (VST) was measured by a HDT-VICAT instrument from ATS-Faar S.p.A (Milano, Italy) following ASTM D1525-09. Three specimens of 3 mm thickness were used in each test (heating rate of 50°C/h; applied load of 10 N).

Dynamic mechanical thermal analysis (DMTA) was performed on 12 × 5 × 1.0 mm samples with a DMA Q800 testing unit (TA Instruments, New Castle, DE, USA). The experiments were carried out in tensile mode by applying a sinusoidal strain with a frequency of 1 Hz and amplitude of 64 microns under a preload force of 10 N (constant stress of 2 MPa).

Thermal degradation was studied in the range 50–600°C by a thermobalance Mettler TG 50 (Schwarzenbach, Switzerland) on sample of about 15 mg at a heating rate of 10°C/min with an air flow of 100 mL/min. The results represent the average of three tests.

Density measurements were performed by using a Micromeretrics Accupyc 1330 helium pycnometer (Norcross, GA, USA) at 23.0°C. A testing chamber of 3.5 cm^3 was used, and 30 measurements were replicated for each specimen. Standard deviation on each measurement was ±0.001 g/cm^3.

Differential scanning calorimetry (DSC) analysis was performed on samples of about 15 mg in 160 μL aluminum crucible by using a Mettler DSC30 calorimeter (Schwarzenbach, Switzerland), in the range 0–200°C with a heating and cooling cycle at ±10°C/min flushing nitrogen at 100 mL/min. The

crystallinity percentage of HDPE X_{HDPE} was calculated according to Equation (2):

$$X_{HDPE} = 100 \cdot \frac{\Delta H_i}{\Delta H_{HDPE} \cdot (1 - f)} \quad (2)$$

where ΔH_i is the melting enthalpy, ΔH_{HDPE} is the reference enthalpy of a fully crystalline polyethylene, taken as 293 $J \cdot g^{-1}$ [25], and f is the weight fraction of nanofiller.

Mechanical properties of plates and fibers were performed at room temperature by using an Instron 4502 (Norwood, MA, USA) dynamometer, equipped with load cells of 1 kN and 100 N, respectively. Rectangular specimens (80 mm long, 5 mm wide and 1.5 mm thick) and fiber specimens (diameter 500 and 158 micron; gauge length 30 mm) were tested at a cross-head speed of 50 $mm \cdot min^{-1}$. According to ISO 527 standard, the elastic modulus was determined as a secant value between deformation levels of 0.05 and 0.25%. The results represent the average of at least three specimens.

3. Results and discussion

3.1. Compounding and morphology

As reported in Table 1, the investigated formulations are a combination of polyethylene with the nanofiller LDH and the compatibilizer. It should be noted the higher MFI of the masterbatch, and consequently the MFI values increased with the percentage of hydrotalcite in the polymer matrix, with an almost linear dependence on the HDPE-LDH composition (Table 1).

The effect of compounding and the quality of hydrotalcite dispersion into HDPE matrix was evaluated from ESEM analysis of cryo-fractured surfaces of HDPE-LDH nanocomposites. Figure 1a evidences the presence of various agglomerates with dimensions in the range between 5 and 15 microns in the masterbatch containing 12 wt% of hydrotalcite. These agglomerates need to be properly disaggregated and dispersed in HDPE compounds during processing otherwise these defects and stress concentration points could prevent the drawability in fiber spinning [22]. ESEM analysis evidenced the progressive dispersion of LDH in polyethylene matrix. An almost satisfactory result was obtained in compounding through internal mixer for various compositions, as evidenced from the particle dimension at the fracture surface in comparison with that of the masterbatch (Figure 1a). For instance LDH particles of 0.25–0.40 microns and other aggregates of about 0.8 micron were observed in plates at 5% of LDH (Figure 1b). The dimension of both aggregates and particles was found to reduce with the masterbatch content. Figure 1c shows the fracture surface of LDH-1 plate, for which particles of about 0.20–0.35 micron and aggregates up to 0.6 micron were evidenced.

In the case of fibers filled with LDH, some lower size particles were revealed, indicating that twin-screw processing allowed a submicron level of dispersion especially at low hydrotalcite content, as in the case of LDH-0.5 fiber, for which particles of 0.15–0.24 micron were shown in Figure 1d.

The XRD analysis is a very useful method to describe the extent of intercalation and exfoliation of the nanofiller having layered structure. The XRD analysis for HDPE-LDH plates and fibers are reported in Figure 2a and 2b respectively. The XRD pattern was interpreted with respect to the position of the basal peak (003), which depends on the distance between two adjacent metal hydroxide sheets in the LDH crystal lattice. The higher order peaks indicate the presence of repeating crystal planes and symmetry in a specific crystallographic direction [26]. A more intense and sharp peak indicates a more ordered intercalated structure, while less intense and broader peak testify the existence of a disordered intercalated structure [27]. XRD spectrum of LDH-5 plate evidences the two characteristic Bragg reflections of LDH presence at about 4.9° (003) and 11.2° (006), in agreement to the ICPDS Powder Diffraction File (LDH number 41-1428). According to some authors [26] the third peak at 8.4° is attributed to LDH, while it is not included in the ICPDS standard for Al-Mg LDH; however it might be related to the phase derived from primary clay, like Dypingite, $Mg_5(CO_3)_4(OH)_2 \cdot 5H_2O$. For the compositions LDH-2 and LDH-1 with lower nanofiller content only the main peak at 11.2° is well detectable, whereas the two others appear weak and broad. Moreover, XRD spectrum of LDH-5 suggests the presence of another and very intensive reflection at about 1.9° (001), even if not completely visible in Figure 2a, that could be attributed to the presence of bulk LDH nanoplatelets [28].

XRD spectra of HDPE-LDH fibers containing 1 and 2% of hydrotalcite reported in Figure 2b show the characteristic reflections attributed to LDH particles, the very weak peaks and the shift to lower 2θ

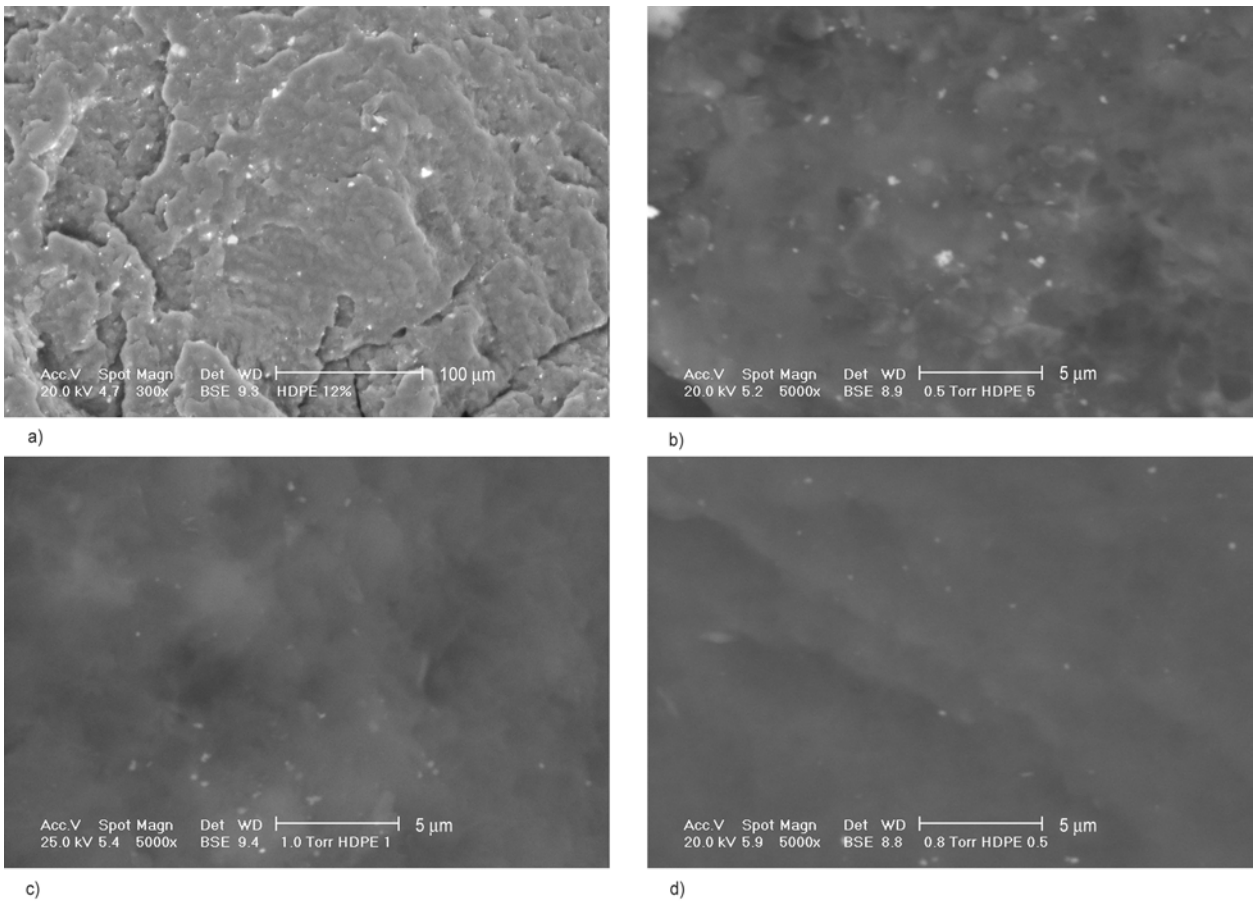

Figure 1. a) ESEM micrograph of masterbatch (fracture surface), b) ESEM micrograph of LDH-5 plate (fracture surface), c) ESEM micrograph of LDH-1 plate (fracture surface), d) ESEM micrograph of LDH-0.5 fiber (fracture surface)

(4.4, 8.1 and 11.0°). It is known that a complete degree of exfoliation of layered crystalline fillers in polymer matrix determines the disappearance of corresponding peaks in the XRD spectra of the composites. However, the absence of the peak could be also related to the very low concentration of the filler [6]. Some of these results might suggest a possible intercalation with partial exfoliation, as reported by other researchers [10, 26–30]. Moreover, after comparison of Figures 2a and 2b, the lower intense reflections of fibers with respect to those of plates, at the same (1 and 2% by wt.) nanofiller content, could suggest that the layer of LDH were better intercalated and partially exfoliated in the polymer during melt compounding/spinning in twin-screw extrusion.

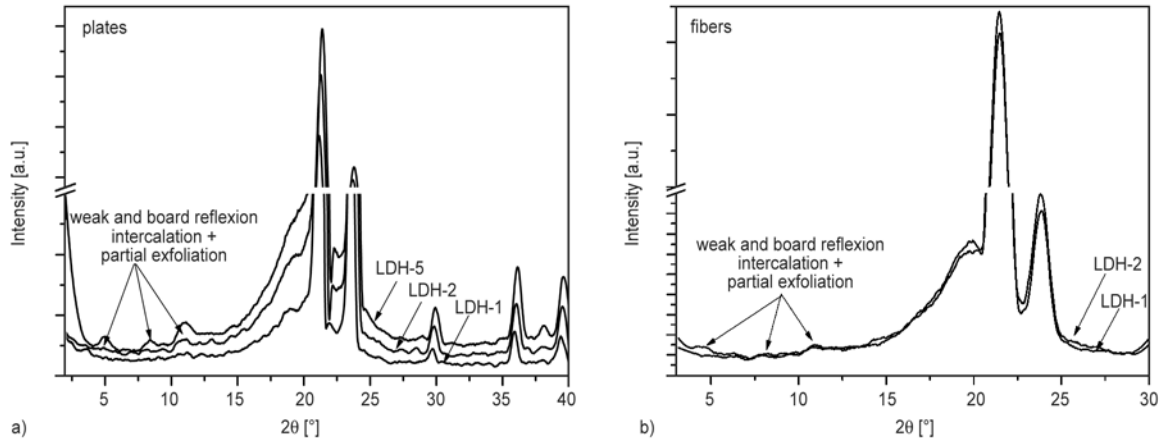

Figure 2. a) XRD patterns of HDPE-LDH nanocomposites plates with different nanofiller content, b) XRD patterns of HDPE-LDH nanocomposites fibers with different nanofiller content

3.2. Compression molded plates (Shore D, Vicat and DMTA)

Shore hardness (Hs) and Vicat softening temperature (VST) are interesting data for the initial comparison of nanocomposite compression molded plates, being related to the tip penetration at room temperature and during heating, respectively. Higher Shore D values of polymer nanocomposites (about 63–64 Hs) with respect to 62.2 Hs for polyethylene evidence the effect of nanofiller, as reported in Table 1. The highest hardness value was obtained for LDH-1 (64.5 Hs), while at higher LDH content the reinforcement action is progressively counterbalanced by the presence of various agglomerates (lower interfacial interaction), reaching for LDH-5 value equal to 63.5 Hs.

Vicat Softening Temperature (VST) gives a useful indication of the relative rigidity at high temperature (Table 1). VST value progressively decreased with the percentage of hydrotalcite in the polymer matrix, in particular from 136.6°C, for neat HDPE, to about 135–136°C for LDH content in the range 0.5–2%, and to 134.0°C for LDH-5 respectively.

The results of dynamic mechanical analysis of neat HDPE and nanofilled HDPE plates are reported in Figure 3. Storage modulus increased with percentage of the organically modified LDH, particularly at lower temperatures, i.e. from –120°C to –20°C, and the highest values were obtained for LDH-5 and LDH-1, as shown in Figure 3. These results could be tentatively attributed to the combined effects of both the filler content and the polymer microstructure (note that hardness values present a maximum for LDH-1). On the other hand at higher temperature above 0°C, both neat HDPE and HDPE-LDH nanocomposites exhibited a similar storage modulus, with some minor differences. In the range 0–50°C the highest storage modulus was found for LDH-1. A similar behavior in the case of LDPE/silica composite was explained from Kontou and Niaounakis by considering the coexistence in the matrix of composite two parts, i.e. the bulk free part and the interphase formed by the physical/chemical interaction of polyethylene molecules and/or crystallization on the filler's surface [31]. Loss modulus evidences in Figure 3 the three main relaxations of polyethylene α, β and γ at about 50, –40 and –120°C respectively, according to literature [32, 33]. The β relaxation, related to the movement of the chain units in the interfacial region [32, 34], typically dependent on branching, is practically absent in the case of neat HDPE, as previously shown for HDPE with melt flow 1.15 dg/min [35]. After addition of 0.5% LDH, the β-peak appears in the zone –50 and 0°C, and it becomes more intense for higher percentage of hydrotalcite [36], as a combined effect of the higher amount of fatty acid, the organo-modifier agent, and the higher interfacial region due to the higher percentage of nanofiller. The position of loss modulus α-peak moved to lower temperature after addition of hydrotalcite masterbatch, i.e. from 59°C of the neat HDPE to 52°C in the case of LDH-5. Moreover, the intensity of the α–peak in loss modulus curves of LDH-composites is higher than that of neat HDPE, in direct dependence on the crystallinity of the polymer matrix.

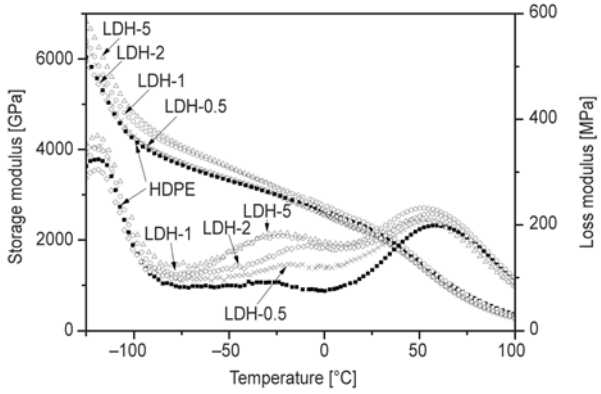

Figure 3. Storage modulus and loss modulus of neat HDPE plates (■) and nanocomposites HDPE plates containing 0.5% (×), 1% (○), 2% (◇) and 5% (Δ) of LDH, respectively

3.3. Thermal properties of plates and fibers

Following the initial characterization of HDPE-LDH plates up to 5% of hydrotalcite, various compositions with a maximum 3% of LDH were also compounded and extruded for fiber production. In particular, this paragraph will describe and compare thermogravimetry results, density and calorimetric data of both plates and fibers with LDH.

Representative TGA curves of plates are reported in Figure 4, evidencing the beneficial effect of organically modified hydrotalcite on the thermal degradation resistance not only for the masterbatch, but also for all the nanocomposites at 0.5–5% LDH, with respect to the neat HDPE. Similar results were observed in the case of fibers, where the curves of nanofilled HDPE appeared shifted at higher temperature.

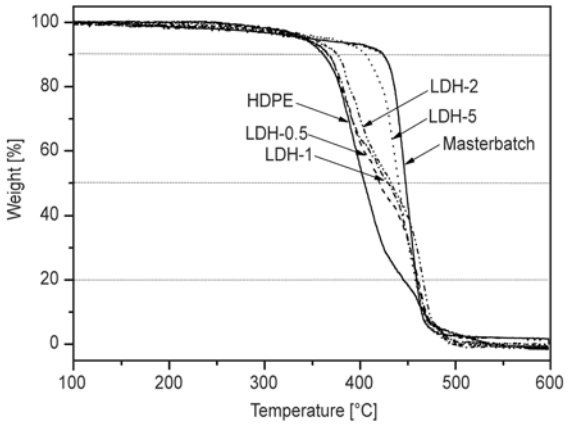

Figure 4. TGA thermograms of neat HDPE and HDPE nanocomposites plates with different LDH content (from 0.5 up to 12% by wt)

The comparison of thermal stability was carried out in terms of selected decomposition temperatures, in particular the initial degradation at 10% ($T_{0.1}$), and the temperatures $T_{0.5}$ and $T_{0.8}$ at which occurred 50 and 80% of mass loss, respectively. The decomposition temperatures ($T_{0.1}$, $T_{0.5}$, $T_{0.8}$) of HDPE-LDH plates and fiber, summarized in Table 2, were found to be higher than those of neat HDPE, even at low hydrotalcite content with a stabilizing effect of nanofiller particles under oxidizing conditions. Following Gilman's suggestion [37], this behavior is due to the hindered thermal motion of the polymer molecular chain. At the same time the selected decomposition temperatures tend to increase with LDH content. However some discrepancies from linearity could be attributed to the parallel contribution of the nanofiller dispersion, particularly at higher mass loss. For instance in the case of fiber and plates containing 1% of LDH, it is worth noting that $T_{0.8}$ was found at a higher temperature than that of masterbatch at 12% of LDH content, 460 vs. 458°C, respectively. The slightly lower degradation temperature of HDPE nanocomposite fibers with respect to plates could be attributed to the higher surface of fiber in oxidizing atmosphere.

Residual mass at 600°C is directly dependent on the nanofiller content, ranging between 0.4% for composition LDH-0.5 up to about 1.8% for LDH-3 fiber and LDH-5 plate. HDPE masterbatch (12 wt% of LDH content) plate exhibited a relevant mass loss of about 3% weight in the range 230–280°C, and a final residue of 4% at 600°C.

Hence, these LDH nanocomposites showed in TGA test a charring process with formation of a charred layer, which enhances the material thermal stability, in conformity to literature results [38, 39]. In fact, the incorporation of clay into a polyolefin matrix enhances its thermal stability by acting as a superior insulator and mass transport barrier to the volatile products generated during decomposition, making the diffusion path of the oxygen more tortuous, and thus retarding the thermo-oxidative process [2, 7, 40].

Bulk properties of plates and fibers were compared in term of density, as shown in Table 3. The results evidenced a direct dependence not only on the composition, but also on the different processing. The higher the LDH content, the higher the density, in between the density 0.957 g/cm^3 of neat polyethylene and the density of the masterbatch, 0.985 g/cm^3. It should be noted that the density of fiber containing 1–3% of LDH is higher not only than HDPE fiber, but it is also higher than the correspondent LDH nanocomposite plates. This evidence reveals that density could be influenced from various other factors than LDH content, for instance from the orientation and from the crystallinity.

For such reason, an investigation of plates and fibers was performed through DSC, as shown in Figure 5 where the heating-cooling cycles of HDPE and selected LDH composites were compared. In

Table 2. Selected TGA results of neat HDPE and nanofilled HDPE plates and fibers

Composition	Temperature of 10% mass loss – $T_{0.1}$ [°C]		Temperature of 50% mass loss – $T_{0.5}$ [°C]		Temperature of 80% mass loss – $T_{0.8}$ [°C]		Residual mass at 600°C [%]	
	plates	fibers	plates	fibers	plates	fibers	plates	fibers
HDPE	356±2	358±2	403±1	412±3	444±6	444±10	0.0±0.2	0.0±0.4
Masterbatch	424	–	447	–	458	–	4.0	–
LDH-0.5	364±5	362±1	420±5	428±5	460±4	454±3	0.4±0.4	0.4±0.1
LDH-1	365±8	368±1	428±2	422±8	460±2	460±6	1.3±0.1	1.0±0.3
LDH-2	371±4	375±5	433±3	425±3	465±6	454±4	1.4±0.3	1.5±0.1
LDH-3	–	389±6	–	433±3	–	452±4	–	1.8±1.0
LDH-5	405±4	–	441±1	–	455±1	–	1.8±0.2	–

Table 3. Density, melting temperature (T_m), crystallinity content, and crystallization temperature (T_c) for pure HDPE and nanofilled HDPE plates and fibers

Composition	Density [g/cm^3]		Melting temperature [°C]		Crystallinity [%]		Crystallization temperature [°C]	
	plates	fibers	plates	fibers	plates	fibers	plates	fibers
HDPE	0.957	0.954	134.6	133.4	70.8	50.5	110.0	110.8
Masterbatch	0.985	–	136.9	–	62.5	–	109.4	–
LDH-0.5	0.958	0.945	136.7	133.0	70.0	51.7	113.5	111.8
LDH-1	0.963	0.960	137.4	133.4	71.8	53.0	114.0	112.5
LDH-2	0.964	0.976	137.5	132.0	71.0	54.5	115.3	112.8
LDH-3	–	0.982	–	133.0	–	53.3	–	115.0
LDH-5	0.971	–	135.0	–	70.4	–	115.3	–

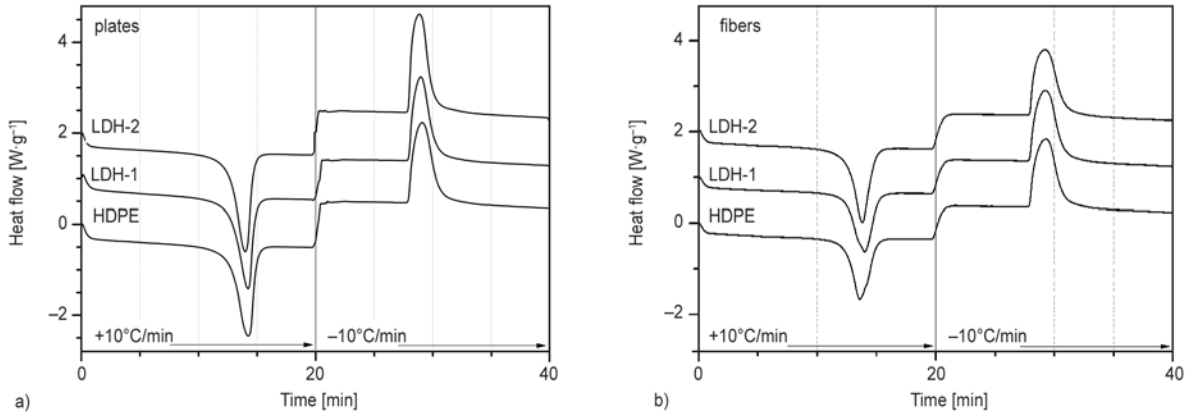

Figure 5. DSC thermograms (heating at +10°C/min and cooling at –10°C/min) of neat HDPE and nanocomposites plates (a) and fibers (b) with different nanofiller content

Table 3, the relative crystallinity values of polyethylene matrix and the temperatures of melting and crystallization during the heating and the cooling were presented. The melting temperature and particularly the level of crystallinity of fiber samples were lower than the correspondent of plate samples, in this latter case about 50 vs 70%, confirming a peculiar dependence on the thermal history in the processing [41]. Fast cooling in fiber spinning (about –20°C/sec) caused not only a quenched crystallization process with the formation of less perfect crystal (and almost constant melting temperature of about 133°C), but also a lower crystallizability. On the other hand, the slow cooling applied for plates (about –20°C/min) determined a slow crystallization rate and hence the formation of more perfect crystals at higher melting temperature, from about 135°C (HDPE) up to 137°C (LDH nanocomposite).

Literature data reported various effects of nanofiller on crystallization temperature and crystallinity content of polyethylene matrix, showing negligible [42], or significant [36, 43] or small differences [12], in dependence on both processing and composition. In our case, the crystallinity of nanofilled polymer was found almost the same in the case of compression molded plates, whereas the final crystallinity of fiber slightly increased with LDH content, in direct conformity to the density measurements.

From the DSC cooling stage, it is noticeable that crystallization temperature of nanocomposites plates and fibers is higher than neat HDPE, i.e. up to 115 versus 110°C, suggesting a mild effect of LDH as nucleating agent. Moreover it should also be considered that the higher crystallization temperature of plates with respect to fibers could be attributed to the higher initial crystallinity of plates, particularly associated to the heterogeneous nucleation attributed to hydrotalcite [10, 37].

3.4. Mechanical properties of plates and fibers

An enhancement of elastic modulus and tensile strength, and a reduction of tensile ductility compared to neat matrix could be expected after a good dispersion of nanofiller [11, 44, 45]. Therefore, mechanical tests were performed on both plates and fibers of various LDH content.

Representative stress-strain curves for plates and fibers are presented in Figures 6, whereas all the

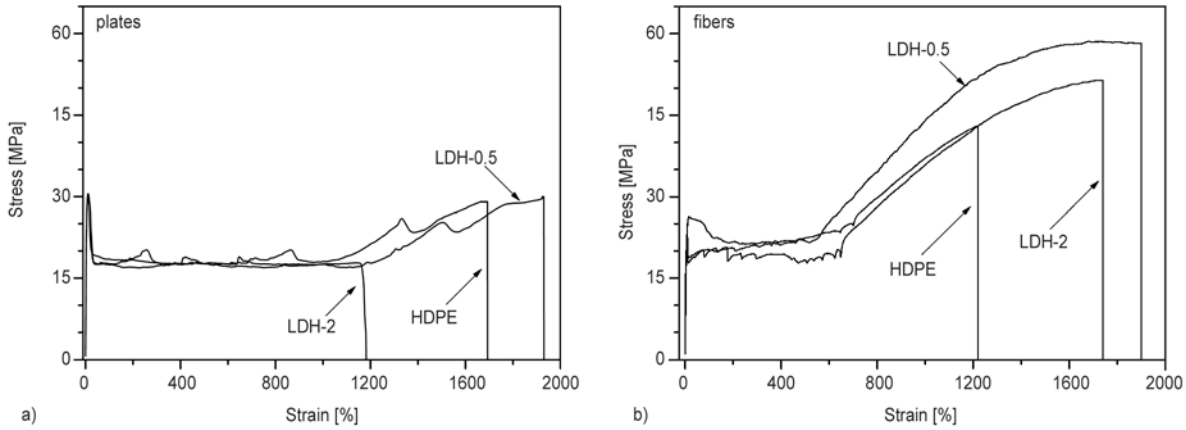

Figure 6. Stress-strain curves of compression molded plates (a) and as-spun fibers (b) of neat HDPE and selected HDPE nanocomposites containing 0.5 and 2% of LDH

Table 4. Tensile mechanical properties of neat HDPE and nanofilled HDPE plates

Composition	Tensile modulus [GPa]	Yield stress [MPa]	Strain at yield [%]	Stress at break [MPa]	Strain at break [%]
HDPE	0.96±0.01	31±1	11±1	26±4	1766±166
LDH-0.5	0.95±0.02	31±1	11±1	29±1	1933±30
LDH-1	1.01±0.03	31±1	11±1	25±1	1590±63
LDH-2	1.03±0.02	31±1	11±1	21±3	1205±144
LDH-5	1.04±0.04	30±1	14±1	17±1	378±60

Table 5. Tensile mechanical properties of neat HDPE and nanofilled HDPE fibers (diameter 500 micron)

Composition	Tensile modulus [GPa]	Yield stress [MPa]	Strain at yield [%]	Stress at break [MPa]	Strain at break [%]	Mechanical draw ratio	Calculated maximum strength [MPa]	Linear density* [tex]	Tenacity* [cN/tex]
HDPE	0.55±0.02	22±2	8±2	42±1	1206±20	13.1	549	187	4.4±0.1
LDH-0.5	0.53±0.01	25±1	16±1	56±4	1860±60	19.6	1098	185	5.9±0.4
LDH-1	0.60±0.08	22±1	11±4	52±6	1360±60	14.6	759	188	5.4±0.6
LDH-2	0.62±0.02	22±1	11±1	53±1	1770±42	18.7	991	192	5.4±0.1
LDH-3	0.66±0.02	23±1	12±1	43±1	1470±70	15.7	675	193	4.4±0.1

*for definition of Linear density and Tenacity see ASTM [48].

results are summarized in Table 4 and in Table 5, respectively. As first evidence, the formulation at 0.5% of organically modified LDH showed the highest ultimate properties of both stress at break and strain at break (about 1900%), either in the case of plates (Figure 6a) or in the case of fibers (Figure 6b). However at the same time, a slightly lower tensile modulus with respect to HDPE was obtained, 0.95 vs 0.96 GPa after compression molding (plates), and 0.53 vs 0.55 GPa after spinning (fibers).

At higher LDH content, a progressive stiffening of both plates and fibers was achieved as expected. The elastic modulus increased up to 1.04 GPa for LDH-5 plates, and up to 0.66 GPa for LDH-3 fibers. It is well known that mechanical properties of a nanocomposite depend upon these two factors, crystallinity of the matrix and reinforcement of the filler [38]. For such considerations, if the elastic modulus of polyethylene and LDH-composite will be compared as a function of the crystallinity a good correlation between the two groups of plates and fibers data can be observed. The main difference of modulus values can be directly attributed to the different processing conditions, because they affected the crystallinity content.

A similar dependence on the crystalline content, was also found in the case of yield stress, resulting about 30 MPa for all the plates (with 70–73% of crystallinity) and about 22 MPa for the fibers (with 50–55% of crystallinity).

Moreover the effect of the nanofiller content on the tensile modulus can be specifically clarified after

the comparison of the relative stiffness of plates and fibers. In particular the relative elastic modulus (REM) was calculated as the ratio between the composite modulus ($E_{HDPE-LDH}$) and the matrix modulus (E_{HDPE}) according to Equation (3):

$$REM = \frac{E_{HDPE-LDH}}{E_{HDPE}} \quad (3)$$

and it was depicted in Figure 7. It is quite evident that the initial reduction for composition at 0.5% of LDH, is followed by a slight increase in the case of plate up to about 7% for LDH-5, and a much higher increment for the fibers (about 20% for LDH-3). This latter effect of stiffening is particularly related to the spinning process, for which the twin screw extrusion at higher temperature determined a better distribution of the filler and the following interaction with the oriented polymer chains.

The comparison of ultimate properties evidenced the higher strength of fibers (Table 5) with respect to plates (Table 4), as result of polymer orientation during the spinning process. Moreover, in the case of fiber a good improvement of stress at break was obtained with hydrotalcite, from 42–46 MPa for neat HDPE, up to 52–56 MPa for nanocomposite at LDH content in the range 0.5–2%. These results could be related to the better filler dispersion and the smaller dimension of hydrotalcite aggregates.

On the other hand, as expected, at higher LDH content, the stiffening effect was also counterbalanced by a consistent and progressive reduction of tensile properties at break, in conformity to other literature data [12, 45, 46]. For instance the strain at break of plates decreased from about 1700% for HDPE plates to 380% for LDH-5. The decrease in both tensile strength and strain at break at high nanofiller content, particularly in LDH-5 plates and LDH-3 fiber, has been attributed to the presence of hydrotalcite aggregates, that may behave as defects, and could also reduce the interfacial adhesion between the matrix and the filler [5, 47].

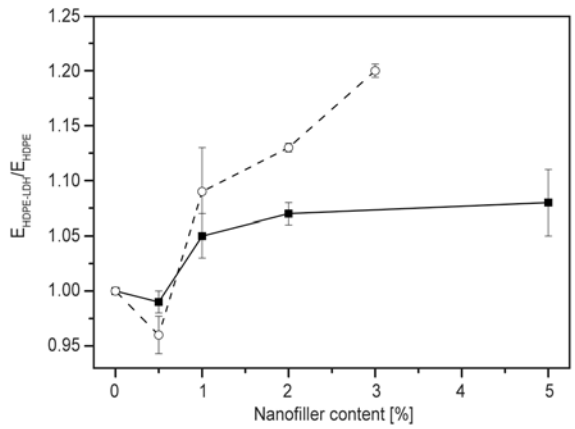

Figure 7. Comparison of relative elastic modulus of plates (■) and fibers (○) as function of nanofiller content

Some other indications on the fiber drawing can be evaluated from the mechanical draw ratio λ_{MEC}, or the maximum drawability that is defined according to Equation (4):

$$\lambda_{MEC} = 1 + \frac{\varepsilon_b}{100} \quad (4)$$

where ε_b is the strain at break expressed in percentage [13, 21].

At the same time, the maximum attainable strength σ_{MAX}, is computable from the stress at break, σ_b multiplied by the mechanical draw ratio, following Equation (5):

$$\sigma_{MAX} = \sigma_b \cdot \lambda_{MEC} = \sigma_b \left(1 + \frac{\varepsilon_b}{100} \right) \quad (5)$$

These data are compared in Table 5. Mechanical draw ratio of nanocomposite fiber ranged in between 15–20, and correspondingly the calculated maximum strength was between 670 and 1100 MPa, with respect to the values of 13 and about 550 MPa of HDPE fiber, respectively. The highest mechanical draw ratio and the maximum strength were obtained for composition at 0.5% of LDH.

The linear density [48] of spun monofilament slightly increased with the LDH content, from 187 tex of neat HDPE fiber up to 193 tex of LDH-3 fiber. At the same time, the tenacity of nanocomposite fibers containing 0.5–2% of LDH was found in the range of 5.4–5.9 cN/tex, much higher than neat HDPE fiber (4.4 cN/tex), indicating the positive effect of LDH dispersion. On the other hand, at higher LDH content, both the stress at break and tenacity decreased as a possible consequence of a non-homogenous nanofiller dispersion.

Selected compositions of as-spun filament were drawn ten times at 100°C, producing fibers of about 158 micron (titer of 19 tex) at higher stiffness and strength. Representative stress-strain curves are shown in Figure 8, whereas tensile results are reported in Table 6. It is well evident that elastic modulus of drawn HDPE-LDH fibers (5.5–5.8 GPa) is higher of about 10–15% in comparison to neat

Table 6. Effect of drawing on tensile mechanical properties of neat HDPE and nanofilled HDPE fibers drawn at 100°C with DR = 10 (diameter 158 micron)

Composition	Tensile modulus [GPa]	Stress at break [MPa]	Strain at break [%]	Mechanical draw ratio	Calculated maximum strength [MPa]	Relative stiffening factor*
HDPE	5.04±0.50	592±50	68±10	1.68	994	9.2
LDH-1	5.54±0.32	460±35	98±5	1.98	910	9.2
LDH-2	5.81±0.42	470±40	98±10	1.98	930	9.4
LDH-3	5.59±0.10	510±20	76±8	1.76	897	8.5

*relative tensile modulus of draw fiber and as-span fiber

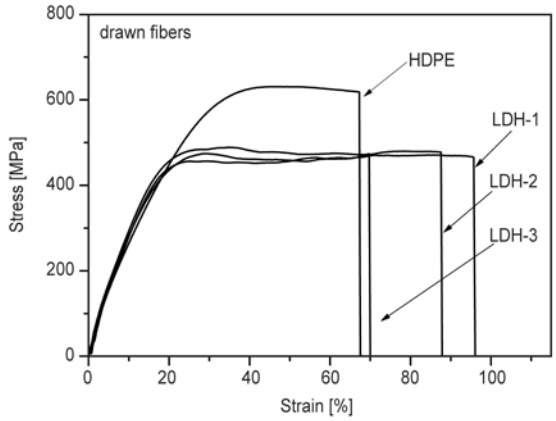

Figure 8. Stress-strain curves of selected fibers of neat HDPE and HDPE nanocomposites drawn ten times at 100°C

HDPE drawn fibers (5.0 GPa), maintaining the stiffening effect of LDH.

The highest improvement was observed for the composition with 2 wt% of nanofiller. Together with improvement in modulus, a slightly lower stress at break was observed, whereas strain at break exhibit higher values in comparison to neat HDPE drawn fiber (Figure 8 and Table 6).

In general, the enhancement of mechanical stiffening observed for nanocomposites can be explained as an effect of the alignment of nanofiller particles along the strain direction [18]. This process is very similar to the exfoliation process induced by the flow in polymer/clay nanocomposites with a good affinity between the two components. The elongation flow could be responsible to the break and orientation of the dispersed nanoparticles aggregates even if the viscosity ratio of the two components is very different and this can be the reason of the observed improvement of tensile modulus [49]. On the other hand after addition of LDH and drawing, nanocomposite polyethylene fibers exhibited a slight lower strength (0.46–0.51 GPa) with respect to neat HDPE drawn fibers (0.59 GPa). At the same time deformation at break of drawn LDH-fiber is higher than that of HDPE (68%). However, the higher the LDH content the lower the deformation at break that decreases from about 100% for LDH-1 and LDH-2 to 75% for LDH-3.

The calculated maximum strength of LDH drawn fibers is about 910 MPa, with respect to 990 MPa of HDPE drawn fibers. Moreover it is worth noting that the relative stiffening factor, calculated as the ratio between tensile modulus of drawn and as-spun fiber, increase from 9.2 for HDPE and LDH-1, to 9.4 for LDH-2 and decreases to 8.5 for LDH-3 (see Table 6).

It can be concluded that a reinforcement effect for HDPE fibers can be obtained with a relatively small amount of hydrotalcite (in the range of 0.5 and 2% by wt.) resulting in a positive combination of improved stiffness (elastic modulus), tenacity (stress at break) and strain at break.

4. Conclusions

HDPE composites with organically modified hydrotalcite were prepared following two different compounding routes, i.e. internal mixing and compression molding, or twin-screw extrusion and spinning. The effect of filler on the thermo-mechanical properties of high density polyethylene was investigated on compression molded plates and as-spun fibers. In both cases, the dispersion of nanoparticles in a content of 0.5–5% significantly improved the thermal stability and the elastic modulus of HDPE. The stiffening effect of nanofiller was also confirmed by the proportional increase of Shore D hardness values.

Depending on the lower cooling rate after compression molding, HDPE plates showed a higher crystallinity with respect to the fibers. However, nanocomposites fibers showed a higher improvement of the relative elastic modulus with respect to the nanocomposites plates containing the same percentage of nanofiller. This behaviour could be a consequence of the different orientation and morphology related to the crystallinity developed in the spin-

ning. These results confirmed that polyethylene containing organically modified hydrotalcite could be easily spinned into nanofilled fibers. The compositions between 0.5 and 2% by wt. of hydrotalcite resulted the more promising for improving the fiber properties. HDPE-LDH drawn fiber exhibited higher stiffness than correspondent HDPE drawn fiber.

Acknowledgements

The authors thanks to LyondellBasell Industries - Basell Poliolefine Italia S.r.l. 'Giulio Natta' R&D and dr. F. Fava (Clariant Masterbatches S.p.A., Pogliano Milanese, MI, Italy) for the formulation and the provision of HDPE hydrotalcite masterbatch. Moreover, prof R. Ceccato (University of Trento) is warmly acknowledged for XRD analysis and for the helpful discussion.

References

[1] Lefebvre J. M.: Nanocomposites, polymer-clay. in 'Encyclopedia of polymer science and technology' (eds.: Kroschwitz J. I., Mark H. F.) Wiley-Interscience, New York, Vol. 3, 336–352 (2003).

[2] Ke Y. C., Stroeve P.: Polymer-layered silicate and silica nanocomposites. Elsevier, Amsterdam (2005).

[3] Ray S. S., Okamoto M.: Polymer/layered silicate nanocomposite: A review from preparation to processing. Progress in Polymer Science, **28**, 1539–1641 (2003). DOI: 10.1016/j.progpolymsci.2003.08.002

[4] Giannellis E. P.: Polymer-layered silicate nanocomposites: Synthesis, properties and applications. Applied Organometallic Chemistry, **12**, 675–680 (1998). DOI: 10.1002/(SICI)1099-0739(199810/11)12:10/11<675::AID-AOC779>3.0.CO;2-V

[5] Paul D. R., Robeson L. M.: Polymer nanotechnology: Nanocomposites. Polymer, **49**, 3187–3204 (2008). DOI: 10.1016/j.polymer.2008.04.017

[6] Costa F. R., Abdel-Goad M., Wagenknecht U., Heinrich G.: Nanocomposites based on polyethylene and Mg-Al layered double hydroxide. I. Synthesis and characterization. Polymer, **46**, 4447–4453 (2005). DOI: 10.1016/j.polymer.2005.02.027

[7] Costa F. R., Wagenknecht U., Heinrich G.: LDPE/Mg-Al layered double hydroxide nanocomposite: Thermal and flammability properties. Polymer Degradation and Stability, **92**, 1813–1823 (2007). DOI: 10.1016/j.polymdegradstab.2007.07.009

[8] Ciardelli F., Coiai S., Passaglia E., Pucci A., Ruggeri G.: Nanocomposites based on polyolefins and functional thermoplastic materials. Polymer International, **57**, 805–836 (2008). DOI: 10.1002/pi.2415

[9] Tonnaer H.: New synthetic organoclays offer improved flame retardancy and gas barrier properties. Plastics, Additives and Compounding, **11**, 14–17 (2009). DOI: 10.1016/S1464-391X(09)70077-7

[10] Marega C., Causin V., Marigo A., Ferrara G., Tonnaer H.: Perkalite as an innovative filler for isotactic polypropylene-based nanocomposites. Journal of Nanoscience and Nanotechnology, **9**, 2704–2714 (2009). DOI: 10.1166/jnn.2009.dk01

[11] Marega C., Causin V., Neppalli R., Saini R., Ferrara G., Marigo A.: The effect of a synthetic double layer hydroxide on the rate of II→I phase transformation of poly(1-butene). Express Polymer Letters, **12**, 1050–1061 (2011). DOI: 10.3144/expresspolymlett.2011.103

[12] Dorigato A., D'Amato M., Pegoretti A.: Thermomechanical properties of high density polyethylene – fumed silica nanocomposites: Effect of filler surface area and treatment. Journal of Polymer Research, **19**, 9889–9899 (2012). DOI: 10.1007/s10965-012-9889-2

[13] George Tomka J.: Textile fiber. in 'Comprehensive polymer science' (eds.: Booth C., Price C.) Pergamon Press, Oxford, Vol. 2, 487–510 (1989).

[14] La Mantia F. P., Tzankova Dintcheva N., Scaffaro R., Marino R.: Morphology and properties of polyethylene/clay nanocomposites drawn fibers. Macromolecular Materials and Engineering, **293**, 83–91 (2008). DOI: 10.1002/mame.200700204

[15] La Mantia F. P., Marino R., Tzankova Dintcheva N.: Morphology modification of polyethylene/clay nanocomposite samples under convergent flow. Macromolecular Materials and Engineering, **294**, 575–581 (2009). DOI: 10.1002/mame.200900066

[16] Chantrasakul S., Amornsakchai T.: High strength polyethylene fibers from high density polyethylene/organoclay composites. Polymer Engineering and Science, **47**, 943–950 (2007). DOI: 10.1002/pen.20778

[17] Rattanawijan W., Amornsakchai T.: Polyethylene composite fibers. I: Composite fibers of high-density polyethylene. Journal of Applied Polymer Science, **124**, 501–509 (2012). DOI: 10.1002/app.34863

[18] D'Amato M., Dorigato A., Fambri L., Pegoretti A.: High performance polyethylene nanocomposite fibers. Express Polymer Letters, **6**, 954–964 (2012). DOI: 10.3144/expresspolymlett.2012.101

[19] Pavliková S., Thomann R., Reichert P., Mülhaupt R., Marcincin A., Borsig E.: Fiber spinning from poly (propylene)–organoclay nanocomposite. Journal of Applied Polymer Science, **89**, 604–611 (2003). DOI: 10.1002/app.11870

[20] Joshi M., Shaw M., Butola B. S.: Studies on composite filaments from nanoclay reinforced polypropylene. Fibers and Polymers, **5**, 59–67 (2004). DOI: 10.1007/BF02875496

[21] Lorenzi D., Sartori G., Ferrara G., Fambri L.: Spinnability of nanofilled polypropylene. Macromolecular Symposia, **301**, 73–81 (2011). DOI: 10.1002/masy.201150310

[22] Rangasamy L., Shim E., Pourdeyhimi B.: Structure and tensile properties of nanoclay–polypropylene fibers produced by melt spinning. Journal of Applied Polymer Science, **121**, 410–419 (2011).
DOI: 10.1002/app.33619

[23] Bhat G., Hedge R. R., Kamath M. G., Deshpande B.: Nanoclay reinforced fibers and nonwovens. Journal of Engineered Fibers and Fabrics, **3**, 22–34 (2008).

[24] Guo Z., Hagström B.: Preparation of polypropylene/nanoclay composite fibers. Polymer Engineering and Science, in press (2013).
DOI: 10.1002/pen.23463

[25] Van Krevelen D. W.: Properties of polymers. Elsevier, Amsterdam (1990).

[26] Costa F. R., Satapathy B. K., Wagenknecht U., Weidisch R., Heinrich G.: Morphology and fracture behaviour of polyethylene/Mg-Al layered double hydroxide (LDH) nanocomposites. European Polymer Journal, **42**, 2140–2152 (2006).
DOI: 10.1016/j.eurpolymj.2006.04.005

[27] Ramírez-Vargas E., Sánchez-Valdes S., Parra-Tabla O., Castañeda-Gutiérrez S., Méndez-Nonell J., Ramos-deValle L. F., López-León A., Lujan-Acosta R.: Structural characterization of LDPE/EVA blends containing nanoclay-flame retardant combinations. Journal of Applied Polymer Science, **123**, 1125–1136 (2012).
DOI: 10.1002/app.34586

[28] Wang Q., Zhang X., Wang C. J., Zhu J., Guo Z., O'Hare D.: Polypropylene/layered double hydroxide nanocomposites. Journal of Materials Chemistry, **22**, 19113–19121 (2012).
DOI: 10.1039/C2JM33493C

[29] Costa F. R., Leuteritz A., Meinl J., Wagenknecht U., Heinrich G.: LDH as nanofiller: Organic modification and dispersion in polymers. Macromolecular Symposia, **301**, 46–54 (2011).
DOI: 10.1002/masy.201150307

[30] Ye L, Wu Q.: Effects of an intercalation agent on the morphology and thermal and flame-retardant properties of low-density polyethylene/layered double hydroxide nanocomposites prepared by melt intercalation. Journal of Applied Polymer Science, **123**, 316–323 (2012).
DOI: 10.1002/app.33770

[31] Kontou E., Niaounakis M.: Thermo-mechanical properties of LLDPE/SiO_2 nanocomposites. Polymer, **47**, 1267–1280 (2006).
DOI: 10.1016/j.polymer.2005.12.039

[32] McCrum N. G., Read B. E., Williams G.: Anelastic and dielectric effects in polymeric solids. Wiley, New York (1967).

[33] Passaglia E., Coiai S., Giordani G., Taburoni E., Fambri L., Pagani V., Penco M.: Modulated crosslinking of polyolefins through radical processes in the melt. Macromolecular Materials and Engineering, **289**, 809–817 (2004).
DOI: 10.1002/mame.200400155

[34] Hippi U., Mattila J., Korhonen M., Seppälä J.: Compatibilization of polyethylene/aluminum hydroxide (PE/ATH) and polyethylene/magnesium hydroxide (PE/MH) composites with functionalized polyethylenes. Polymer, **44**, 1193–1201 (2003).
DOI: 10.1016/S0032-3861(02)00856-X

[35] Kolařík J., Kruliš Z., Šlouf M., Fambri L.: High-density polyethylene/cycloolefin copolymer blends. Part 1: Phase structure, dynamic mechanical, tensile, and impact properties. Polymer Engineering and Science, **45**, 817–826 (2005).
DOI: 10.1002/pen.20337

[36] Tian Y., Zhang H., Qin J., Yu J., Cheng L., Lv Q.: Effect of the ethylene-acrylic acid melt index on the structural characteristics and properties of high-density polyethylene/layered double hydroxide nanocomposites prepared via the master-batch method. Journal of Composite Materials, in press (2013).
DOI: 10.1177/0021998312470153

[37] Gilman J. W.: Flammability and thermal stability studies of polymer layered-silicate (clay) nanocomposites. Applied Clay Science, **15**, 31–49 (1999).
DOI: 10.1016/S0169-1317(99)00019-8

[38] Chen W., Qu B.: LLDPE/ZnAl LDH-exfoliated nanocomposites: Effects of nanolayers on thermal and mechanical properties. Journal of Materials Chemistry, **14**, 1705–1710 (2004).
DOI: 10.1039/B401790K

[39] Ding P., Qu B.: Synthesis of exfoliated PP/LDH nanocomposites via melt-intercalation: Structure, thermal properties, and photo-oxidative behavior in comparison with PP/MMT nanocomposites. Polymer Engineering and Science, 46, 1153–1159 (2006).
DOI: 10.1002/pen.20568

[40] Costantino U., Gallipoli A., Nocchetti M., Camino G., Bellucci F., Frache A.: New nanocomposites constituted of polyethylene and organically modified ZnAl-hydrotalcites. Polymer Degradation and Stability, **90**, 586–590 (2005).
DOI: 10.1016/j.polymdegradstab.2005.05.019

[41] Amornsakchai T., Songtipya P.: On the influence of molecular weight and crystallization condition on the development of defect in highly drawn polyethylene. Polymer, **43**, 4231–4236 (2002).
DOI: 10.1016/S0032-3861(02)00208-2

[42] Deshmane C., Yuan Q., Perkins R. S., Misra R. D. K.: On striking variation in impact toughness of polyethylene-clay and polypropylene-clay nanocomposite systems: The effect of clay-polymer interaction. Materials Science and Engineering A, **458**, 150–157 (2007).
DOI: 10.1016/j.msea.2006.12.069

[43] Xu J-T., Wang Q., Fan Z-Q.: Non-isothermal crystallization kinetics of exfoliated and intercalated polyethylene/montmorillonite nanocomposites prepared by *in situ* polymerization. European Polymer Journal, **41**, 3011–3017 (2005).
DOI: 10.1016/j.eurpolymj.2005.04.042

[44] Ahmed S., Jones F. R.: A review of particulate reinforcement theories for polymer composites. Journal of Materials Science, **25**, 4933–4942 (1990).
DOI: 10.1007/BF00580110

[45] Pegoretti A., Dorigato A., Penati A.: Tensile mechanical response of polyethylene-clay nanocomposites. Express Polymer Letters, **1**, 123–131 (2007).
DOI: 10.3144/expresspolymlett.2007.21

[46] He D., Jiang B.: The elastic modulus of filled polymer composites. Journal of Applied Polymer Science, **49**, 617–621 (1993).
DOI: 10.1002/app.1993.070490408

[47] Mareri P., Bastide S., Binda N., Crespy A.: Mechanical behaviour of polypropylene composites containing fine mineral filler: Effect of filler surface treatment. Composites Science and Technology, **58**, 747–752 (1998).
DOI: 10.1016/S0266-3538(97)00156-5

[48] ASTM D123-13a: Standard terminology relating to textile (2013).
DOI: 10.1520/D0123

[49] Tokihisa M., Yakemoto K., Sakai T., Utracki L. A., Sepehr M., Li J., Simard Y.: Extensional flow mixer for polymer nanocomposites. Polymer Engineering and Science, **46**, 1040–1050 (2006).
DOI: 10.1002/pen.20542

eXPRESS Polymer Letters Vol.7, No.11 (2013) 950–958
Available online at www.expresspolymlett.com
DOI: 10.3144/expresspolymlett.2013.92

Controlled biopolymer roughness induced by plasma and excimer laser treatment

P. Slepička[*], *I. Michaljaničová, V. Švorčík*

Department of Solid State Engineering, Institute of Chemical Technology, 166 28 Prague, Czech Republic

Received 23 May 2013; accepted in revised form 4 August 2013

Abstract. A new method for biopolymer poly-L-lactic-acid (PLLA) surface nanostructuring with surface plasmon resonance appearance is proposed. The motivation of this work is to determine optimal conditions for rough or flat biopolymer surface which may find broad application in tissue engineering as biocompatible carrier for various types of cell lines. A combination of plasma pre-treatment with consequent excimer laser exposure is proposed as a method for increasing the roughness of PLLA surface and changing its morphology. The focus of this paper is to determine morphology changes in combination with mass loss changes. The ablation loss and morphology of PLLA was induced by excimer laser exposure of plasma pre-treated PLLA with different laser fluencies and number of pulses. The combination of a certain input parameters of plasma pre-treatment together with laser exposure induces extensive physico-chemical changes (morphology, contact angle, optical properties) on polymer surface with dramatic roughness increase. Gravimetric studies have revealed an extensive polymer ablation after excimer laser application. The effect of surface plasmon resonance was observed in laser modified PLLA. Conditions for PLLA surface flattening are also proposed.

Keywords: *nanomaterials, biodegradable polymers, plasma pre-treatment, excimer laser, surface characterization*

1. Introduction

Synthetic biodegradable polymers are the most versatile of all materials used in tissue engineering [1, 2]. Their surface properties can be changed e.g. by the application of plasma discharge or laser treatment [3] or by grafting procedures and the limitations of the scaffold architecture could be improved. Poly-L-lactic-acid is such kind of polymer that has been extensively used in tissue engineering [4]. Biodegradable polymers [5, 6] are promising scaffolding materials; however, the roughness of polymer and its surface structure may play a significant role in cell-polymer interaction with a significant improvement of biocompatibility [7]. The surface of a solid material is important to the material performance [8, 9] in at least two aspects, (i) the microstructure and (ii) properties of surfaces, which are usually different from those in the bulk.

Although PLLA polymer represents an important member of biodegradable polymers family, only a few papers have been published about the biomaterial interaction with an excimer laser. The effect of excimer laser exposure on crystallinity and chemical changes of biodegradable polymer has been recently published [3]. The surface modification of biopolymer by ArF laser has been studied [10]. The effect of KrF excimer laser treatment on surface properties of biopolymer foils in combination with plasma treatment remains still to be discovered.

This paper deals with the surface modification of PLLA by plasma pre-treatment in combination with consequent exposure by excimer laser. The effect of

[*]Corresponding author, e-mail: petr.slepicka@vscht.cz

these modifications on its surface morphology is introduced. The ablation (mass loss) of plasma pre-treated samples by excimer laser exposure is determined. The effect of laser pulses number and laser fluence is investigated. The roughness and surface morphology of PLLA was studied by AFM, ablation by gravimetry and surface plasmon resonance by UV-Vis spectroscopy, contact angle measurement by goniometry. The surface induced changes represented by the alteration of both surface morphology and roughness are described in detail. The proposed technique of combination of plasma treatment and excimer modification has been successfully applied for 'super-rough' biopolymer surface.

2. Materials and methods

2.1. Materials, plasma pre-treatment, laser exposure

We used biopolymer poly(lactic acid) (PLLA, density 1.25 g·cm^{-3}, T_g = 60°C, crystallinity 60–70%, 50 μm thick foils, supplied by Goodfellow Cambridge Ltd., Cambridge, Great Britain).

Plasma treatment was accomplished with diode plasma discharge on Balzers SCD 050 (BalTec Maschinenbau AG, Pfäffikon, Switzerland), device for 240 s, using DC Ar plasma (gas purity was 99.997%, 10 W). Process parameters were: Ar flow 0.3 L·s^{-1}, Ar pressure 10 Pa, electrode area 48 cm^2, the inter-electrode distance of 50 mm, chamber volume 1000 cm^3.

For exposure of the PLLA we employed an KrF excimer laser (Coherent Compex Pro 50, Santa Clara, CA USA, wavelength of 248 nm, pulse duration of 20–40 ns, repetition rate 10 Hz). The beam of KrF laser was polarized linearly with cube of UV grade fused silica 25 × 25 × 25 mm with active polarization layer. For homogeneous illumination of the samples we used only the central part of the beam profile by means of an aperture (0.5 × 1 cm^2). The samples were mounted onto a translation stage at perpendicular position of the sample and laser beam. The pulses were chosen from 500 to 6000 with laser fluencies in the interval of 6–30 mJ·cm^{-2}. All experiments with laser treatment of biopolymer PLLA were performed on the samples firstly pre-treated with argon plasma (power 10 W and exposure time 240 s) and consecutively aged for 72 hours, when the surface is 'aged' and stabilized with the exception of samples for comparison.

2.2. Measurement techniques

Surface morphology and roughness of the pristine, plasma and laser treated PLLA samples was examined by AFM technique using a Bruker Corporation CP-II setup (Santa Barbara, CA, USA) device in tapping mode. A Si probe RTESPA-CP with the spring constant of 20–80 N·m^{-1} was used. The mean roughness value (R_a) represents the arithmetic average of the deviations from the centre plane of the sample.

Mean thickness of the removed surface layer after the plasma ablation was measured using a Mettler Toledo UMX2 (Metler Toledo LLC, Columbus, USA) microbalance. The thickness of the removed layer was calculated from the measured change of weight of 3 samples before and after the treatment. The depolarization high-frequency gate was used to discharge the sample surface in order to minimize the influence of surface electrostatic charge on the measurement. After weight-loss determination the ablated thickness was calculated (error ±5%) from the weight of the ablated layer, area of the sample and the PLLA density.

The UV/Vis spectra were measured using a Perkin Elmer Lambda 25 spectrometer in the spectral range from 225 to 400 nm. Applicable range is 190–1100 nm with bandwidth 1 nm (fixed).

Contact angle was determined by goniometry using static water drop method. The measurements of the water contact angles (error ±5%) were performed using distilled water on 4 different positions using the Surface Energy Evaluation System (SEE System, Advex Instruments, Czech Republic). By automatic pipette a water droplet of volume (8.0±0.2) μL was deposited on the polymer's surface and the consequent photo was evaluated. The set of values were then evaluated with the Origin 8.0 program.

3. Results and discussion

3.1. Plasma pre-treatment

The first step of PLLA surface modification was the pre-treatment of the polymer surface by Ar plasma discharge. Previous experiments with only laser exposure of PLLA did not reveal ripple-like patterning of biopolymer PLLA or its significant roughness increase [12, 13]. Therefore the plasma pre-treatment has been implemented. Since the goal of our study was to prepare a highly rough polymer surface, the modification (10 W and 240 s) was chosen for the consequent experiments since the most pronounced

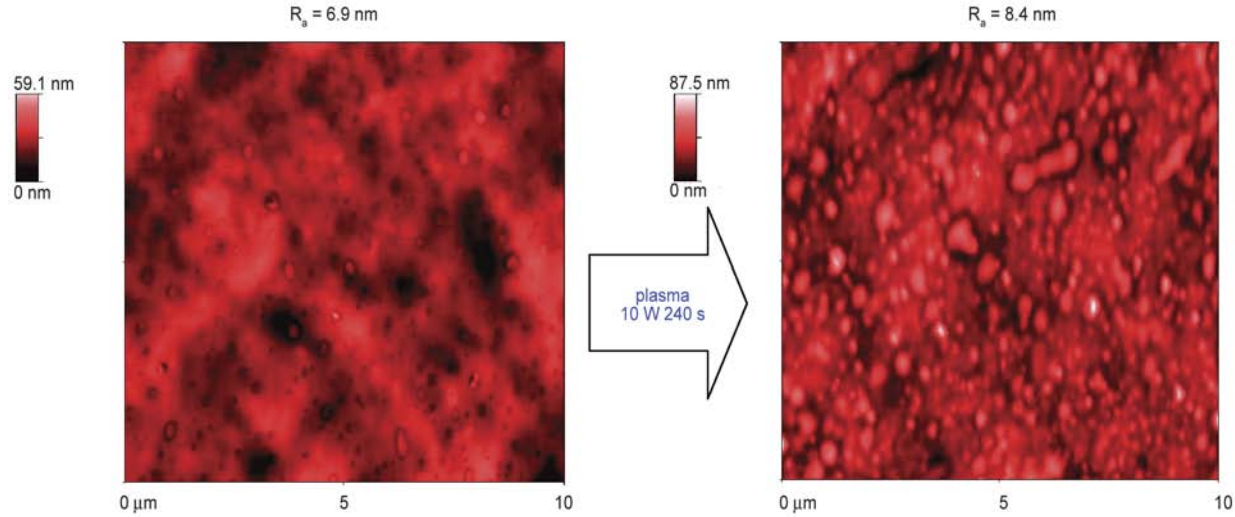

Figure 1. Surface morphology and roughness of pristine PLLA and PLLA pre-treated in argon plasma with 10 W and 240 s

changes in morphology were observed with higher plasma power [14]. As it is obvious from Figure 1, plasma pre-treatment leads to a mild increase of the surface roughness of PLLA. The pristine PLLA sample exhibits lower surface roughness in comparison with the treated samples and 'pits' are apparent on the modified surface. During plasma pre-treatment, the ablation of the polymer surface takes place [14]. The different ablation rate of crystalline and amorphous phases results in the appearance of crystalline structures on the treated PLLA surface. The frequency of crystallites being more pronounced on the treated PLLA with higher plasma power. The amplification of the crystalline phase on the PLLA surface leads to an increase of surface roughness [14]. It is known that beam treatment (e.g. plasma, ions, laser, excimer lamp) of polymer leads to the cleavage of chemical bonds (e.g. C–H, C–C, C–O) [15, 16]. It was shown previously that carbonyl, carboxyl and ester groups are created on the polymer surface layers by the oxidation during or after plasma treatment [17]. The re-orientation of surface polar groups on the polymeric chain leads to lower oxygen concentration in comparison to theoretical value thus influencing the wettability [18].

3.2. Polymer laser ablation

We investigated the influence of laser exposure of plasma pre-treated PLLA (by different number of pulses and laser fluence) on its thickness loss. Since the laser exposure can cause thickness loss of exposed foil, it is important to study the ablation of modified PLLA foil. The thickness loss of PLLA foil induced by plasma pre-treatment under similar

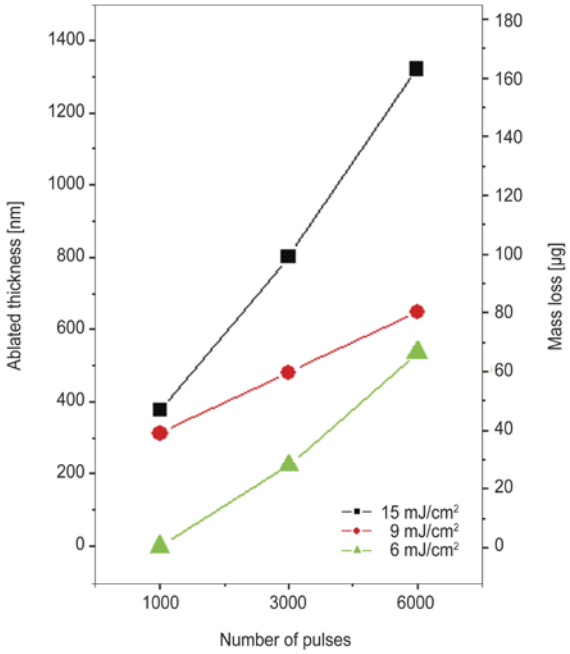

Figure 2. The dependence of PLLA ablated thickness and mass loss on number of laser pulses for laser fluence 6–15 mJ·cm^{-2}. PLLA samples have been pre-treated with plasma (10 W, 240 s)

conditions did not exceeded 100 nm [14]. If the thickness loss caused by consequent laser exposure would be too high, the PLLA surface alteration would not be effective as the mechanical properties of modified foil could be lost. The thickness loss and ablation of plasma pre-treated polymer foils was studied for consequent laser exposure with pulses from 1000 up to 6000 (Figure 2). This number of pulses was applied with laser fluences from 6, 9 and 15 mJ·cm^{-2}. It was found, as expected, that the thickness loss of PLLA foil significantly increases both with increasing laser fluence and number of

laser pulses. With increasing laser fluence the effect of laser pulses becomes stronger. However, the value of thickness loss did not exceeded 1.5 μm (15 mJ and 6000 pulses) which represents about 3% of the bulk. Another important result is that the plasma pre-treatment causes significantly lower ablation in comparison to the excimer laser. Plasma exposure leads to the preferential ablation of the amorphous phase which results in the appearance of the crystalline structures on the treated polymer surface. The heavy argon ions impacting the polymer surface cause polymer bond breakage until the macromolecular chains are released to the ambient atmosphere. The laser exposure (photon impacts) influences also the crystalline phase of the polymer. By the absorption of ultraviolet light also the thermal bond breakage takes place probably, when an inhomogeneous heat flux is present on the biopolymer surface between the pulses [8].

3.3. Surface contact angle (wettability)

The dependence of PLLA contact angle on laser fluence is introduced in Figure 3. The samples were used pre-treated with plasma and aged for more than 72 hours, that means that the input values of PLLA contact angle before laser exposure were those of 90° (surface is stabilized). As it can be concluded from Figure 3, laser exposure leads to the decrease contact angle by aged PLLA and even from pristine PLLA (it is cca 71°). This decrease depends on the number of laser pulses and laser fluence. The

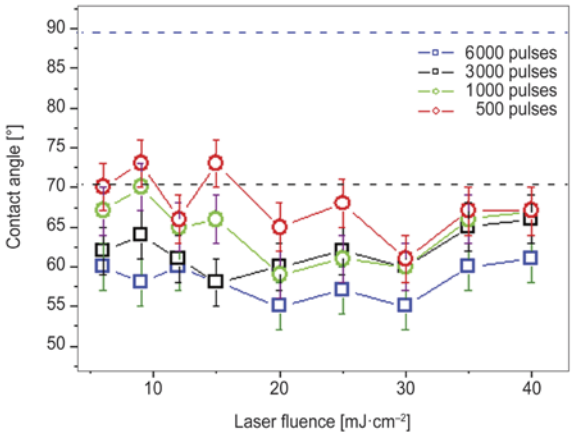

Figure 3. The dependence of contact angle of plasma pre-treated PLLA surface on laser fluencies with different laser number of pulses (500–6000). Black dash line represents contact angle for pristine PLLA, blue dash line (upper one) represents contact angle of aged plasma pre-treated (10 W, 240 s) PLLA.

sample treated with 500 pulses exhibits the highest values of contact angle in comparison to samples exposed with higher number of pulses. With increasing laser fluence the surface morphology is strongly influenced. With more pronounced ablation also the surface chemistry is significantly altered. The macromolecular chains rearrangement ability and chemical structure of modified surface is influenced by the laser fluence. The changes of contact angle are probably caused by several factors involving surface roughness change, e.g. the stability of treated surface (ability to macromolecular chains rearrangement) and amount of ablated biopolymer material. The slight fluctuations of contact angle appear, probably due to the ablation of polymer surface, which were confirmed earlier (Figure 2). The most pronounced decrease of contact angle was observed for samples treated for 6000 pulses. However, the slight increase with higher laser fluence (40 mJ·cm^{-2}) was observed, probably due to more pronounced ablation. The trend of contact angle decrease with higher laser fluence on pristine PLLA was also observed [10], however the PLLA and type of excimer laser was different from our experimental set-up.

3.4. Preparation of highly rough surface

The surface morphology for selected laser exposed samples (fluence 9 mJ·cm^{-2}) is introduced in Figure 4. This laser fluence was chosen since the modification in the interval of 9–15 mJ·cm^{-2} led to the roughness increase similar to that of 9 mJ·cm^{-2}. As a consequence of plasma pre-treatment globular formations (Figure 1) appear. These surface fragments are connected with the ablation of amorphous phase that is typically higher than that of crystalline phase [11]. The applied laser exposure causes at lower laser pulses only a minor change in the surface roughness and morphology. Rather different situation was achieved for laser exposure with 6000 pulses. The plasma pre-treatment combined with consecutive laser exposure (9 mJ, 6000 pulses) causes a sharp increase of surface roughness up to roughness R_a = 25.7 nm. The structure formation is connected to local surface melting caused by interaction of exposed polymer with laser. The microcrystalline regions of polymer bulk (crystallinity 60–70%, according to Goodfellow Ltd.) may react with the incoming polarized laser beam which leads to surface melting, which causes consequent recrystallization. This phenomena together with strong

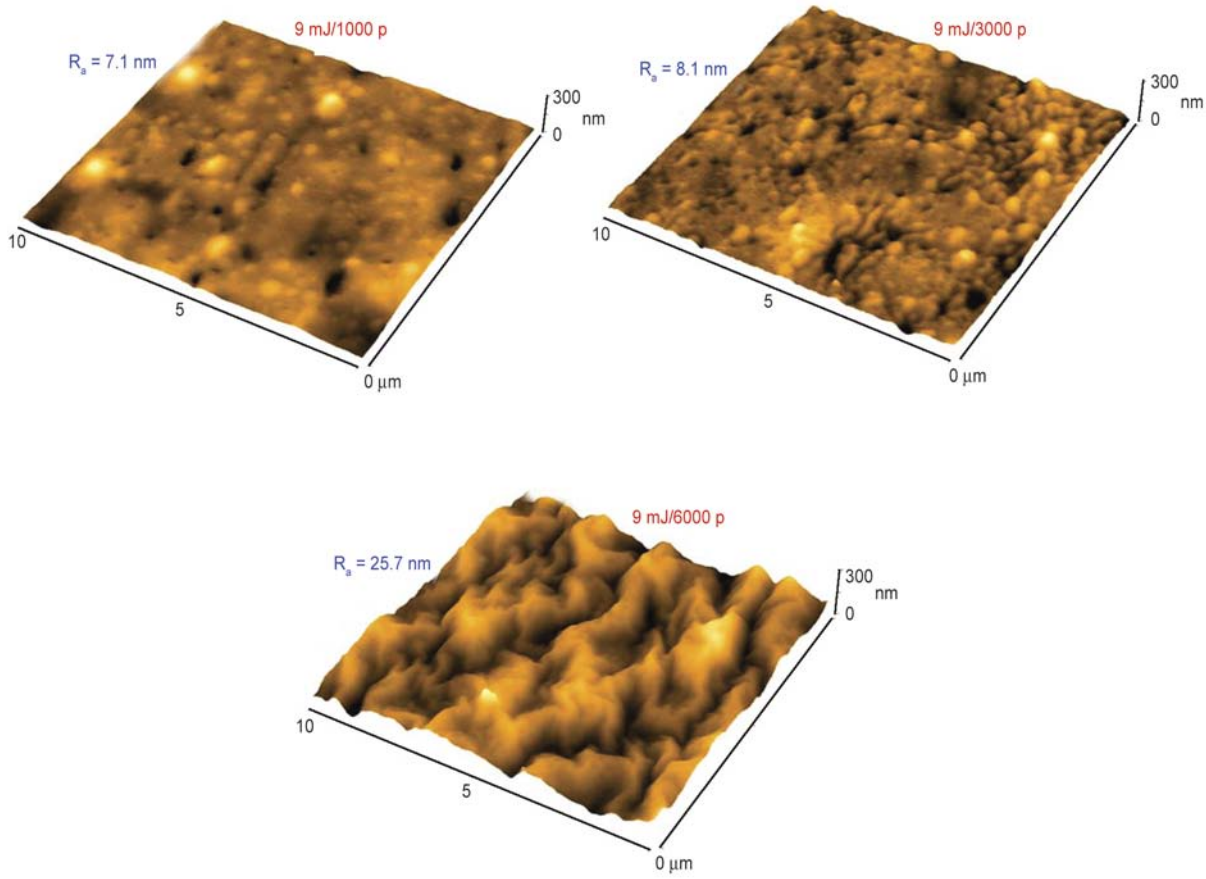

Figure 4. The surface morphology of plasma pre-treated PLLA and consequently exposed with laser beam with 9 mJ cm^{-2} and different number of pulses (1000, 3000 and 6000 p). R_a represents arithmetic mean roughness in nm.

ablation process, when up to 1.5 µm of PLLA could be removed induces a highly rough surface, applicable consequently e.g. as a scaffold for cell adhesion and proliferation improvement.

3.5. Preparation of flat surface

The effect of increase of surface roughness with increasing number of laser pulses can be observed up to a laser fluence of 20 mJ·cm^{-2}. The reason for the increase of plasma pre-treated PLLA surface roughness (e.g. for 9 mJ·cm^{-2}) is the ablation (polymer removal) connected with local heating and melting of laser exposed surface. The ratio of amorphous and crystalline phase (set by the plasma pretreatment, crystalline structures are revealed) is also strongly affected by the increase of laser fluence and polymer removal. The highest laser fluence (30 mJ·cm^{-2}), on the contrary, causes probably such pronounced polymer ablation, that local melting prevails combined with consequent recrystallization. Therefore the opposite effect takes place and the roughness is reduced, as it is obvious in Figure 5. The spherulitic structures exposed by plasma pre-treatment diminishes with increasing number of laser pulses (fluence 30 mJ·cm^{-2}) and the surface roughness being strongly lowered. The dramatic surface roughness changes are visible in Figure 6. As it is evident from Figures 5 and 6, application of plasma pretreatment strongly influences the latter effect of laser exposure. If a lower laser fluence (9 mJ·cm^{-2}) is applied, it leads to a strong amplification of surface roughness of PLLA. Higher laser fluence (30 mJ·cm^{-2}) in combination with plasma pre-treatment has an opposite effect. This observation can find an excellent applications e.g. in tissue engineering [19], where the knowledge of both surface contact angle (wettability) and surface morphology and roughness is important for applicable scaffold construction.

3.6. Optical properties

The UV-VIS absorption spectra of laser exposed PLLA with 9 and 30 mJ·cm^{-2} by different number of laser pulses is introduced in Figure 7a. The same set of samples with plasma pre-treatment is introduced in Figure 7b. It is evident, that both laser flu-

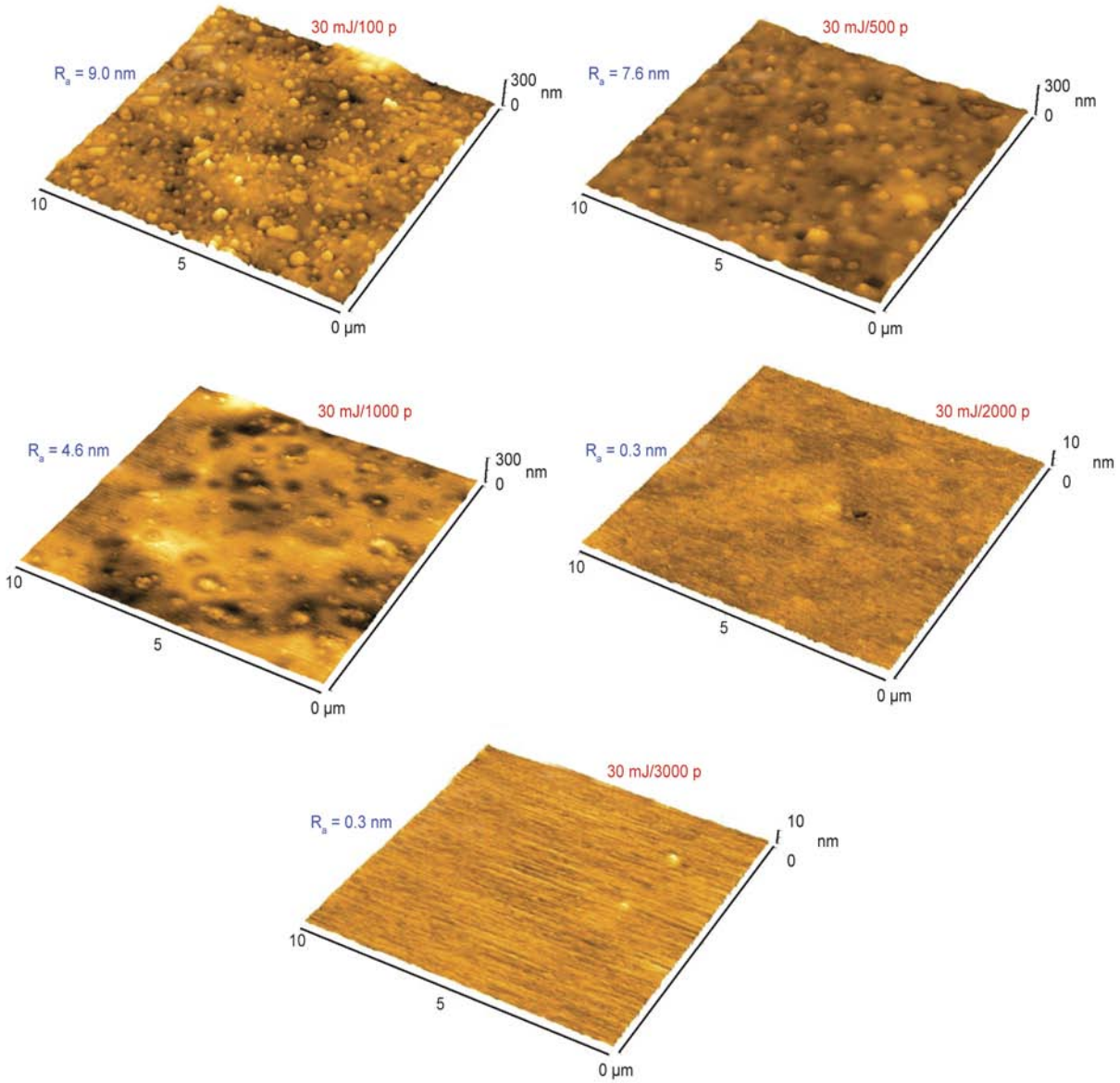

Figure 5. The surface morphology of plasma pre-treated PLLA and consequently exposed with laser beam with 30 mJ cm^{-2} and different number of pulses (100, 500, 1000, 3000 and 6000 p). R_a represents arithmetic mean roughness in nm.

ence and plasma pre-treatment with consequent laser exposure lead under certain conditions to surface resonance peak occurrence. The optical properties of interacting conjugated systems have often been discussed in the framework of molecular exciton theories based on (transition) dipole-dipole interaction models [20]. As it is obvious from Figure 7a, consequent laser exposure significantly influences UV absorption. The slight effect of surface plasmon resonance is observed for higher laser fluence (both 1000 and 6000 pulses). The diagonal shift of the absorbance curve corresponds to increasing both the double bonds concentration [21].

Surface plasmon resonance (SPR) can be described as a collective oscillation of electrons in a solid or liquid stimulated by incident light. The condition for the resonance appearance is established when the frequency of light photons matches the frequency of surface electrons oscillating against the restoring force of positive nuclei. This effect when occurs in nanometer-sized structures is called localized surface plasmon resonance (LSPR). SPR reflectivity measurements can be used to detect molecular adsorption, such as polymers, DNA or proteins, molecular interaction studies [22]. The shift of the curves in extinction spectra can be explained by the coupling of the electromagnetic field between surface plasmons excited in gold nanoparticles of different density and size.

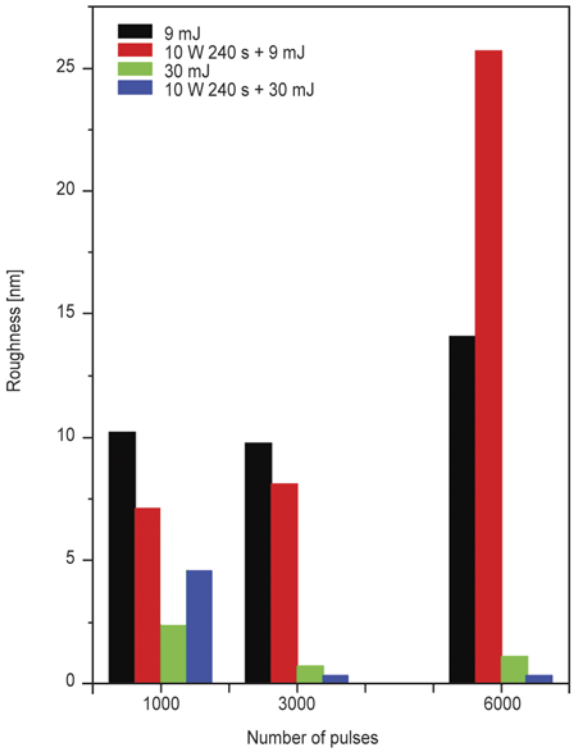

Figure 6. Surface roughness of samples of laser exposed PLLA or plasma pre-treated PLLA (10 W, 240 s) and consequently exposed with laser (9 and 30 mJ cm^{-2}) with different number of pulses (1000, 3000 and 6000)

Rather different situation was observed for samples exposed with lower laser fluence, but number of pulses 6000. The strong peak of surface plasmon resonance was observed at a position of approx. 295 nm, which indicated nanostructures formation on the PLLA laser exposed foil. The phenomenon of plasmon resonance probably arises from structural changes due to annealing while a PLLA surface is exposed to laser fluence. Both the shape and dimension of nanostructure can significantly influence the shape and position of surface plasmon peak [23]. The shift of the peak is connected with the nanoparticle dimension changes or the agglomeration effects. The shifts of the optical-absorption peak were also observed during the reduction of gold-sulfide particles to gold particles [24]. It was previously found, that by controlling the initial size of the gold-sulfide particles, the resonance shift can be correlated with a theoretical model that includes both quantum confinement and the resonance effects (the so-called surface-plasmon resonance) [24]. Ultra smooth surfaces from template-stripping procedures can be also used for periodic structures preparation [25], which can induce effects of surface-plasmon resonance.

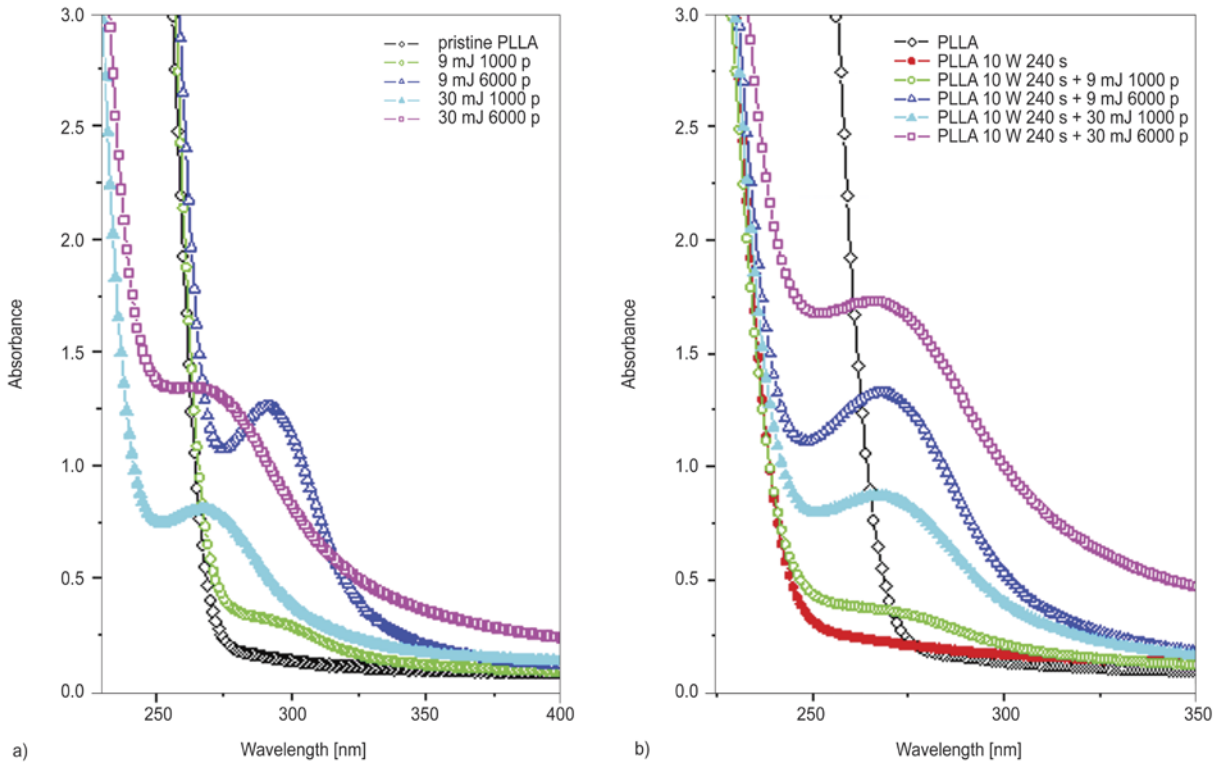

Figure 7. UV-Vis spectra of samples exposed with laser fluence 9 and 30 mJ cm^{-2} (1000 and 6000 pulses) (a); the same samples with plasma pre-treatment (10 W 240 s) (b). The spectra for pristine PLLA (a) and plasma pre-treated PLLA (10 W, 240 s) (b) is introduced for comparison.

The behavior of laser exposed foils with plasma pre-treatment is rather different. The peak of plasmon resonance can be found for the laser exposed samples at the constant position of approx. 270 nm. With increasing the laser fluence and number of laser pulses only the amplification of the peak is apparent, which indicates increasing amount of nanostructures on the modified foils. The absolute value of the absorbance is higher with increasing laser fluence and number of pulses, which is probably caused by the changes in structure morphology, density and size of nanoparticles in the modified surface.

4. Conclusions

A method for preparation of biopolymer surface of high/smaller roughness has been introduced. Plasma pre-treatment of PLLA surface leads to the formation of pits consisting of crystalline phase with mild increase of surface roughness. The combination of plasma pre-treatment with consequent laser exposure leads to an extreme increase of PLLA surface roughness up to 26 nm with appearance of lamellar structures. The exposure of plasma pre-treated surface by laser induces the ablation of PLLA surface. The ablation loss depends strongly on number of laser pulses and applied laser fluence. Under certain conditions a strong decrease of PLLA surface roughness was observed. Optical properties of plasma-pretreated PLLA with laser exposure exhibited plasmon surface resonance effects are dependent on laser fluence, which indicated nanostructures formation in the biopolymer surface.

Acknowledgements

This work was supported by the GACR under project 13-06609S and by financial support from specific university research (MSMT No 20/2013).

References

[1] Tian H., Tang Z., Zhuang X., Chen X., Jing X.: Biodegradable synthetic polymers: Preparation, functionalization and biomedical application. Progress in Polymer Science, **37**, 237–280 (2011). DOI: 10.1016/j.progpolymsci.2011.06.004

[2] Nair L. S., Laurencin C. T.: Biodegradable polymers as biomaterials. Progress in Polymer Science, **32**, 762–798 (2007). DOI: 10.1016/j.progpolymsci.2007.05.017

[3] Hsu S-T., Tan H., Yao L.: Effect of excimer laser irradiation on crystallinity and chemical bonding of biodegradable polymer. Polymer Degradation and Stability, **97**, 88–97 (2012). DOI: 10.1016/j.polymdegradstab.2011.10.006

[4] Gunatillake P., Mayadunne R., Adhikari R.: Recent developments in biodegradable synthetic polymers. Biotechnology Annual Review, **12**, 301–347 (2006). DOI: 10.1016/S1387-2656(06)12009-8

[5] Synytsya A., Grafová M., Slepička P., Gedeon O., Synytsya A.: Modification of chitosan–methylcellulose composite films with *meso*-tetrakis(4-sulfonatophenyl)porphyrin. Biomacromolecules, **13**, 489–498 (2012). DOI: 10.1021/bm2015366

[6] Synytsya A., Synytsya A., Blafková P., Ederová J., Spěváček J., Slepička P., Král V., Volka K.: pH-controlled self-assembling of *meso*-tetrakis(4-sulfonatophenyl)porphyrin-chitosan complexes. Biomacromolecules, **10**, 1067–1076 (2009). DOI: 10.1021/bm8011715

[7] Donoso M. G., Méndez-Vilas A., Bruque J. M., González-Martin M. L.: On the relationship between common amplitude surface roughness parameters and surface area: Implications for the study of cell–material interactions. International Biodeterioration and Biodegradation, **59**, 245–251 (2007). DOI: 10.1016/j.ibiod.2006.09.011

[8] Slepička P., Chaloupka A., Sajdl P., Heitz J., Hnatowicz V., Švorčík V.: Angle dependent laser nanopatterning of poly(ethylene terephthalate) surfaces. Applied Surface Science, **257**, 6021–6025 (2011). DOI: 10.1016/j.apsusc.2011.01.107

[9] Slepičková Kasálková N., Slepička P., Kolská Z., Sajdl P., Bačáková L., Rimpelová S., Švorčík V.: Cell adhesion and proliferation on polyethylene grafted with Au nanoparticles. Nuclear Instruments and Methods in Physics Research Section B: Beam Interactions with Materials and Atoms, **272**, 391–395 (2012). DOI: 10.1016/j.nimb.2011.01.108

[10] Rytlewski P., Mróz W., Żenkiewicz M., Czwartos J., Budner B.: Laser induced surface modification of polylactide. Journal of Materials Processing Technology, **212**, 1700–1704 (2012). DOI: 10.1016/j.jmatprotec.2012.03.019

[11] Siegel J., Řezníčková A., Chaloupka A., Slepička P., Švorčík V.: Ablation and water etching of plasma-treated polymers. Radiation Effects and Defects in Solids, **163**, 779–788 (2008). DOI: 10.1080/10420150801969654

[12] Slepička P., Michaljaničová I., Sajdl P., Fitl P., Švorčík V.: Surface ablation of PLLA induced by KrF excimer laser. Applied Surface Science, in press (2013). DOI: 10.1016/j.apsusc.2013.06.127

[13] Hsu S-T., Tan H., Yao Y. L.: Effect of excimer laser irradiation on crystallinity and chemical bonding of biodegradable polymer. Polymer Degradation and Stability, **97**, 88–97 (2012).
DOI: 10.1016/j.polymdegradstab.2011.10.006

[14] Slepička P., Michaljaničová I., Slepičková Kasálková N., Kolská Z., Rimpelová S., Ruml T., Švorčík V.: Poly-L-lactic acid modified by etching and grafting with gold nanoparticles. Journal of Materials Science **48**, 5871–5879 (2013).
DOI: 10.1007/s10853-013-7383-9

[15] Ročková-Hlaváčková K., Švorčík V., Bačáková L., Dvořánková B., Heitz J., Hnatowicz V.: Bio-compatibility of ion beam-modified and RGD-grafted polyethylene. Nuclear Instruments and Methods in Physics Research Section B: Beam Interactions with Materials and Atoms, **225**, 275–282 (2004).
DOI: 10.1016/j.nimb.2004.05.004

[16] Řezníčková A., Chaloupka A., Heitz J., Kolská Z., Švorčík V.: Surface properties of polymers treated with F_2 laser. Surface and Interface Analysis, **44**, 296–300 (2012).
DOI: 10.1002/sia.3801

[17] Chu P. K., Chen J. Y., Wang L. P., Huang N.: Plasma-surface modification of biomaterials. Materials Science and Engineering: R: Reports, **36**, 143–206 (2002).
DOI: 10.1016/S0927-796X(02)00004-9

[18] Kotál V., Švorčík V., Slepička P., Sajdl P., Bláhová O., Šutta P., Hnatowicz V.: Gold coating of Poly(ethylene terephthalate) modified by argon plasma. Plasma Processes and Polymers **4**, 69–76 (2007).
DOI: 10.1002/ppap.200600069

[19] Goddard J. M., Hotchkiss J. H.: Polymer surface modification for the attachment of bioactive compounds. Progress in Polymer Science, **32**, 698–725 (2007).
DOI: 10.1016/j.progpolymsci.2007.04.002

[20] Cornil J., Beljonne D., Calbert J-P., Bredas J-L.: Interchain interactions in organic π-conjugated materials: Impact on electronic structure, optical response, and charge transport. Advanced Materials, **13**, 1053–1067 (2001).
DOI: 10.1002/1521-4095(200107)13:14<1053::AID-ADMA1053>3.0.CO;2-7

[21] Švorčík V., Prošková K., Hnatowicz V., Rybka V.: Alanine grafting of ion-beam-modified polyethylene. Journal of Applied Polymer Science, **75**, 1144–1148 (2000).
DOI: 10.1002/(SICI)1097-4628(20000228)75:9<1144::AID-APP7>3.0.CO;2-3

[22] McDonnell J. M.: Surface plasmon resonance: towards an understanding of the mechanisms of biological molecular recognition. Current Opinion in Chemical Biology, **5**, 572–577 (2001).

[23] Amendola V., Bakr O. M., Stellacci F.: A study of the surface plasmon resonance of silver nanoparticles by the discrete dipole approximation method: Effect of shape, size, structure, and assembly. Plasmonics, **5**, 85–97 (2010).
DOI: 10.1007/s11468-009-9120-4

[24] Zhou H. S., Honma I., Komiyama H., Haus J. W.: Controlled synthesis and quantum-size effect in gold-coated nanoparticles. Physical Review B, **50**, 12052–12056 (1994).
DOI: 10.1103/PhysRevB.50.12052

[25] Vogel N., Zieleniecki J., Köper I.: As flat as it gets: ultrasmooth surfaces from template-stripping procedures. Nanoscale, **4**, 3820–3832 (2012).
DOI: 10.1039/C2NR30434A